

AFIT/DS/ENP/96-04

CHARACTERIZATION OF SPATIAL AND TEMPORAL  
ANISOTROPY IN TURBULENT MIXING LAYERS  
USING OPTICAL TECHNIQUES

DISSERTATION  
Patrick J. Gardner  
Captain, USAF

AFIT/DS/ENP/96-04

DTIC QUALITY INSPECTED 3

Approved for public release; distribution unlimited

19960718 123

The views expressed in this dissertation are those of the author and do not reflect the official policy or position of the Department of Defense or the U. S. Government.

AFIT/DS/ENP/96-04

CHARACTERIZATION OF SPATIAL AND TEMPORAL  
ANISOTROPY IN TURBULENT MIXING LAYERS  
USING OPTICAL TECHNIQUES

DISSERTATION

Presented to the Faculty of the Graduate School of Engineering  
of the Air Force Institute of Technology  
Air University  
In Partial Fulfillment of the  
Requirements for the Degree of  
Doctor of Philosophy

Patrick J. Gardner, B.S.E.E., M.S.E.E.  
Captain, USAF

May, 1996

Approved for public release; distribution unlimited

CHARACTERIZATION OF SPATIAL AND TEMPORAL ANISOTROPY  
IN TURBULENT MIXING LAYERS USING OPTICAL TECHNIQUES

Patrick J. Gardner, B.S.E.E., M.S.E.E.

Captain, USAF

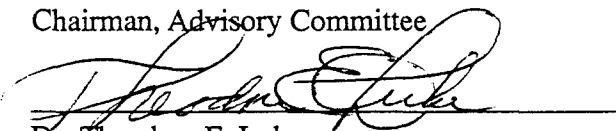
Approved:



Dr. Michael C. Roggemann  
Chairman, Advisory Committee

5/17/96

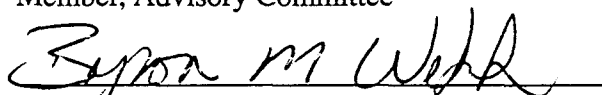
Date



Dr. Theodore E. Luke  
Member, Advisory Committee

5/17/96

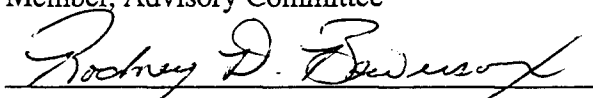
Date



Dr. Byron M. Welsh  
Member, Advisory Committee

5-17-96

Date



Dr. Rodney D. Bowersox  
Member, Advisory Committee

5-17-96

Date

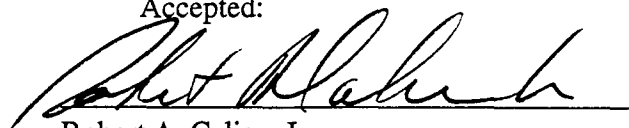


Dr. William E. Wiesel  
Dean's Representative

5-17-96

Date

Accepted:



Robert A. Calico, Jr.  
Dean, Graduate School of Engineering



### *Acknowledgements*

Shortly after becoming a doctoral candidate, I clearly realized the advantage in having an active and committed advisory committee. I thank Dr. Mike Roggemann, my research advisor, for his continuous support, encouragement, wisdom, and great sense of humor. He exemplifies leadership. I am grateful to Dr. Byron Welsh for his persistence in keeping me analytically honest. I also thank Dr. Rod Bowersox, for guiding me through the aeronautical aspects of this research. Finally, I thank Dr. Ted Luke, a long-time mentor and friend, for his valuable insight throughout this program.

Equally important, I enjoyed the advantage in having a loving and supportive family. A very special thanks to my wife, Katerina, who still doesn't understand how a man can compute calculus but can't balance a checkbook. I thank my children: Emily, Erin, Mary, Kevin, and Curtis ('CJ'). They continually bring me joy - even in their teenage years.

Finally, I benefited from the advantage of possessing the determination and discipline required for this rigorous program - qualities that I credit my parents for instilling in me. I am forever grateful to my father and best friend, Philip E. Gardner. He didn't get to see me successfully complete this program - but then, he didn't have to.

Patrick J. Gardner

## *Table of Contents*

	Page
Acknowledgements . . . . .	iii
List of Figures . . . . .	vii
List of Tables . . . . .	x
Abstract . . . . .	xi
 I. INTRODUCTION . . . . .	 1
1.1 Overview . . . . .	1
1.2 Historical Background and Motivation . . . . .	3
1.3 Problem Statement and Scope . . . . .	6
1.4 Summary of Key Results . . . . .	7
1.5 Dissertation Organization . . . . .	8
 II. TURBULENCE MODELS . . . . .	 10
2.1 Aero-Optical Model . . . . .	12
2.2 Atmospheric Model . . . . .	14
2.3 Refractionless Limit Approximation . . . . .	18
2.4 Frozen-Flow Turbulence Model . . . . .	19
 III. FREE TURBULENT MIXING LAYERS . . . . .	 21
3.1 Overview . . . . .	21
3.2 Experimental Setup . . . . .	22
3.3 Statistical Calculations . . . . .	29
3.3.1 Autocorrelation Function . . . . .	31
3.3.2 Structure Function . . . . .	33

	Page
3.4 Structure-Function-Based Modeling of Free Turbulence . . . . .	40
3.5 Strehl Ratio and Reynolds Number Effects . . . . .	43
3.6 Summary of Free Turbulent Mixing Layers . . . . .	46
IV. TURBULENT MIXING LAYERS IN CHANNEL FLOW . . . . .	47
4.1 Overview . . . . .	47
4.2 Experimental Setup . . . . .	48
4.3 Statistical Calculations . . . . .	53
4.3.1 Autocorrelation Function . . . . .	53
4.3.2 Structure Function . . . . .	54
4.4 Structure-Function-Based Modeling of Channel Turbulence . . . . .	62
4.5 Strehl ratio and Reynolds Number Effects . . . . .	64
4.6 Mixing characteristics for other Reynolds numbers . . . . .	70
4.7 Summary of Turbulent Mixing Layers in Channel Flow . . . . .	72
V. TIME-RESOLVED MEASUREMENTS IN CHANNEL FLOW . . . . .	78
5.1 Overview . . . . .	78
5.2 Experimental Setup . . . . .	79
5.3 Simultaneous Shadowgraphs and Wavefront Measurements . . . . .	82
5.3.1 Time-resolved Shadowgraphs . . . . .	82
5.3.2 Temporal Analysis of Shadowgraphs . . . . .	88
5.3.3 Time-resolved Wavefront Slope Measurements . . . . .	94
5.3.4 Temporal Analysis of the Wavefront Phase . . . . .	103
5.4 Simultaneous Wavefront Slope and PSF Measurements . . . . .	104
5.4.1 Phase Structure Function Calculations . . . . .	111
5.4.2 Measurements of Strehl Ratio . . . . .	115
5.5 Summary of Time-resolved Measurements in Channel Flow . . . . .	118

	Page
VI. CONCLUSIONS AND RECOMMENDATIONS . . . . .	121
6.1 Overview . . . . .	121
6.2 Conclusions . . . . .	121
6.3 Recommendations . . . . .	123
Appendix A. Data files for shearing interferometer . . . . .	126
Appendix B. Data files for high-speed cameras . . . . .	129
Bibliography . . . . .	131
Vita . . . . .	135

## *List of Figures*

Figure	Page
1. Hierarchy of Classes of Random Processes . . . . .	11
2. Optical system layout - free turbulence . . . . .	24
3. Shear layer turbulence generator . . . . .	25
4. Flow field schematic . . . . .	26
5. Reconstructed wavefront phase . . . . .	29
6. Surface contour of one phase realization with overlay of 81 anchor points .	30
7. Statistical ACF operation for a single grid point . . . . .	32
8. Surface contour of the autocorrelation function for four anchor points . . .	34
9. Surface contour of the autocorrelation function for four anchor points . . .	35
10. Surface contour of the structure function for four anchor points . . . . .	36
11. Surface contour of the structure function for four anchor points . . . . .	37
12. Average structure function surface contour for 59 anchor points . . . . .	38
13. Average structure function surface contours . . . . .	39
14. Orthogonal slices of $\tilde{D}_\phi(\Delta x, \Delta y)$ . . . . .	41
15. Coefficients $\alpha_x$ and $\alpha_y$ as a function of the six locations in the flow . . . . .	41
16. Coherence parameters, $x_0$ and $y_0$ as a function of downstream location . . .	42
17. Structure function surface approximation using the coherence dimensions, $x_0$ and $y_0$ . . . . .	43
18. Relative Strehl ratio as a function of downstream location . . . . .	45
19. Optical system layout - channel flow . . . . .	49
20. Reconstructed wavefront phase . . . . .	51
21. Point spread function images . . . . .	52
22. Surface contour of one phase realization with overlay of 81 anchor points .	54
23. Surface contour of the autocorrelation function for four anchor points . . .	55
24. Surface contour of the autocorrelation function for four anchor points . . .	56

Figure		Page
25.	Surface contour of the structure function for four anchor points . . . . .	57
26.	Surface contour of the structure function for four anchor points . . . . .	58
27.	Average structure function surface contour for 81 anchor points . . . . .	59
28.	Average structure function surface contours . . . . .	60
29.	Average structure function surface contours . . . . .	61
30.	Orthogonal slices of $\tilde{D}_\phi(\Delta x, \Delta y)$ . . . . .	63
31.	Coefficients $\alpha_x$ and $\alpha_y$ as a function of the six locations in the flow . . . . .	63
32.	Coherence parameters, $x_0$ and $y_0$ as a function of downstream location . . . . .	66
33.	Relative Strehl ratio as a function of downstream location . . . . .	66
34.	Interference images from shearing interferometer . . . . .	68
35.	Interference images from shearing interferometer . . . . .	69
36.	Interference images from shearing interferometer . . . . .	73
37.	Interference images from shearing interferometer . . . . .	74
38.	Interference images from shearing interferometer . . . . .	75
39.	Interference images from shearing interferometer . . . . .	76
40.	Optical system layout - time resolved measurements . . . . .	80
41.	Shadowgraph images . . . . .	84
42.	Shadowgraph images . . . . .	85
43.	Shadowgraph images . . . . .	86
44.	Shadowgraph sequence at 15 cm in the flow . . . . .	89
45.	Shadowgraph sequence at 15 cm in the flow . . . . .	90
46.	Shadowgraph sequence at 15 cm in the flow . . . . .	91
47.	Shadowgraph sequence at 15 cm in the flow . . . . .	92
48.	Operation performed to obtain the correlation coefficient arrays . . . . .	93
49.	Shadowgraph correlation coefficient arrays . . . . .	95
50.	Shadowgraph correlation coefficient arrays . . . . .	96
51.	Shadowgraph correlation coefficient arrays . . . . .	97

Figure		Page
52.	Shadowgraph correlation coefficient Arrays . . . . .	98
53.	Shadowgraph correlation peaks versus frame separation . . . . .	99
54.	Shadowgraph correlation peaks versus frame separation . . . . .	100
55.	Hartmann WFS turbulence sensing system . . . . .	102
56.	Reconstructed wavefront phase from the Hartmann WFS . . . . .	103
57.	Phase correlation coefficient arrays . . . . .	105
58.	Phase correlation coefficient arrays . . . . .	106
59.	Phase correlation coefficient arrays . . . . .	107
60.	Phase correlation coefficient arrays . . . . .	108
61.	Phase correlation peaks versus frame separation . . . . .	109
62.	Phase correlation peaks versus frame separation . . . . .	110
63.	Velocity estimate of the phase correlation peaks . . . . .	112
64.	Surface contour of one phase realization with overlay of 16 anchor points .	112
65.	Surface contour of the structure function for four anchor points . . . . .	113
66.	Surface contour of the structure function for four anchor points . . . . .	114
67.	Surface contour of the structure function for four anchor points . . . . .	116
68.	Relative Strehl ratio calculation as a function of downstream location . . .	119

# *List of Tables*

Table		Page
1.	Summary of Fluid Parameters for the Free Mixing Layers. . . . .	27
2.	Fluid parameters for three He/N <sub>2</sub> mixing ratios (for $C_\delta = 0.26$ ). . . . .	72
3.	Free Turbulence Experiments - Data Files . . . . .	127
4.	Channel Turbulence Experiments - Data Files . . . . .	128
5.	Channel Turbulence Experiments - Slopes and Simultaneous Shadowgraphs	130
6.	Channel Turbulence Experiments - Slopes and Simultaneous PSF's . . . . .	130



### *Abstract*

The optical aberrations induced by mixing layers of dissimilar gases are recorded and analyzed in order to characterize the spatial and temporal properties of the flow. Laser light was propagated through a mixing layer of Helium and Nitrogen gas, having velocities of 8.5 m/sec and 1.5 m/sec, respectively. The light was propagated in a direction perpendicular to the plane of the mixing layer. The mixing layer was evaluated in two experimental regimes: free turbulent mixing, where the mixing layer spreads into the surrounding air; and channel flow, where the mixing layer is confined to a rectangular channel. The optical perturbations induced by the mixing layer were recorded using a lateral shearing interferometer and a point spread function camera. Autocorrelation functions and structure functions were computed from the spatially resolved phase surfaces obtained using the shearing interferometer. For both the free and channel flows, the phase fluctuations were not wide-sense stationary. Consequently, the Strehl ratio predicted by traditional aero-optical models did not agree with experimental measurements except in regions of the flow where the Reynolds number was low. However, the phase fluctuations were locally homogeneous. A two-dimensional power law model was developed, analogous to the one-dimensional Kolmogorov model for isotropic turbulence. This model predicted a relative Strehl ratio which closely matched experiment throughout the flow. In a second series of experiments, the gas velocities were reduced to 4.5 m/s and 1.0 m/s for the Helium and nitrogen gas, respectively. The flow orientation was rotated such that the laser light propagated in a direction parallel to the plane of the mixing layer. Simultaneous high-speed measurements of shadowgraphs and wavefront slopes were used to assess the applicability of Taylor's frozen flow hypothesis to the mixing layer. Comparison of temporal and spatial correlation functions indicated that frozen flow is at best limited to time scales on the order of 1 ms. For this flow orientation the phase fluctuations were found to be nonhomogeneous for all regions analyzed.

# CHARACTERIZATION OF SPATIAL AND TEMPORAL ANISOTROPY IN TURBULENT MIXING LAYERS USING OPTICAL TECHNIQUES

## I. INTRODUCTION

### 1.1 Overview

The characterization of interactions between optical waves and fluid flow is a difficult problem for optical systems which require light propagation through complex flow fields. Light waves which pass through turbulent mixing layers are aberrated by index-of-refraction fluctuations in the flow [48]. These index-of-refraction fluctuations arise from random spatial and temporal fluctuations in the gas density. The phase of an optical wave that propagates through a turbulent region will be aberrated, degrading the performance of imaging and beam projection systems. Imaging through aircraft optical windows, for instance, is degraded by turbulence fluctuations of the mass density in the boundary layer on the window [46], where the index-of-refraction,  $n$ , varies proportionally to the mass density by the relationship:

$$n = 1 + G \frac{\rho}{\rho_s} \quad (1)$$

where  $G$  is the Gladstone-Dale constant,  $\rho$  is the mass density in the field, and  $\rho_s$  is the mass density at standard conditions. These randomly distributed index variations induce phase perturbations in a transmitted optical field which may result in bore-sight and centroid errors for tracking systems, blur and identification problems for imaging systems, and defocus and jitter for directed energy systems [21], any of which can substantially impact mission effectiveness.

Adaptively correcting for the random phase fluctuations requires an understanding of the spatial and temporal characteristics of the turbulence; hence, a great deal of research

has been dedicated to developing various techniques for visualizing the turbulent flow and predicting the optical effects. Examples of such techniques are shadowgraphs, schlieren, laser light sheets, thin-beam raster scan, holography, and wave front sensors, such as shearing interferometers and Hartmann sensors.

The problem of optical propagation through turbulence has been addressed for two general applications: (1) imaging and laser beam projection through turbulence in the extended free atmosphere, for example from a ground-based telescope, and (2) imaging and laser beam projection through boundary layer turbulence generated near aerodynamic surfaces, for example from a turret-mounted telescope on an aircraft (the aero-optical problem). Understanding the optical effects of turbulence requires that the random nature of the turbulence be characterized. However, a characterization appropriate for modeling atmospheric turbulence may be completely inappropriate for modeling aerodynamic turbulence. For example, assuming statistical isotropy to at least second order has been shown to be valid for atmospheric imaging scenarios [26] and is often invoked as a means to reduce four-dimensional problems to one-dimensional problems, allowing for a simpler analytical solution [6, 13]. Current analytical models in use today for aero-optical scenarios attempt to make similar simplifications, often with dubious success [15].

The purpose of this research is to develop a more thorough understanding of the statistical properties of complex flow fields, such as that encountered in boundary layer turbulence. A widely-accepted laboratory simulation of such a flow is obtained by the mixing of dissimilar gases with high density ratios, such as Helium and Nitrogen [2, 3, 5, 55]. For this research, the optical aberrations induced by the He/N<sub>2</sub> mixing layer are evaluated for evidence of stationarity. Both the atmospheric and aero-optical models are tested for applicability. A new statistical model of the optical aberrations induced by the mixing layer is introduced. The model is based on Kolmogorov-like properties observed in the mixing layer. In addition, temporal properties of the mixing layer are investigated for applicability of frozen flow assumptions.

## 1.2 Historical Background and Motivation

In the late nineteenth century, Osborne Reynolds published a series of observations on the transformation of laminar flow of fluids in pipes to turbulent flow. Reynolds found the fluids transition according to a ratio of the inertial and viscous forces acting within the fluid, a relationship which was later named the 'Reynolds Number' of the flow. The inertial forces tend to contribute to the transfer of energy in the flow from large-scale components of motion to smaller-scale components, leading to the emergence of small-scale inhomogeneities, characteristic of turbulent flow. Meanwhile, the viscous forces tend to smooth the small-scale inhomogeneities, eventually leading to the transfer of kinetic energy to heat dissipation in the fluid [30]. Hence, flows with sufficiently low Reynolds numbers are usually laminar, while those with sufficiently high Reynolds number are turbulent.

The concept of inertial forces in a fluid giving rise to a hierarchy of small-scale inhomogeneities, coupled with viscous forces reducing the smallest scales of motion to heat dissipation was summarized by Lewis Richardson [36] in this simple poem, published in 1922:

*Big whorls have little whorls,  
Which feed on their velocity;  
And little whorls have lesser whorls,  
And so on to viscosity  
(In the molecular sense)*

In another significant contribution to the early theory of turbulence, Reynolds suggested the hydrodynamic quantities in the turbulent flow might be divided into regular and irregular components, recognized today as the mean and fluctuating components. Additionally, Reynolds introduced the concept of homogeneity and isotropy in the small-scale fluctuating components of the fluid dynamics.

Following Reynolds early work, a vast amount of research was dedicated to understanding the mechanics of turbulence. Noted scientists such as Ludwig Prandtl and Theodor von Karman, one of Prandtl's students, formulated semi-empirical theories of turbulence.

These formulations were derived through extensive measurements in pipe flow, channel flow, and free turbulent flow, used to predict the outcome of subsequent experiments under similar conditions [30]. The turbulence was theorized to be analogous to molecular chaos; hence, properties such as mixing length, turbulence intensity, viscosity, thermal conductivity, and diffusion were used to describe the transfer of momentum and heat through the large-scale components of motion in the flow.

Today the study of turbulent flow fields may be divided into two distinct perspectives. One approach views the turbulence as being composed of 'building blocks' of quasi-deterministic vortex structures. Moon [31] makes the following assertion:

*In the physical sciences, the paragon of chaotic behavior is turbulence. Thus, a rising column of smoke or the eddies behind a boat or aircraft wing provide graphic examples of chaotic motion. The fluid mechanician believes that these events are not random because the governing equations of physics for each fluid element can be written down. A great deal of excitement in nonlinear dynamics today is centered around the hope that this transition from ordered to disordered flow may be explained or modeled with relatively simple mathematical equations.*

The evidence of large-scale coherent structures at high Reynolds numbers was confirmed in early experiments by Brown and Roshko [2]. Consequently, significant effort has been dedicated to modeling turbulence as a purely deterministic process. One extreme example of this approach, which treats transition from laminar to turbulent flow in terms of chaotic transitions may be found in Lee [24]. Significant contributions have been made by investigators treating mixing layers as a deterministic process. Applying frozen flow assumptions, thin beam transmissions at high pulse rates through the mixing layers have provided valuable insight into the mixing transition effects, and characteristics of streamwise and spanwise coherent structures [21, 55].

A contrasting approach, termed the 'classical theory' [18], views turbulence as a random process, decomposed into a mean and fluctuating constituent which is analyzed statistically. Monin and Yaglom [30], both students of A. N. Kolmogorov, described the nature of turbulence as follows:

*The only possibility in the theory of turbulence is a statistical description, based on the study of specific statistical laws, inherent in phenomena en masse , i.e., in large ensembles of similar objects. Thus only statistical fluid mechanics, which studies the statistical properties of the ensembles of fluid flows under macroscopically identical external conditions, can provide a turbulence theory.*

Many significant contributions have been made using a statistical approach to turbulence. The Kolmogorov model is firmly rooted in the analysis of optical propagation through the turbulent atmosphere and has been verified using both laboratory measurements and direct airborne measurements of the atmosphere [30]. Additionally, an abundance of airborne measurements of propagation loss through boundary layer turbulence has been collected and compared with statistical models [23, 32, 40, 48]. These models have shown various degrees of success, limited primarily to the validity of the isotropy assumptions [15].

For the present research, the turbulent mixing layers are treated as a random process. The clear persistence of orderly structures in the mixing layer cannot be ignored. In fact, this research will capitalize on the presence of the coherent structures, through flow visualization techniques, to estimate the evolution of the mixing layer. However, it's further assumed that a sufficiently large ensemble of independent measurements will permit isolation of the deterministic and random features in the flow, such that a statistical analysis may be performed. No assumptions on stationarity are made, rather stationarity is tested on measurement ensembles. A detailed discussion of the statistical treatment of the experimental data is presented in Chapters III and IV.

Previous work at the Air Force Institute of Technology set the stage for the research presented here. In 1992, Captain Eric Magee conducted statistical calculations on phase aberrations resulting from the propagation of plane waves through heated jets of air. The phase surfaces were obtained using the same lateral shearing interferometer which was used for the current research. Captain Magee concluded that the random phase fluctuations resulted in phase structure functions which were approximately isotropic and could therefore be modeled by Kolmogorov statistics [26]. A more detailed description of Kolmogorov turbulence and phase structure functions is in Chapter II. Captain Magee's research was a testing ground for

the lateral shearing interferometer for AFTT. In addition, his general technique for evaluating isolated phase points on a 'grid' was followed for the current research. In 1994, Captain Dan Jewell designed and fabricated the dual-chamber turbulence generator which was used in the current research and is described in detail in Chapter III. Captain Jewell conducted visualization experiments for a free-flowing mixing layer of Helium and Nitrogen gas. The visualizations consisted of orthogonal views of the mixing layer, represented by shadowgraphs, interference images from the shearing interferometer cameras, and reconstructed phase surfaces from the shearing interferometer system [20]. In concert, these two research projects provided the background knowledge and necessary resources to develop a novel method to better understand the anisotropic properties of turbulent mixing layers.

### *1.3 Problem Statement and Scope*

Turbulence-induced optical phase distortions have been studied and modeled extensively. To reduce the complexity of the four-dimensional problem, homogeneous, isotropic, and even ergodic statistics are assumed. These assumptions have been shown to be valid for atmospheric propagation in most cases; however, the same assumptions fail for propagation through aero-optical turbulence, which involves shear layers, boundary layer separation, shock layers, and the more 'benign' inviscid flow region. In spite of the complexity resident in aero-optical flows, assumptions on homogeneity are typically applied for lack of a better model [15]. A better measurement and analysis technique is needed for these complex flows; i.e., one that can quantify the anisotropy and use this statistical property to generate a more reliable analytical model of the optical aberrations encountered in these complex flows.

This research investigates the effects of light propagation in an aero-optical environment via experimental measurements of turbulent mixing layers in an optical laboratory. A shear layer mix of Helium and Nitrogen gas provides the complex flow field to evaluate. The mixing layer is evaluated in a free flow environment, as well as in a confined channel flow. In total, over 20,000 images were recorded for analysis. For both flow regimes, the random phase fluctuations are assessed for wide-sense stationarity and stationarity in first increments. The

research identifies Kolmogorov properties in an anisotropic flow, resulting in a new method to model the turbulent mixing layer.

#### *1.4 Summary of Key Results*

This research uses a variety of techniques for analyzing the optical effects induced by turbulent mixing layers. A summary of the key results from this research follows:

1. Statistical autocorrelation functions of the phase fluctuations are reported for a free turbulent Helium/Nitrogen mixing layer. These functions were not wide-sense stationary for any region in the flow; thus, application of the isotropic aero-optical model was shown to be invalid.
2. Phase structure functions are reported for the free turbulence and are shown to be locally homogeneous for all regions in the flow. Orthogonal components of the average structure functions are used to generate a two-dimensional power law model for the structure function of the phase aberration, analogous to the Kolmogorov five-thirds power law for isotropic turbulence.
3. Relative Strehl ratio predictions, accounting for the statistical anisotropy, are derived from the free turbulence model. The traditional aero-optical model is shown to be a poor estimate of optical degradation at high Reynolds numbers in comparison to the anisotropic model.
4. Results are reported on a Helium/Nitrogen mixing layer in a channel flow, similar to items 1-3 above. These mixing layers are also shown to be locally homogeneous, but not wide-sense stationary, and a two-dimensional power law model for the structure function of the phase aberration is developed. The model predicts a cross-over region in the flow for orthogonal components of the density fluctuations. The cross-over indicates a region in the flow where the optical degradation in the streamwise direction surpasses that of the cross stream direction, indicative of growth of the mixing layer



width coupled with molecular mixing of the gases. This region is shown to coincide with the maximization of the mixing layer width in the channel.

5. For the channel flow, relative Strehl ratios are computed from measured average point spread functions. The Strehl ratios predicted from the isotropic aero-optical model are shown to match experiment only in regions close to the exit nozzle of the turbulence generator, where the Reynolds number is low. The anisotropic model developed in this research is shown to match closely with experiment for all locations in the flow.
6. Using the anisotropic model developed in this research and interferometric flow visualization images of the flow, a technique is demonstrated for estimating fluid parameters such as mixing layer width, local Reynolds number, and mixing layer experimental coefficients.
7. High-speed slope measurements and frame-registered shadowgraphs are reported for the channel flow with the mixing layer plane oriented parallel to the laser propagation. A technique for computing an array of correlation coefficients over a two-dimensional sliding window for various temporal separations is introduced. From the peaks of the coefficient arrays, the temporal scale for frozen flow is determined. The temporal scales are on the order of 4 ms for the shadowgraphs and 1 ms for the wavefront phase.
8. High-speed slope measurements and frame-registered point spread functions are reported for the channel flow with the same mixing layer orientation. With this orientation (orthogonal to the results in items 1-6 above) the phase structure functions are shown to be nonhomogeneous. Relative Strehl ratios are computed from the average point spread functions, with a minimum value substantiating the anisotropic model previously developed in this research.

### *1.5 Dissertation Organization*

The dissertation is organized into six chapters. Chapter II presents an overview of a generally accepted aero-optical model, highlighting the basic assumption of statistical isotropy inherent in the model. This is followed by a description of the Kolmogorov model for

atmospheric turbulence, also noting typical assumptions. Chapter III presents experimental results performed on a free turbulent mixing layer of Helium and Nitrogen gas at fixed velocities, interfacing with the surrounding ambient air. A lateral shearing interferometer is used to obtain phase measurements with high spatial resolution. This chapter describes the experimental setup, statistical calculations and homogeneity assessment, and some novel modeling parameters which enable predictions of a relative Strehl ratio. The ratio is relative because it relates the mixing-layer-induced aberrations to the experimental imaging system, rather than a non-measurable, diffraction-limited system. This relative Strehl ratio is then related to the Reynolds number in the flow. Chapter IV presents experimental results acquired for the same Helium/Nitrogen mixing layer, this time confined within a rectangular channel. Again, the shearing interferometer is used to obtain the phase measurements. Similar statistical calculations and modeling parameters are presented. In these experiments, the point spread function is also measured as an independent source for the Strehl ratio. While both the free flow and channel flow experiments are modeled similarly, the techniques developed in this research clearly distinguish the anisotropy characteristics in the two flows, a capability not previously demonstrated with non-invasive measurements. In Chapter V, the channel flow is revisited, this time using high-speed cameras. Phase measurements are obtained using a two-dimensional Hartmann wave front sensor. Simultaneous, high-speed shadowgraphs are recorded for visualization of the flow. The two sets of measurements are evaluated for frozen flow using a novel technique of computing correlation coefficient arrays over a sliding two-dimensional window. Finally, Chapter VI summarizes the findings and offers suggested areas for further research.

## II. TURBULENCE MODELS

This chapter presents an overview of existing models for various turbulent media. First, a generally accepted aero-optical model is described, highlighting the basic assumption of statistical isotropy inherent in the model. This is followed by a description of the Kolmogorov model for atmospheric turbulence, also noting typical assumptions. Finally, the notion of a ‘frozen flow’ assumption is addressed with a discussion of its implications on turbulence measurements.

First, some basic definitions regarding stationarity are presented, using the general space-time correlation function as an example. The definitions are consistent with V.I. Tatarski’s, considered the standard in the field of optical propagation through turbulence [13].

Consider a random signal,  $u$ , with spatial coordinates,  $(x, y)$ . The general space-time autocorrelation function (ACF),  $\mathcal{R}_{uu}$  is given by:

$$\mathcal{R}_{uu}(x_1, y_1, t_1; x_2, y_2, t_2) = \mathcal{E} \{u(x_1, y_1, t_1)u^*(x_2, y_2, t_2)\} \quad (2)$$

where  $\mathcal{E}\{\cdot\}$  is the expected value operator, denoting a statistical average. For the moment, we consider a special case of Eq. (2) where  $t_1 = t_2$ , the spatial ACF. The temporal ACF (i.e., where  $(x_1, y_1) = (x_2, y_2)$  and Eq. (2) is evaluated temporally) is discussed with regard to frozen flow approximations in Section 2.4. For the spatial ACF, homogeneity implies that  $\mathcal{R}_{uu}(x_1, y_1; x_2, y_2)$  depends only on the vector separation of  $(x_1, y_1)$  and  $(x_2, y_2)$ . In this case, the ACF reduces simply to  $\mathcal{R}_{uu}(\Delta x, \Delta y)$ , where  $\Delta x = x_2 - x_1$  and  $\Delta y = y_2 - y_1$ . Wide-sense stationarity, in this context, is synonymous with homogeneity [22]. A more restrictive condition is one of isotropy where  $\mathcal{R}_{uu}(x_1, y_1; x_2, y_2)$  depends only on the *scalar* separation of  $(x_1, y_1)$  and  $(x_2, y_2)$ . Isotropy may be viewed as circular symmetry of the two-dimensional ACF, which then reduces Eq. (2) to a single dimensional function,  $\mathcal{R}_{uu}(r)$ , where  $r = \sqrt{(\Delta x)^2 + (\Delta y)^2}$ . The most restrictive condition is one of ergodicity, where the ACF for any single realization of  $u$  is representative of the statistical ACF. The hierarchy of types

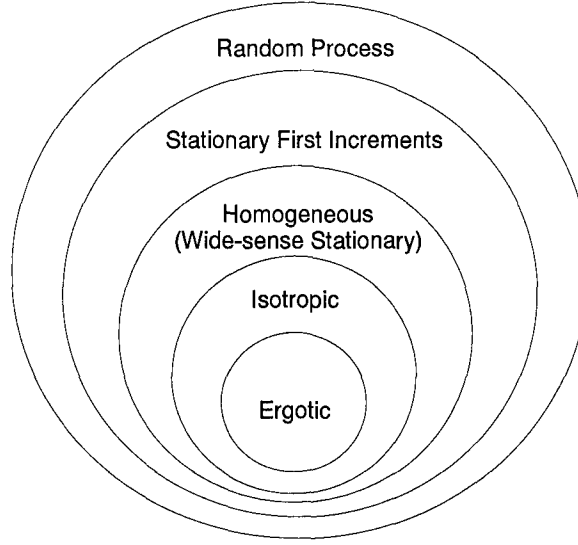


Figure 1. The Hierarchy of Classes of Random Processes

of relevant random processes is illustrated in Fig. 1, analogous to Goodman's hierarchy where an inner circle is a subset of the outer ones [13]. Note that isotropy is a necessary condition for ergodicity, and ergodicity is often imposed by necessity if multiple realizations of a signal are unavailable or inconvenient (for example, see Verhoff[51] for modeling turbulent boundary/shear layers).

Some useful properties of a homogeneous ACF are [13]:

1.  $\mathcal{R}_{uu}(0, 0) = \mathcal{E} \{u^2(x, y)\}$
2.  $|\mathcal{R}_{uu}(\Delta x, \Delta y)| \leq \mathcal{R}_{uu}(0, 0)$
3.  $\mathcal{R}_{uu}(-\Delta x, -\Delta y) = \mathcal{R}_{uu}(\Delta x, \Delta y)$

The first property comes directly from the definition in Eq. (2). This mean square value is a measure of the total power in the process, which sets the upper bound on the ACF as indicated by property two. The third property reflects the Hermitian symmetry of the ACF. These properties will be useful when assessing the ACF results for the free flow and channel flow measurements.

## 2.1 Aero-Optical Model

Airborne-platform flow fields induce three general classes of optical aberrations at a sensor: Strehl loss, beam spread, and beam tilt [11]. The primary model used in aero-optical applications for wave front phase variance ( $\text{rad}^2$ ) is given by [10, 15, 44, 49]

$$\sigma_\phi^2 = 2G^2 k^2 \int_0^\delta \sigma_{\rho'}^2(z) \ell_z(z) dz, \quad (3)$$

where the subscripts  $\phi$  and  $\rho$  denote phase and density, respectively;  $G$  is the Gladstone-Dale constant;  $k = (2\pi/\lambda)$  is the wave number for optical wavelength,  $\lambda$ ;  $\sigma_{\rho'}^2(z)$  is the variance of the density fluctuations in the direction of beam propagation;  $\ell_z(z)$  is the turbulence scale length in the direction of propagation; and  $\delta$  is the path length through the turbulence. For low-speed mixing of dissimilar gases,  $\delta$  is the mixing layer thickness, which is a function of the streamwise location in the flow [5]. The optical waves are assumed to propagate in the  $z$ -direction with negligible refraction [15]. The applicability of the refractionless limit approximation is addressed later in the chapter.

A derivation of Eq. (3), including typical assumptions, is presented here. The derivation follows from first-order geometrical optics, where the index fluctuations are assumed to induce negligible ray deflection over, for example, a thin boundary layer [49]. Thus, the random phase shift at a point  $(x, y)$  is related to the random index fluctuations,  $n'$  by

$$\phi(x, y) = k \int_0^\delta n'(x, y, z) dz. \quad (4)$$

The index fluctuations and density fluctuations,  $\rho'$ , are related by the Gladstone-Dale law,

$$n'(x, y, z) = G\rho'(x, y, z), \quad (5)$$

so that, upon substitution into Eq. (4) we have

$$\phi(x, y) = Gk \int_0^\delta \rho'(x, y, z) dz. \quad (6)$$

The statistics of the phase fluctuations may be characterized by the spatial ACF, defined by Eq. (2), for the random variable  $\phi(x, y)$  and the special case where  $t_1 = t_2$ . Combining Eq. (2) and (6) results in

$$\mathcal{R}_\phi(x_1, y_1; x_2, y_2) = G^2 k^2 \int_0^\delta \int_0^\delta \mathcal{R}_{\rho'}(x_1, y_1, z_1; x_2, y_2, z_2) dz_1 dz_2, \quad (7)$$

where  $\mathcal{R}_{\rho'}(x_1, y_1, z_1; x_2, y_2, z_2)$  is the ACF of the density fluctuations. For a process which is wide-sense stationary in the  $(x, y)$  plane, Eq. (7) reduces to [44]

$$\mathcal{R}_\phi(\Delta x, \Delta y) = G^2 k^2 \int_0^\delta \int_0^\delta \mathcal{R}_{\rho'}(\Delta x, \Delta y; z_1, z_2) dz_1 dz_2, \quad (8)$$

where  $\Delta x = x_2 - x_1$  and  $\Delta y = y_2 - y_1$ . Previous experimental results [44] indicate that, for the variable substitutions

$$u = \frac{z_1 + z_2}{2} \quad \text{and} \quad v = z_2 - z_1, \quad (9)$$

$\mathcal{R}_{\rho'}(\Delta x, \Delta y; z_1, z_2)$  can be represented as  $\mathcal{R}_{\rho'}(\Delta x, \Delta y; u, v)$  which, for a zero-mean process, is of the form

$$\mathcal{R}_{\rho'}(\Delta x, \Delta y; u, v) = \sigma_{\rho'}^2(u) \exp \left\{ -\sqrt{\left( \frac{\Delta x}{l_x(u)} \right)^2 + \left( \frac{\Delta y}{l_y(u)} \right)^2 + \left( \frac{v}{l_z(u)} \right)^2} \right\}. \quad (10)$$

The terms  $l_x(u)$ ,  $l_y(u)$ , and  $l_z(u)$  in Eq. (10) are the turbulence scale lengths in the  $x$ ,  $y$ , and  $z$  directions, respectively. Applying the variable substitution to Eq. (8) yields

$$\begin{aligned} \mathcal{R}_\phi(\Delta x, \Delta y) = G^2 k^2 \left\{ \int_0^{\delta/2} \int_{-2u}^{2u} \mathcal{R}_{\rho'}(\Delta x, \Delta y; u, v) du dv \right. \\ \left. + \int_{\delta/2}^\delta \int_{-2(\delta-u)}^{2(\delta-u)} \mathcal{R}_{\rho'}(\Delta x, \Delta y; u, v) du dv \right\}. \quad (11) \end{aligned}$$

Finally, combining Eq. (10) and (11), assuming that  $\delta \gg l_z$  we obtain Eq. (3) [44],

$$\mathcal{R}_\phi(0, 0) = \sigma_\phi^2 \approx 2G^2 k^2 \int_0^\delta \sigma_{\rho'}^2(z) \ell_z(z) dz. \quad (12)$$

Hence, applying the model given by Eq. (3) requires assumptions on wide-sense stationarity and scale size of the turbulence. For the turbulent mixing layers generated in this research, an estimate of the spatial ACF for the random phase fluctuations was computed. The results for this calculation are presented in Chapters III and IV.

## 2.2 Atmospheric Model

The Kolmogorov model for turbulence is widely accepted in the analysis of optical propagation through the turbulent atmosphere [13, 30]. For isotropic turbulence, the relative abundance of eddies with dimensions  $L = 2\pi/\kappa$ , where  $\kappa$  is the wavenumber scalar, can be described by the power spectral density (PSD) for index fluctuations,  $\Phi_n(\kappa)$ , which is given by

$$\Phi_n(\kappa) = 0.033 C_n^2 \kappa^{-\frac{11}{3}}, \quad (13)$$

where  $C_n^2$  is called the structure constant of the index fluctuation and is a local measure of the strength of the fluctuations. In atmospheric turbulence, the phase structure function of the random process  $\phi(x, y)$ , may be used to characterize the effects of refractive index fluctuations on optical system performance. The phase structure function is defined by

$$D_\phi(x_1, y_1; x_2, y_2) = E \left\{ [\phi(x_1, y_1) - \phi(x_2, y_2)]^2 \right\}. \quad (14)$$

When the random phase  $\phi(x, y)$  is stationary in first increments, the phase structure function reduces to a two-dimensional function, depending only on the coordinate differences  $\Delta x$  and  $\Delta y$ . Additionally, when the phase variation is a zero-mean, Gaussian random process; e.g. in the turbulent atmosphere, the average optical transfer function (OTF), for spatial frequency

variables  $\nu_x$  and  $\nu_y$ , is expressed in terms of the structure function as [13]

$$\overline{\mathcal{H}}_s(\nu_x, \nu_y) = \exp \left\{ -\frac{1}{2} D_\phi(\bar{\lambda} f \nu_x, \bar{\lambda} f \nu_y) \right\}, \quad (15)$$

where  $f$  is the imaging system focal length. In addition, the average OTF of the imaging system,  $\overline{\mathcal{H}}(\nu_x, \nu_y)$ , may be expressed as the product [13]

$$\overline{\mathcal{H}}(\nu_x, \nu_y) = \mathcal{H}_0(\nu_x, \nu_y) \overline{\mathcal{H}}_s(\nu_x, \nu_y), \quad (16)$$

where  $\mathcal{H}_0$  is the OTF of the imaging system in the absence of the turbulence. Thus, evidence of stationarity in first increments, a less restrictive case than wide-sense stationarity, is sufficient for generating tractable mathematical expressions for the average OTF of the random turbulent field. The average OTF provides predictions for the performance of the optical imaging system in the presence of the turbulent field. When the phase fluctuations are statistically isotropic, Eq. (14) reduces to a one-dimensional function,  $D_\phi(r)$ , where  $r = \sqrt{(\Delta x)^2 + (\Delta y)^2}$ . In regions where  $C_n^2$  is constant, the Kolmogorov model for the PSD in Eq. (13) results in a phase structure function given by [13]

$$D_\phi(r) = 2.91 \left( \frac{2\pi}{\lambda} \right)^2 C_n^2 z r^{5/3}, \quad (17)$$

where  $z$  is the propagation path length within the turbulence. Eq. (17) is referred to as the Kolmogorov five-thirds power law. The model has been verified using both laboratory measurements, and direct airborne measurements of the atmosphere [30]. More recently, results have been reported on phase structure function estimates using wave front phase measurements for laboratory-generated, free-turbulent heated air [27]. These experiments were designed to simulate atmospheric turbulence. The conclusion was that statistical isotropy was a valid assumption in the free atmosphere; hence, the phase structure functions could be modeled by the Kolmogorov five-thirds power law. In contrast, the present research investigates the optical phase effects induced by turbulent mixing layers. The molecular



mixing of dissimilar gases generates large density fluctuations in the flow, not present in the low-velocity heated air [45]. These density fluctuations, in turn, induce anisotropic phase fluctuations.

It should be noted that the Earth's atmosphere is not entirely isotropic. Measurements from space platforms have identified horizontally stratified non homogeneities of the refractive index in regions of the stratosphere and upper troposphere. These regions cannot be accurately modeled using Kolmogorov statistics due to the strong anisotropy [14]. In the present research, a technique for characterizing the anisotropy of laboratory-generated, turbulent mixing layers is introduced. This technique may prove to be equally valid for the anisotropic regions of the atmosphere.

Imaging system performance is often expressed in terms of the average point spread function (PSF) and the Strehl Ratio (SR). The average PSF is defined as [13]

$$\bar{s}(x, y) = \mathcal{F}^{-1} \left\{ \overline{\mathcal{H}}(\nu_x, \nu_y) \right\}, \quad (18)$$

where  $\mathcal{F}^{-1}$  is the two-dimensional inverse Fourier transform operator. The SR is defined as the ratio of the on-axis intensity of the turbulence-aberrated beam,  $I$ , to the on-axis intensity of an unaberrated beam,  $I_0$ . Hence, for simplicity, the SR may be computed from the PSF by

$$\frac{I}{I_0} = \frac{\bar{s}(x_a, y_a)}{s_0(x_a, y_a)}, \quad (19)$$

where the subscript,  $a$ , refers to the on-axis point, and  $s_0(x, y)$  is the PSF of a diffraction-limited system. Note that from Eqs. (18) and (19), the SR may be equivalently expressed as the normalized volume under the OTF of the aberrated system; that is [12]

$$SR = \frac{\int \int_{-\infty}^{\infty} \mathcal{H}(\nu_x, \nu_y) \Big|_{aberrated} d\nu_x d\nu_y}{\int \int_{-\infty}^{\infty} \mathcal{H}(\nu_x, \nu_y) \Big|_{unaberrated} d\nu_x d\nu_y}. \quad (20)$$

The present research introduces an alternate measure of image quality which replaces the diffraction-limited PSF in the denominator of Eq. (19) with the PSF of the imaging system in the absence of turbulence, a measurable quantity. Replacing the formal Strehl definition with a relative measure of image degradation is not unusual in analysis of optical systems [7, 50]. Furthermore, the relative SR provides a more meaningful comparison with the other SR models presented below.

The conventional aero-optical technique for computing the SR is based on the on-axis, rms phase variance,  $\sigma_\phi^2$ , by [28]

$$\frac{I}{I_0} = \exp \left\{ -\sigma_\phi^2 \right\}. \quad (21)$$

Here, the total wavefront variance is the sum of the phase variance due to the turbulent mixing layer and the phase variance due to the imaging system [50]. But the phase variance due to the imaging system is zero; hence, the Strehl ratio given by Eq. (21) is a relative measure.

For mixing of dissimilar gases, Eq. (21) can be approximated using [3]

$$\frac{I}{I_0} = \exp \left\{ -0.5k^2\alpha^2\Delta n^2\delta^2 \right\}, \quad (22)$$

where  $\alpha$  is the scalar turbulence intensity, experimentally determined to be approximately 0.15 for mixing layers [52];  $\Delta n$  is the refractive index difference for the two mixing gases; and  $\delta$  is the width of the mixing layer. Again, Eq. (22) is based on the assumption of wide-sense stationarity [52] and is a relative measure.

In comparison, Eq. (19) is obtained with no assumptions on stationarity; however, a tractable solution may be achieved when the average OTF can be represented by Eq. (15). For the measurements presented in this research, an estimate of the structure function for the random phase fluctuations was computed. The results for this calculation are presented in Chapters III and IV.

### 2.3 Refractionless Limit Approximation

This section addresses the limitation imposed by the geometrical optics assumption. The geometrical optics approximation for light propagation through a region of fluctuating density is valid when a ray propagating in the  $z$  direction leaves the region at approximately the same  $(x, y)$  position it entered the region [13]. This is a valid approximation when the integrated density of the flow evaluates to a small fraction of a radian. To quantify the displacement of a ray after propagating through a gas flow, we model the flow as a phase-only diffraction grating [25] with period equal to the smallest scale size present in the flow,  $l_0$ . This is analogous to the approach taken by Lee and Harp [25], where atmospheric turbulence-induced aberrations were decomposed using the Fourier transform. The diffraction effects were computed by first analyzing the effects of a single spatial frequency in the aberration, and then integrating over all spatial frequencies. For an incident beam the angle of the first diffracted order leaving a diffraction grating is given by [16]

$$\theta_{\text{out}} = \sin^{-1} \left( \frac{\lambda}{l_0} + \sin \theta_{\text{in}} \right), \quad (23)$$

where  $\theta_{\text{in}}$  and  $\theta_{\text{out}}$  are the incident and exiting angles measured with respect to the surface normal of the grating, respectively. Using  $l_0$  as the spatial period of the diffraction grating results in the maximum diffraction angle. The spatial displacement of a ray which is normally incident to the grating, after propagating a distance,  $d$ , can be approximated for small departure angles by the product  $\theta_{\text{out}}d$ . For the gas flow region, this ray tracing process is more accurately applied by stacking  $N$  layers of spatial gratings, each separated by a propagation distance,  $d$ , such that the product,  $Nd$  equals the total propagation distance [39]. A reasonable separation of layers for this model is  $d = l_0$ . Hence, the total displacement of the ray can be computed by iteration through the  $N$  layers.

As an example, consider the case of a 2 cm thick layer which has a smallest scale size of 2 mm. Using the model described above, we would assume the refractive effects of the layer could be approximated by 10 spatial gratings with a period of 2 mm, separated by 2 mm

along the direction of light propagation. A ray entering this region would be displaced by  $34 \mu\text{m}$  and depart the region with a deflection of  $0.003 \text{ rad}$ .

A reasonable criterion for determining how much displacement of the rays can be tolerated is to restrict the total displacement to be less than or equal to the lateral shear applied to the wave at the shearing interferometer [37]. This criterion is addressed in the Experimental Setup section in Chapter III.

#### 2.4 Frozen-Flow Turbulence Model

Measurements in the atmosphere and in laboratory-generated turbulence indicate that velocity fluctuations are generally an order of magnitude less than the mean flow velocity [30, 45]. This implies that changes in the fluctuations with respect to some time interval, at a fixed point, is predominantly due to the movement of the spatial fluctuations at the mean stream velocity. The Taylor frozen-flow approximation, first introduced by Geoffrey I. Taylor, states that over a small time interval,  $t_2 - t_1 = \tau$ , the turbulent fluctuations have a constant velocity, in space and time, equal to the mean velocity in the flow. Thus, over a sufficiently small value of  $\tau$ , frozen flow implies [45]

$$u(x, y, t) \approx u(x - U\tau, y - U\tau, t + \tau), \quad (24)$$

where  $u$  is the velocity fluctuation, and  $U$  is the mean velocity. Substituting this approximation into the space-time ACF given by Eq. (2) results in

$$\mathcal{R}_{uu}(x, y, t; x, y, t + \tau) = \mathcal{R}_{uu}(x, y, t; x - U\tau, y - U\tau, t); \quad (25)$$

i.e., the temporal ACF is represented by the spatial ACF for a fixed time. Note that the same approximations may be applied to the structure function. In fact, Monin [30] distinguishes between longitudinal (in the direction of the flow) and lateral (transverse direction) components of the velocity field in expressing the spatial and temporal structure functions. This convention is appropriate, as the scale sizes are generally directionally dependent [48], and the time

interval,  $\tau$ , for which the frozen flow approximation is valid will be different for the two directions. In summary, the tangible benefit of the frozen flow assumption is that it converts a time shift into a spatial shift, enabling spatial analysis over relatively large regions of a flow field.

In a real flow the velocity fluctuations evolve with time; hence, the validity of the frozen-flow approximation lies in the specific time interval designated. Frozen turbulence has been shown to be an accurate approximation for isotropic turbulence; however, in the case of non-homogeneous turbulence, the mean velocity is not constant, and the validity of a frozen flow will, at best, encompass very small time scales [15, 30]. Verification of the approximation requires simultaneous measurements of highly-resolved spatial and temporal characteristics of the flow.

The frozen-flow approximation is qualitatively assessed for a specific mixing layer in Chapter V, where high-speed (i.e., 1 kHz) measurements of wave front phase and shadow-graphs are reported.

### *III. FREE TURBULENT MIXING LAYERS*

#### *3.1 Overview*

Light waves passing through turbulent mixing layers are aberrated by index-of-refraction fluctuations in the flow [48]. These index-of-refraction fluctuations arise from random spatial and temporal fluctuations in the gas density. The phase of an optical wave that propagates through a turbulent region will be aberrated, degrading the performance of imaging and beam projection systems. Adaptively correcting for these phase aberrations requires an understanding of the spatial and temporal characteristics of the turbulence; hence, a great deal of research has been dedicated to developing various techniques for visualizing the turbulent flow (e.g., shadowgraphs, schlieren, light sheets, interferometry) and predicting the flow properties. The classical model for optical effects in turbulent flow assumes the refractive index fluctuations are homogeneous and isotropic, providing predictions for Strehl ratio [3]. The model tends to overestimate the optical degradation for anisotropic flows [15]. Additionally, the model has not been validated for complex flows such as the turbulent mixing of dissimilar gases [15].

This chapter describes the use of a shearing interferometer wave front sensor to obtain slope measurements of perturbed wave fronts after propagating through free turbulence. Free turbulence is described as a high-Reynolds-number shear flow in an open ambient fluid; i.e., its motion is unaffected by solid boundaries [54]. Unbounded flow is more difficult to model than pipe or channel flow (bounded) since, in conjunction with development in the streamwise direction, the unbounded flow spreads laterally into the ambient fluid. The evolving flow remains non-homogeneous, making modeling extremely difficult unless assumptions such as self-similarity are applied [45]. Examples of free turbulence are turbulent jets, turbulent wakes behind rigid bodies, and turbulent mixing layers occurring on the boundary between streams of dissimilar gases. Characterization of free turbulent flows is important for naturally-occurring phenomena as well as for numerous engineering applications. Experimental investigations of

free turbulence have led to useful semi-empirical theories; however, the understanding of the physical nature of free turbulence is still, at best, limited [30].

For the wave front slope measurements reported in this research, a turbulence generator was used to mix Helium and Nitrogen gas at a sharp trailing edge, forming an unbounded mixing layer surrounded by ambient air. This resulted in three distinct mixing layers: air/He,  $N_2$ /He, and  $N_2$ /air, having density ratios of approximately 7.2, 7.0, and 1.0 respectively. The slope measurements were used to reconstruct wave front phase surfaces. Shearing interferometers overcome some of the weaknesses of other techniques for sensing density fluctuations in gas flows. The shearing interferometer is non-invasive and requires that only a single beam be passed through the flow, unlike holographic measurements which require a separate reference beam. The shearing interferometer has been shown to be an excellent flow visualization tool [17]; however, the application for the current research was to generate a measured data set of random phase fluctuations for a given location in the turbulent mixing layer. The intent was to capture the random index-of-refraction fluctuations by means of phase reconstructions over a sufficiently large set of measured data. Statistical autocorrelation functions and structure functions were calculated, and the results were assessed for applicability of the aero-optical and atmospheric models described in Chapter II.

The chapter begins with a description of the experimental setup used to generate and compute an ensemble of phase reconstructions of aberrated light waves. Next, a set of statistical calculations is performed on the phase surfaces and the results are assessed for statistical homogeneity and isotropy. Then, a set of modeling parameters is computed, based on the structure functions, leading to a Strehl ratio prediction. Finally, this Strehl ratio is related to the Reynolds number in the flow.

### 3.2 *Experimental Setup*

The optical bench used for the free turbulence experiments is shown in Fig. 2. A 2 cm diameter, collimated laser beam was transmitted through the turbulent flow at various distances from the exit of the turbulence generator. The edge of the turbulent flow was imaged

onto the entrance pupil of the wave front sensor. The lens pair, Lens 1 and Lens 2, provides a magnification of 0.5 so that a 1 cm diameter image of the perturbed beam was presented at the pupil plane of a lateral shearing interferometer. The image filled approximately 50% of the pixels in a  $512 \times 484$  detector array. This resulted in a single pixel subtending a region of approximately  $47 \mu\text{m} \times 54 \mu\text{m}$  in the plane of the turbulence. The lateral shear for both the  $x$  and  $y$  legs of the shearing interferometer was set to 1 pixel to enable detection of strong density fluctuations [37]. A reasonable criterion for determining how much displacement of the rays through the turbulence can be tolerated for the geometrical optics assumption to be valid, is to restrict this displacement to be less than or equal to the lateral shear. Using the spatial grating model described in Chapter II, the displacement was determined to be 34 micrometers for a 2 cm thick layer and a smallest scale size of 2 mm. Therefore, the geometrical optics assumption is valid for shears down to one pixel.

The 1 cm image was split at the non-polarizing beam splitter, providing a path to the optional camera. For the free turbulence measurements, this camera remained inactive during the phase measurements.

A turbulent shear layer generator was used to create a suitable gas flow to test this method [20]. The shear layer generator is shown in Fig. 3. The shear layer generator allows streams of two gases, generally with different speeds and densities, to mix at a sharp trailing edge, forming a shear layer flow. The outer dimensions of the box holding the shear layer generator are  $14 \text{ cm} \times 14 \text{ cm} \times 43 \text{ cm}$ . The box is constructed from 2.54 cm thick aluminum, and all seams were sealed with o-rings to prevent gas leaks. Each gas enters a  $9 \text{ cm} \times 4.5 \text{ cm}$  stilling chamber through 0.635 cm plastic tubing, and exits through a  $2.5 \text{ cm} \times 1.25 \text{ cm}$  opening. The curved taper of the output end of the shear layer generator was specified using a third-order polynomial to provide a smooth reduction in the cross section of the flow. This polynomial is given by

$$y = 0.0080x^3 - 0.1120x^2 - 0.0005x + 4.4695, \quad (26)$$



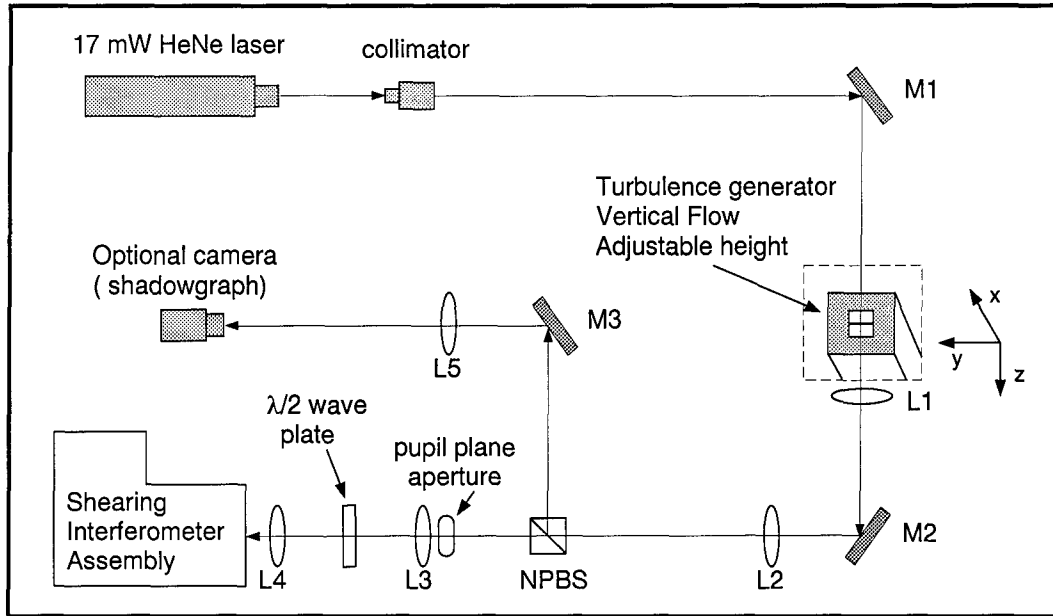


Figure 2. Optical bench used to obtain phase measurements for a laser beam propagating through the free turbulent mixing layer.

where the center of the splitter plate is chosen as the  $x$  axis, the  $x = 0$  point is 10 cm to the left of the output opening,  $y$  is the distance of the tapered surface from the  $x$  axis, and all distances are specified in cm. There is no particular importance attached to the choice of the tapering function in Eq. (26). The tapering function in Eq. (26) simply provides a smooth reduction in the cross section of the chamber over a reasonable distance. A pyramid filled with 0.5 cm holes was placed in each chamber to distribute the flow of gas evenly across the chamber. Honeycomb and screens were placed in the tunnels to straighten the flow and reduce free stream turbulence. The splitter plate was made of 0.32 cm thick bronze plane which was tapered over 10 cm to a sharp edge at the output opening.

The splitter plate in the turbulence generator was oriented in a direction normal to the propagation vector of the laser beam. Hence, for propagation in the  $z$  direction and a vertical flow of the gases in the  $x$  direction, the shear layer of the mixing gases is in the  $(x, y)$  plane. In addition to the He/N<sub>2</sub> mixing layer, the unbounded flow interacts with the surrounding

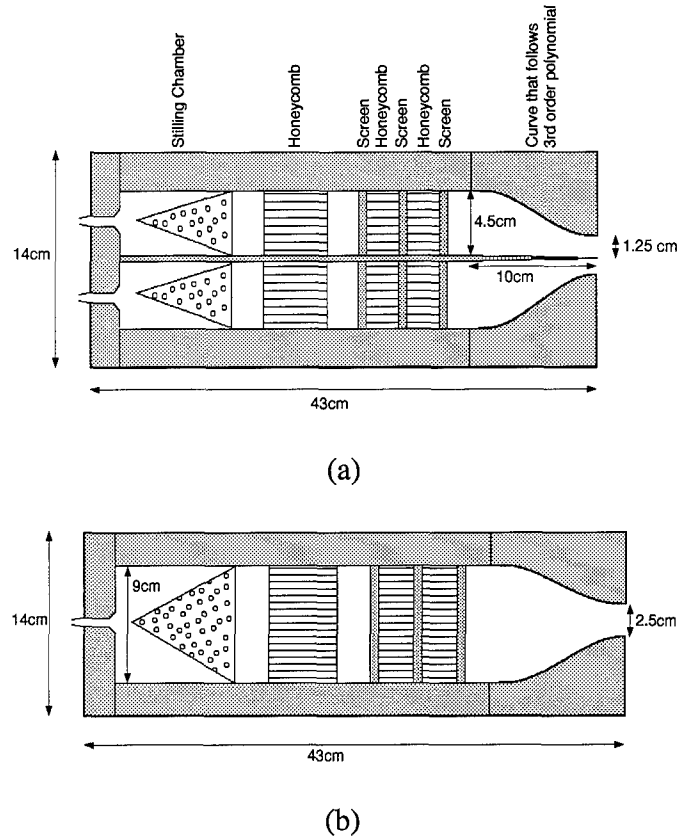


Figure 3. Shear layer turbulence generator: (a) Side view of the shear-layer turbulence generator; and (b) Top view of the shear-layer turbulence generator.

ambient air, resulting in two additional mixing layers. Fig. 4 shows a schematic of the flow field accompanied by the axis labeling convention.

Gas velocities were measured for every run using a micromanometer to measure the difference between the atmospheric pressure and the pressure of each gas leaving the chamber,  $\Delta P$ . The gas velocities were calculated using a form of Bernoulli's equation

$$v = \sqrt{\frac{2\Delta P}{\rho}}, \quad (27)$$

where  $\rho$  is the gas density, which for an ideal gas is given by

$$\rho = \frac{p}{RT}, \quad (28)$$

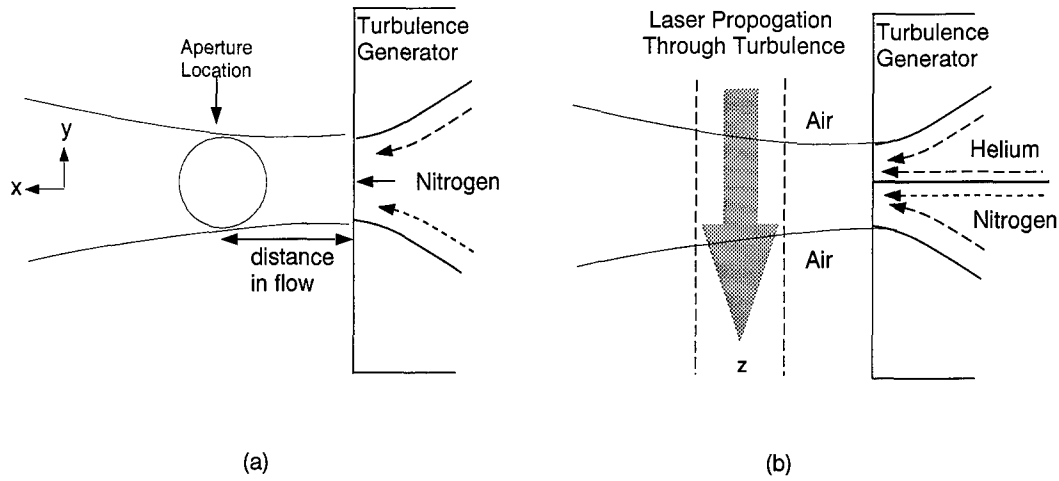


Figure 4. Flow field schematic. (a) The orientation of the turbulence chamber and an aperture location as viewed from the side. (b) Laser propagation through the shear layer as viewed from the top. The  $N_2/He$  mixing layer is in the center of the flow.

where  $p$  is the pressure of the gas,  $R$  is the engineering gas constant, and  $T$  is the gas temperature. The engineering gas constant for Nitrogen is  $R = 296.5 \text{ N} \cdot \text{m/kg} \cdot \text{K}$ , and for Helium it is  $R = 2079.8 \text{ N} \cdot \text{m/kg} \cdot \text{K}$ . The micromanometer measured  $\Delta P$  in cm of water with an accuracy of  $\pm 0.00127 \text{ cm}$ . This translates to a velocity uncertainty of  $\pm 0.09 \text{ m/sec}$  for Helium and  $\pm 0.07 \text{ m/s}$  for Nitrogen. For all experiments described in this research, the gas velocities remained fixed at  $8.5 \text{ m/sec}$  for the He and  $1.5 \text{ m/sec}$  for the  $N_2$ .

The Reynolds number,  $Re_x$  for each mixing layer interface is given by [45]

$$Re_x = \frac{x \Delta U}{\eta}, \quad (29)$$

where  $x$  is the streamwise distance from the generator output,  $\Delta U$  is the velocity difference of the two mixing gases, and  $\eta$  is the kinematic viscosity; i.e., the ratio of the absolute viscosity to the gas density. Here,  $\eta_{air}$  is used for all three mixing layers to be consistent with similar studies [3, 55]. Using  $\eta_{air}$  is a very good approximation for even the  $N_2/He$  layer since the density of  $N_2$  is approximately equal to that of air [5]. Hence,  $Re_x/x$  for each layer differs only by  $\Delta U$ . The width of the mixing layer region, which is a function of the  $N_2$  to He density ratio  $\rho_r$ , the low-speed to high-speed velocity ratio  $U_r$ , and downstream location may

Table 1. Summary of Fluid Parameters for the Free Mixing Layers.

Mixing Layer	$\Delta U$ (m/sec)	$Re_x/x$ (cm <sup>-1</sup> )	$\delta(x)/x$	$Re_\delta/x$ (cm <sup>-1</sup> )
air/He	8.5	5397	0.76	4102
He/N <sub>2</sub>	7.0	4444	0.41	1822
N <sub>2</sub> /air	1.5	952	0.37	352

be approximated by [5]

$$\delta(x) \approx x C_\delta \frac{(1 - U_r)(1 + \sqrt{\rho_r})}{2(1 + U_r \sqrt{\rho_r})} \left\{ 1 - \frac{(1 - \sqrt{\rho_r})/(1 + \sqrt{\rho_r})}{1 + 2.9(1 + U_r)/(1 - U_r)} \right\}, \quad (30)$$

where the value of the coefficient,  $C_\delta$ , varies with initial conditions of the flow. The range of  $C_\delta$  has been empirically determined to be [5]

$$0.25 \leq C_\delta \leq 0.45. \quad (31)$$

Applying the approximation for  $\delta(x)$ , the total path of propagation through the region of mixing may be estimated by the sum of the three mixing layers. From Eq. (29) and Eq. (30), a local Reynolds number,  $Re_\delta$  may be obtained, which is given by [55]

$$Re_\delta = \delta(x) \frac{Re_x}{x}. \quad (32)$$

A summary of the fluid parameters is given in Table 1, where  $\delta(x)$  was calculated using an average  $C_\delta$  of 0.37.

The cameras used for this experiment have output consistent with standard television format, providing one interlaced field to a monitor each 16.67 ms. However, within the field time of 16.67 ms the cameras were read out twice. One readout was used to clear any charge which accumulated in the time leading up to the actual exposure for the wave front measurement. The second readout was for the actual wavefront exposure time which was set at 0.5 ms for all experiments reported here. The simultaneous measurements over a

two-dimensional space imply that frozen turbulence assumptions are not required to infer the effects of the flow in the streamwise direction, as is required with other techniques [21, 29]. Hence, the ACF and structure function can be measured more precisely over a range of vector separations [30]. With the gas velocities fixed at 8.5 m/sec for the Helium and 1.5 m/sec for the Nitrogen, the optical phase perturbations were measured at six locations in the flow. The locations were centered on 1.25 cm, 5.75 cm, 8.25 cm, 10.75 cm, 18.75 cm, and 28.75 cm downstream of the exit of the turbulence generator. These locations can be equivalently expressed in terms of a dimensionless  $X/D$  parameter, where  $X$  is the location of the beam in the flow, and  $D$  is the length of one side of the exit nozzle. Thus, for the present experiment, the  $X/D$  locations are approximately 0.5, 2.3, 3.3, 4.3, 7.5, and 11.5.

The shearing interferometer was used to obtain slope measurements of perturbed wave fronts after propagating through the free turbulent flow. The shearing interferometer senses wave front slope in two orthogonal directions. Phase difference measurements for each direction are obtained from three phase-shifted interference images using a three-bin algorithm [41]. The wave front phase surfaces are then reconstructed using an algorithm developed by Hudgin [19]. A thorough description of the lateral shearing interferometer can be found in Magee [26].

The total reconstructed phase represents the sum of the density fluctuations due to the turbulent mixing layer and any deterministic phase perturbations induced by imperfections in the imaging optics. The deterministic effects can be measured by performing a phase reconstruction in the absence of turbulence. This reference phase measurement is then subtracted from subsequent phase reconstructions, resulting in phase fluctuations due to turbulent mixing only. An example of a reconstructed phase surface is shown in Fig. 5, where the deterministic effects have been subtracted. Fig. 5 is one realization for the aperture centered at 10.75 cm in the flow, and is representative of the average dynamic range observed at that location. Note that the  $x$  and  $y$  axis units in Fig. 5 are samples. The sample spacing in the  $x$ -direction (streamwise) is approximately 95  $\mu\text{m}$ , and the sample spacing in the  $y$ -direction (cross-stream) is approximately 105  $\mu\text{m}$ . Additionally, the units for the phase are waves,

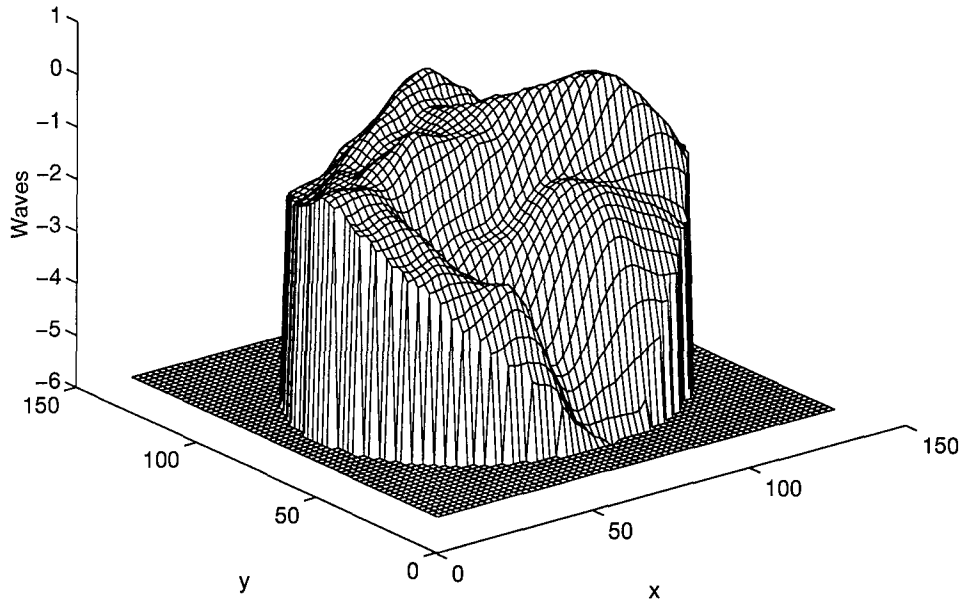


Figure 5. Reconstructed wavefront phase. Deterministic optical system effects have been removed. Flow is in +x direction, propagation is in +z direction. Sample spacing in  $x$  is  $95 \mu\text{m}$ ; sample spacing in  $y$  is  $105 \mu\text{m}$ .

which may be converted to radians by a  $2\pi$  multiplication. Fig. 5 demonstrates the utility of the shearing interferometer as a flow visualization tool. An ensemble of these phase surfaces was used as a means to characterize the random fluctuations in the turbulent flow. Section 3.3 describes the statistical calculations performed.

### 3.3 Statistical Calculations

In this section the results of the ACF and the structure function calculations are presented. First, a discussion of the general technique used for the statistical calculations, including notation and terminology, is provided. The random fluctuating phase was obtained by removing any underlying average phase across the measurement ensemble. The phase

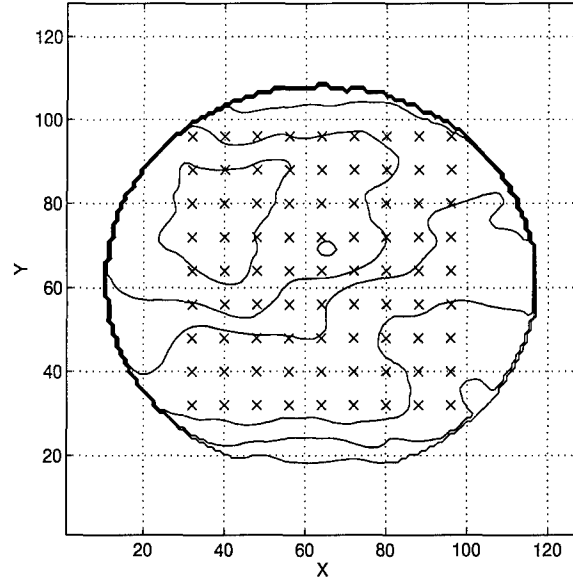


Figure 6. Surface contour of one phase realization,  $\phi'(x, y)$ , with overlay of 81 anchor points. Each 'x' indicates an anchor point. Sample spacing in  $x$  is  $95 \mu\text{m}$ ; sample spacing in  $y$  is  $105 \mu\text{m}$ . Spacing between each anchor point is eight samples.

surface shown in Fig. 5 can be represented as

$$\phi_{meas}(x, y) = \phi_{avg}(x, y) + \phi'(x, y), \quad (33)$$

where  $\phi_{avg}(x, y)$  is the deterministic, average phase and  $\phi'(x, y)$  is the random fluctuating phase to characterize. Hence, for each measurement ensemble,  $\phi_{avg}(x, y)$  was computed, then this value was subtracted from each realization to obtain  $\phi'(x, y)$ .

The reconstructed phase surfaces are  $128 \times 128$  arrays. To reduce computational complexity and allow the assumptions of homogeneity and isotropy to be tested, statistical calculations were conducted on a sample set of 81 points, equally spaced across the aperture. These will be referred to as anchor points. Fig. 6 shows an example of one phase realization,  $\phi'(x, y)$ , displayed as a surface contour with an overlay of the 81 anchor points, where the  $x$  and  $y$  spacing between each anchor point is eight samples. This grid of anchor points was used for the ACF and structure function calculations for all free turbulence measurements. All statistical calculations were based on an ensemble size of 160 realizations. This ensemble

size was determined by evaluating the sample-based signal to noise ratio (SNR). For a set of random variables,  $[f_1, \dots, f_n]$ , the  $n$ -sample SNR is given by [38, 33]

$$\text{SNR}_n = \sqrt{n} \left[ \frac{\bar{f}}{(\bar{v})^{1/2}} \right], \quad (34)$$

where  $\bar{f}$  is the sample-based estimate of the mean of  $f_i$ , defined by

$$\bar{f} = \frac{1}{n} \sum_{i=1}^n f_i \quad (35)$$

and  $\bar{v}$  is the sample-based estimate of the variance of  $f_i$ , defined by

$$\bar{v} = \frac{1}{n-1} \sum_{i=1}^n (f_i - \bar{f})^2 \quad (36)$$

Eq. (34) is appropriate since the 16.67 ms delay between camera fields is sufficient for the mixing volume in the optical path to completely change several times, and hence the realizations of the phase,  $\phi'(x, y)$  are independent. Using this technique, Eq. (34) may be computed for the random variable  $[\phi'_i(x, y)\phi'_i(x + \Delta x, y + \Delta y)]$ , so that the sample mean becomes an estimate of the ACF given by Eq. (2) for  $n$  samples. For an ensemble of 160 realizations, the SNR is approximately 8.5. When Eq. (34) is computed for the random variable  $[\phi'_i(x, y) - \phi'_i(x + \Delta x, y + \Delta y)]^2$ , the sample mean becomes an estimate of the structure function given by Eq. (14) for  $n$  samples, and the SNR is approximately 10 for 160 realizations.

**3.3.1 Autocorrelation Function.** For clarity, the discussion is initially limited to a single location in the turbulent flow, where the aperture is centered at 5.75 cm from the exit of the turbulence generator (see Fig. 4). An estimate of the statistical ACF given by Eq. (2) may be obtained from a finite number of experimental measurements using [22]

$$\hat{\mathcal{R}}_\phi(x, y; x + \Delta x, y + \Delta y) = \frac{1}{N} \sum_{i=1}^N \phi'_i(x, y)\phi'_i(x + \Delta x, y + \Delta y), \quad (37)$$



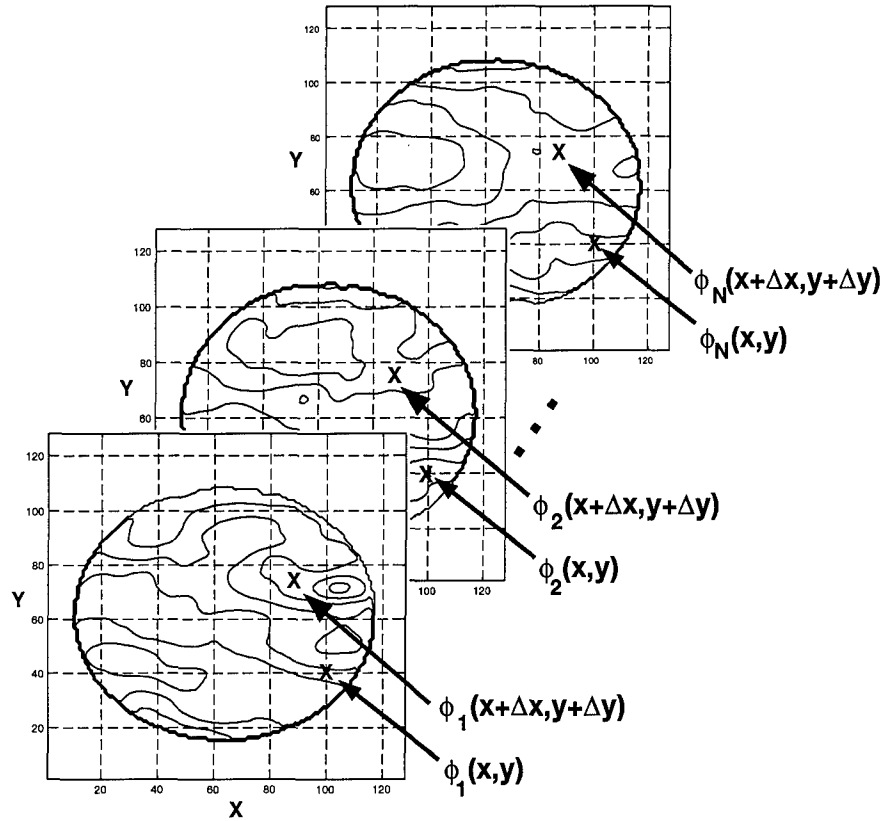


Figure 7. Pictorial representation of the operation performed to obtain the statistical ACF for a single grid point.

where  $N$  is the number of realizations of the wave front phase. For each anchor point, Eq. (37) was computed for  $\Delta x$  and  $\Delta y$  on an interval of  $-10$  samples to  $+10$  samples using an ensemble of 160 realizations of  $\phi'_i(x, y)$ . Fig. 7 shows a pictorial representation of the operation used to compute the statistical ACF for a single grid point.

Eq. (37) is a four-dimensional function; however, for a single anchor point, it reduces to a two-dimensional function of  $\Delta x$  and  $\Delta y$ . Figs. 8 and 9 show the ACF surface contours for a sample set of eight anchor points for the aperture centered at 5.75 cm. For the random process  $\phi'(x, y)$  to be wide-sense stationary, all anchor points on the sample grid must exhibit approximately the same ACF, indicative of the  $\hat{\mathcal{R}}_\phi(\Delta x, \Delta y)$  functional form. Apparent from the eight sample contours, this feature is not observed. Although several anchor points from

the phase grid displayed similar ACF surfaces, none of the points satisfied the properties of the homogeneous ACF, listed in Chapter II. For example, referring to any of the sample anchor points, it is seen that the maximum value from the ACF does not occur at  $\mathcal{R}_{uu}(0, 0)$ . A similar result was obtained for the other five aperture locations in the turbulent flow. The conclusion is that the free turbulent mixing layers generated in this experiment are not stationary in the wide sense. Hence, application of the aero-optical model given by Eq. (3) is not appropriate. The Strehl ratio estimates which are derived from the aero-optical model, as given in Eqs. (21) and (22), were computed and compared to the Strehl ratio obtained from structure function calculations. These results appear later in this chapter.

**3.3.2 Structure Function.** Again, the discussion is initially limited to a single location in the turbulent flow, where the effective aperture is centered at 5.75 cm. An estimate of the statistical phase structure function, given by Eq. (14), may be obtained from a finite number of experimental measurements using

$$\hat{D}_\phi(x, y; x + \Delta x, y + \Delta y) = \frac{1}{N} \sum_{i=1}^N [\phi'_i(x, y) - \phi'_i(x + \Delta x, y + \Delta y)]^2. \quad (38)$$

Analogous to the ACF, an estimate of the phase structure function was computed for  $\Delta x$  and  $\Delta y$  on an interval of  $-10$  samples to  $+10$  samples using an ensemble of 160 realizations. Figs. 10 and 11 show the structure function for eight representative anchor points. Again, for a single anchor point, the structure function is a two-dimensional function of  $\Delta x$  and  $\Delta y$ . For the random process  $\phi'(x, y)$  to be stationary in first increments, all anchor points must exhibit approximately the same structure function. This feature is apparent in the eight-sample set shown in Figs. 10 and 11; i.e., the grid points exhibit similar elliptical contours, symmetric about  $\hat{D}_\phi(0, 0)$ . In general, local homogeneity was a good approximation for anchor points located near the center of the aperture. The absence of statistical homogeneity at the edge of the aperture may be due to imprecise phase reconstruction by the Hudgin algorithm, as documented by Southwell [43]. In addition, the edges of the turbulence generator produce shed vortices which appear as large-scale coherent structures on the edge of the camera interference

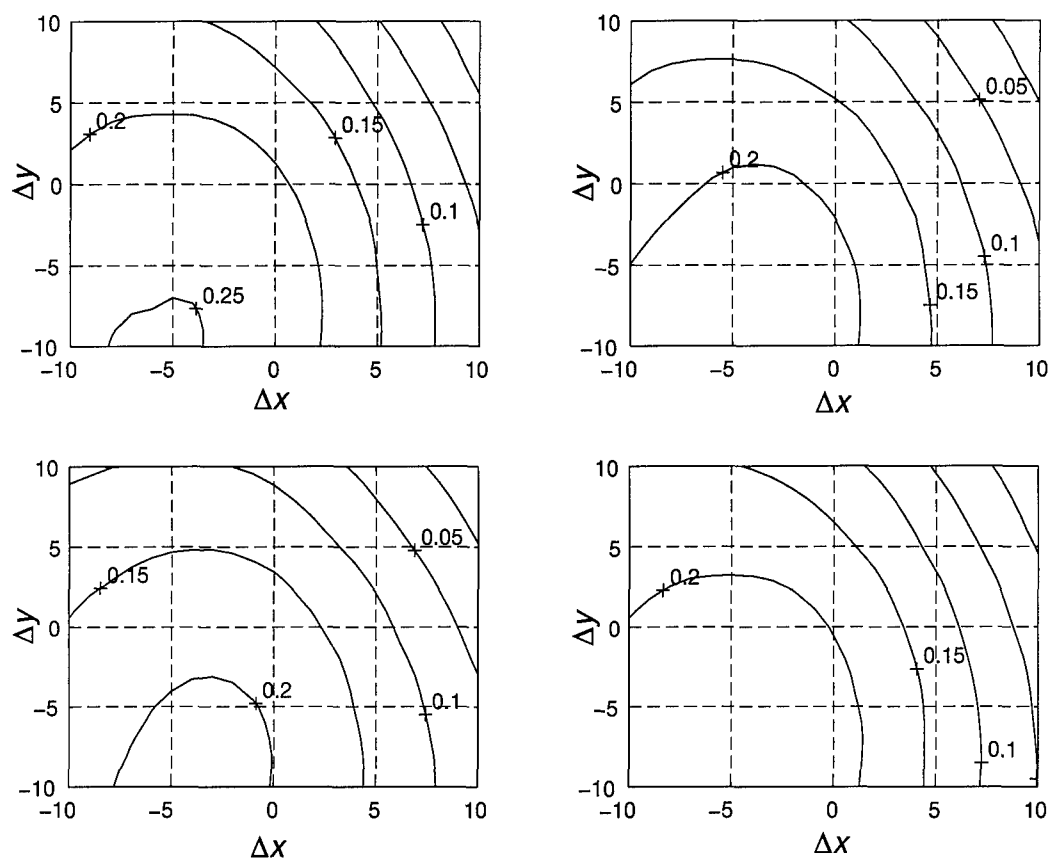


Figure 8. Surface contour of the autocorrelation function for four representative anchor points from the sample grid. Contours are in units of waves<sup>2</sup>. Each unit of  $\Delta x$  and  $\Delta y$  is  $95 \mu\text{m}$  and  $105 \mu\text{m}$ , respectively.

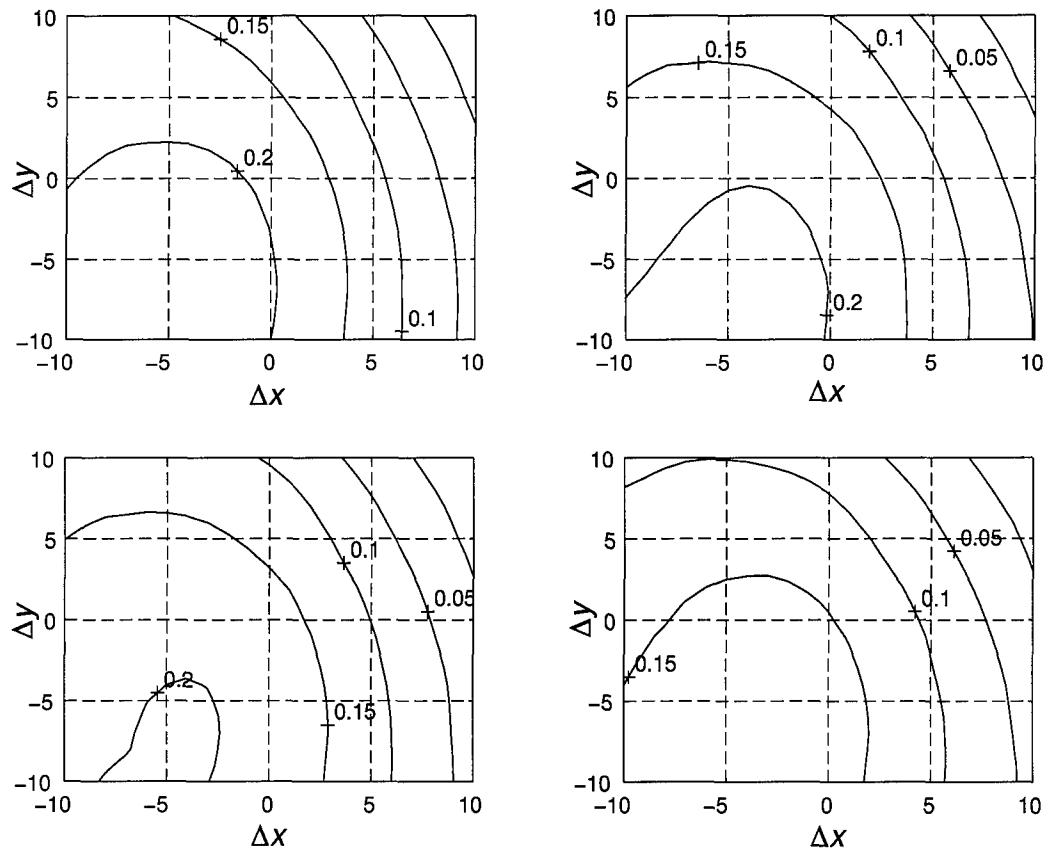


Figure 9. Surface contour of the autocorrelation function for four representative anchor points from the sample grid. Contours are in units of waves<sup>2</sup>. Each unit of  $\Delta x$  and  $\Delta y$  is 95  $\mu\text{m}$  and 105  $\mu\text{m}$ , respectively.

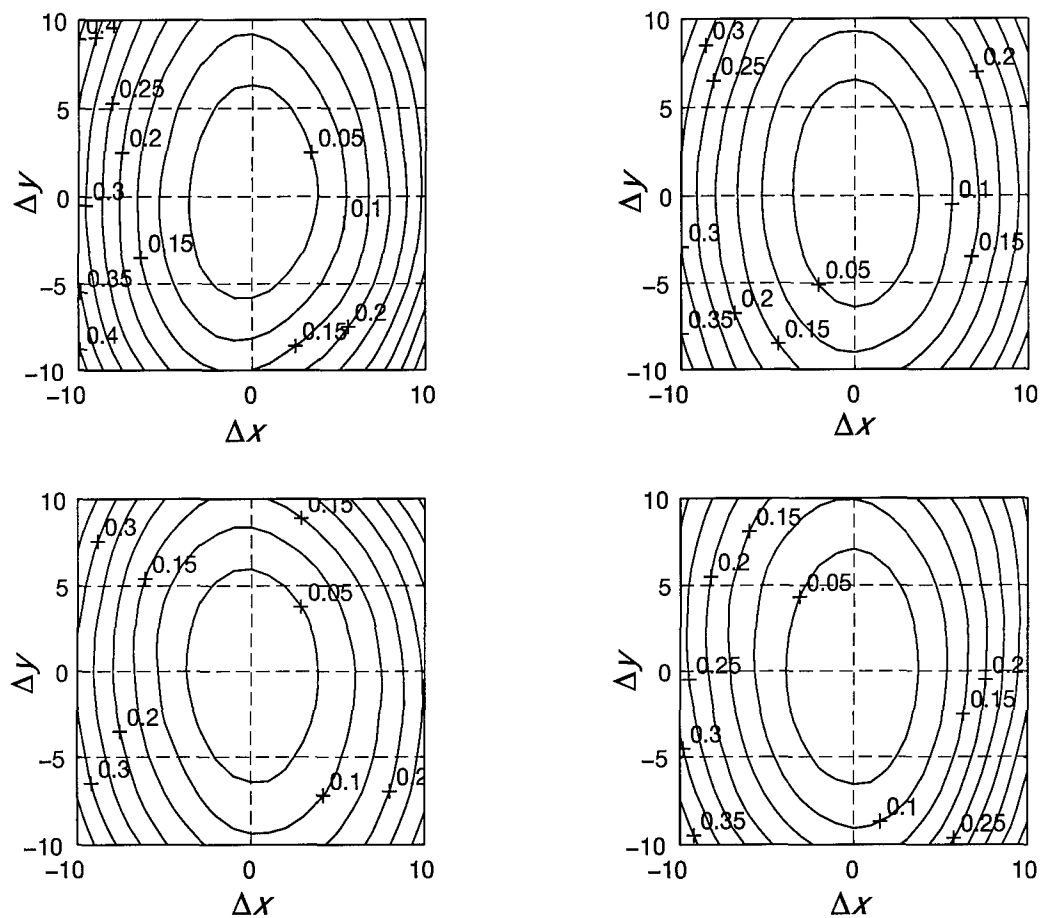


Figure 10. Surface contour of the structure function for four representative anchor points from the sample grid. Contours are in units of  $\text{waves}^2$ . Each unit of  $\Delta x$  and  $\Delta y$  is  $95 \mu\text{m}$  and  $105 \mu\text{m}$ , respectively.

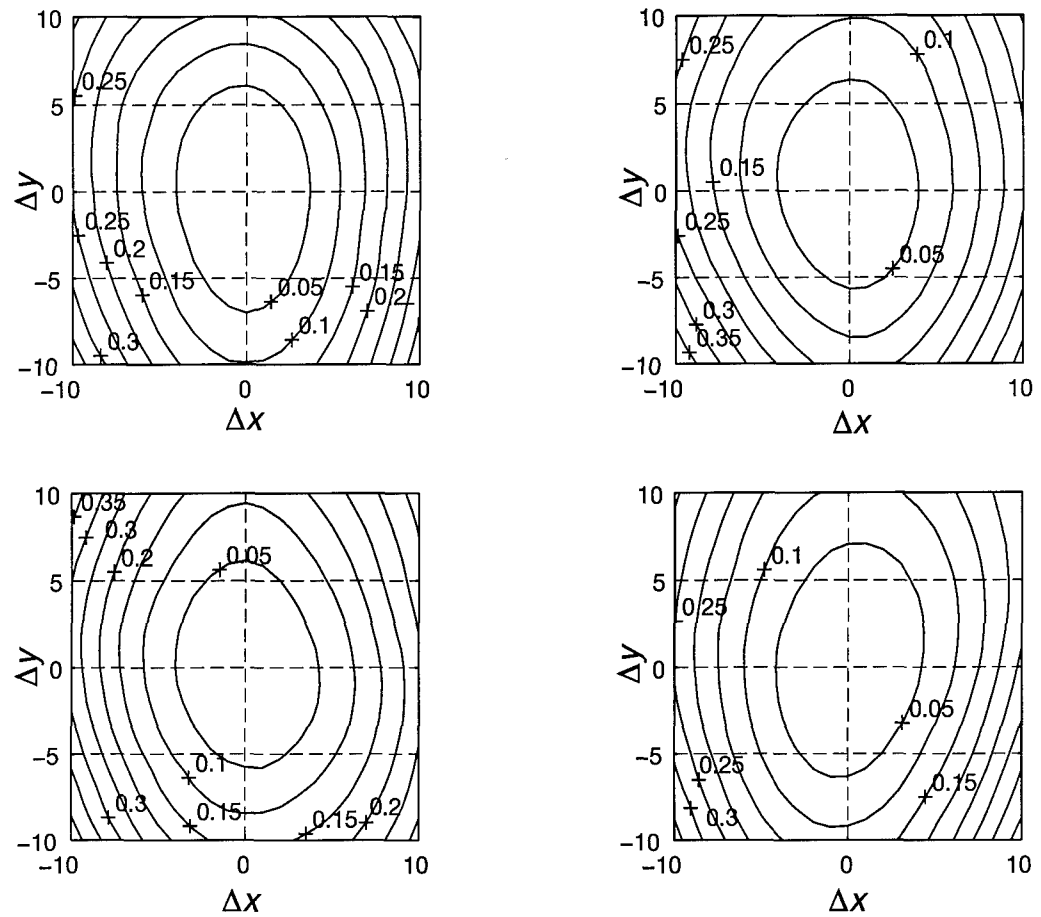


Figure 11. Surface contour of the structure function for four representative anchor points from the sample grid. Contours are in units of  $\text{waves}^2$ . Each unit of  $\Delta x$  and  $\Delta y$  is  $95 \mu\text{m}$  and  $105 \mu\text{m}$ , respectively.

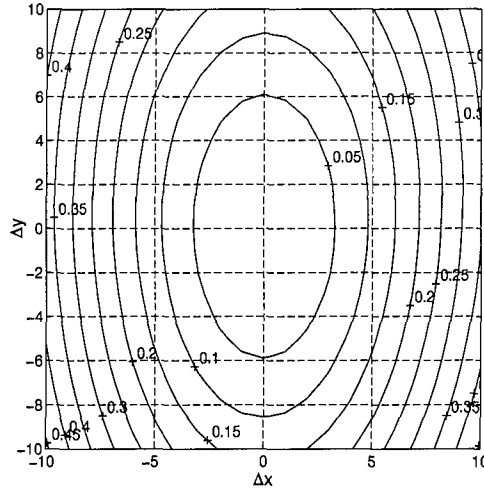
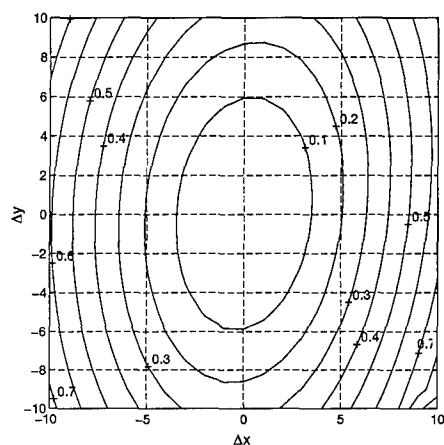


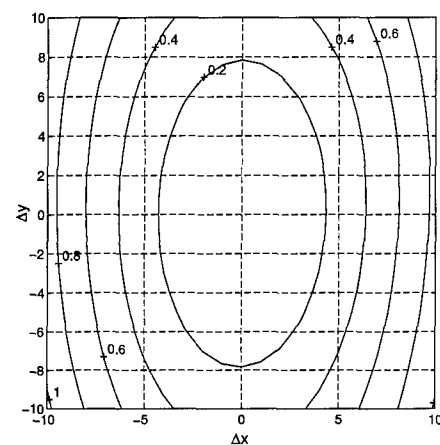
Figure 12. Average structure function surface contour for 59 anchor points. Aperture is centered at 5.75 cm in the flow. Contours are in units of waves<sup>2</sup>. Each unit of  $\Delta x$  and  $\Delta y$  is 95  $\mu\text{m}$  and 105  $\mu\text{m}$ , respectively.

images. This region might be better modeled as a quasi-deterministic phenomena [2, 18]. The results which follow pertain to the center 59 anchor points which exhibited stationarity in first increments.

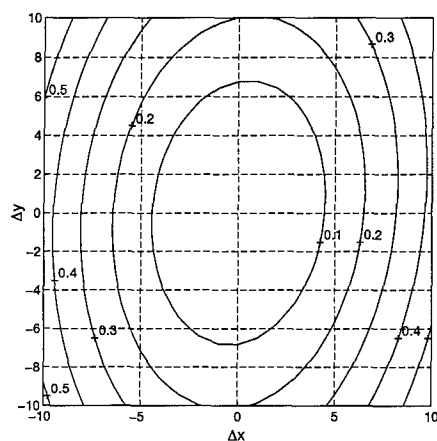
When the fluctuating phase is stationary in first increments, the phase structure function given by Eq. (38) reduces to the two-dimensional function  $\tilde{D}_\phi(\Delta x, \Delta y)$ , which is representative of any point in the aperture. From the center 59 anchor points, an average structure function was computed, and is shown as a surface contour in Fig. 12. Recall this average structure function represents one beam location in the flow, centered at 5.25 cm from the exit of the turbulence generator. Similar structure function results were obtained for the other aperture locations in the flow. Fig. 13 shows average structure functions for four other downstream locations. Note that each average structure function exhibits similar elliptical contours, differing only in scaling as a function of the downstream location in the flow. The next section develops a technique to model these elliptical contours.



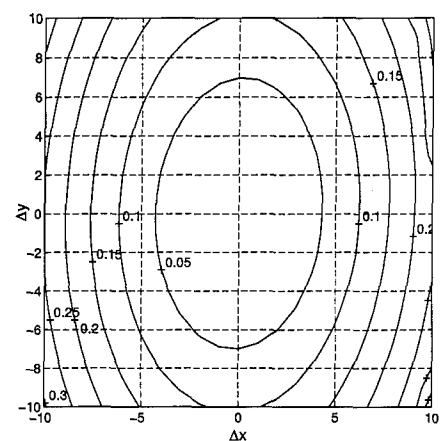
(a)



(b)



(c)



(d)

Figure 13. Average structure function surface contours for 59 anchor points at four aperture locations in the turbulent mixing layer. Contours are in units of waves<sup>2</sup>. Each unit of  $\Delta x$  and  $\Delta y$  is  $95 \mu\text{m}$  and  $105 \mu\text{m}$ , respectively. Aperture is centered at: (a) 8.25 cm; (b) 10.75 cm; (c) 18.75 cm; and (d) 28.75 cm from the exit of the turbulence generator.



### 3.4 Structure-Function-Based Modeling of Free Turbulence

In this section the local homogeneity observed at all six aperture locations is used to develop a model analogous to the Kolmogorov model for atmospheric turbulence, described in Chapter II. For clarity, this development is initially limited to a single location in the turbulent flow, where the effective aperture is centered at 5.75 cm, and the average structure function is represented in Fig. 12. Note this structure function does not exhibit circular symmetry about  $\hat{D}_\phi(0, 0)$ , a requirement for statistical isotropy. Hence, an attempt to model the structure function using the scalar  $r^{5/3}$  power law given by Eq. (17) is not appropriate. However, in an analogous manner, consider orthogonal slices,  $\tilde{D}_\phi(\Delta x, 0)$  and  $\tilde{D}_\phi(0, \Delta y)$  fitted to  $\alpha_x |\Delta x|^{5/3}$  and  $\alpha_y |\Delta y|^{5/3}$  functions, respectively. Fig. 14 is the result of this power law fit resulting in  $\alpha_x = 0.0078$  and  $\alpha_y = 0.0027$ . The phase structure functions are in units of waves<sup>2</sup>, while the  $\Delta x$  and  $\Delta y$  units are samples; hence the coefficients,  $\alpha_x$  and  $\alpha_y$ , have units of waves<sup>2</sup> samples<sup>-5/3</sup>. Equivalently, the alpha coefficients may be expressed in units of rad<sup>2</sup>  $\mu\text{m}^{-5/3}$  by the conversion factor,  $(2\pi)^2(\text{sample spacing})^{-5/3}$ , where the sample spacing is 95  $\mu\text{m}$  and 105  $\mu\text{m}$  in  $x$  and  $y$ , respectively. Similar functional fits were applied to the other five locations. Fig. 15 is a plot of the coefficients  $\alpha_x$  and  $\alpha_y$  as a function of all six beam locations in the flow. Note the coefficients peak at the same location in the flow, 10.75 cm, for both the streamwise and cross-stream indices. Also, the streamwise coefficient is 2–3 times greater than the cross-stream coefficient, consistent with the typical scale sizes reported by Sutton [47].

An equivalent expression for the phase structure function given in Eq. (17) was introduced by Fried [6] as

$$D_\phi(r) = 6.88 \left( \frac{r}{r_0} \right)^{5/3}, \quad (39)$$

where the parameter,  $r_0$ , is referred to as the atmospheric coherence diameter [13]. Analogously, for the turbulent mixing layers, consider two coherence dimensions,  $x_0$  and  $y_0$ , such

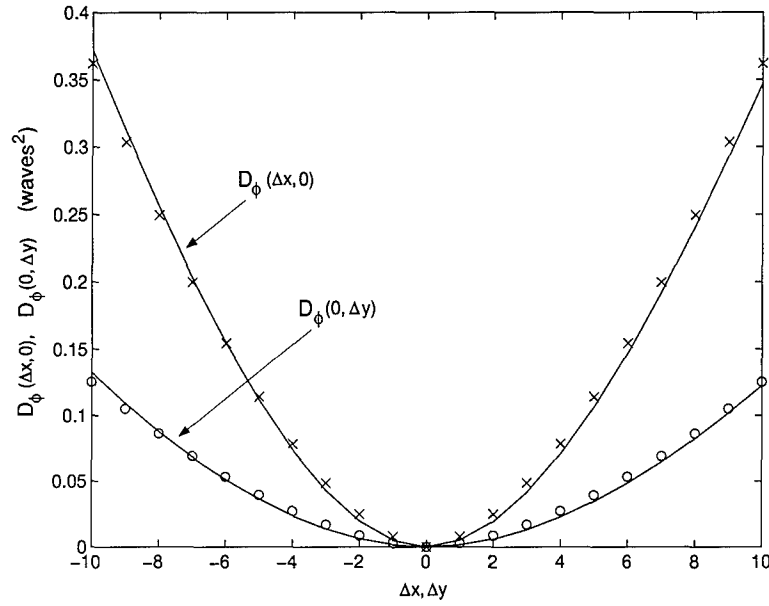


Figure 14. Orthogonal slices of  $\tilde{D}_\phi(\Delta x, \Delta y)$ . Upper curve:  $\tilde{D}_\phi(\Delta x, 0)$ , overlayed ('x') with  $\alpha_x |\Delta x|^{5/3}$  for  $\alpha_x = 0.0078 \text{ waves}^2 \text{ samples}^{-5/3}$ . Lower curve:  $\tilde{D}_\phi(0, \Delta y)$ , overlayed ('o') with  $\alpha_y |\Delta y|^{5/3}$  for  $\alpha_y = 0.0027 \text{ waves}^2 \text{ samples}^{-5/3}$ .

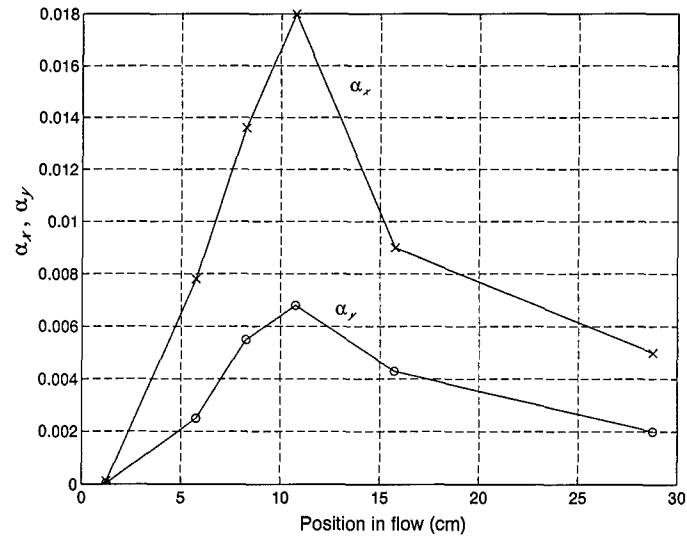


Figure 15. Plot of the coefficients  $\alpha_x$  and  $\alpha_y$  as a function of the six locations in the flow. Units are  $\text{waves}^2 \text{ samples}^{-5/3}$ .

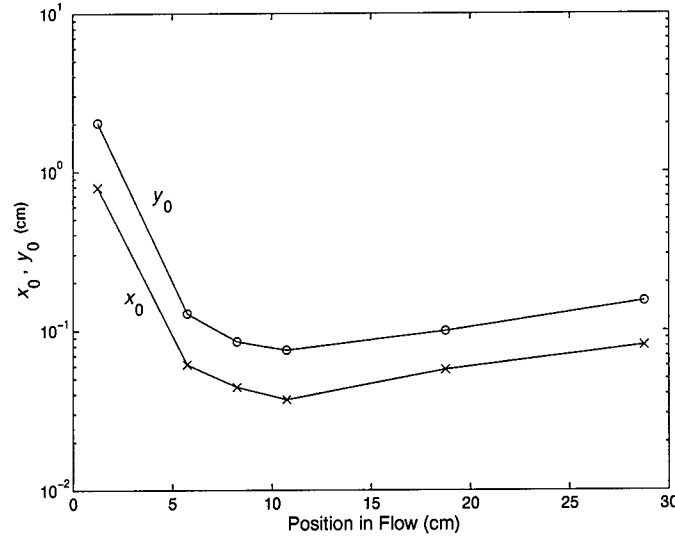


Figure 16. Coherence parameters,  $x_0$  and  $y_0$  as a function of downstream location. The vertical axis is  $\log_{10}$  scale.

that the orthogonal slices of  $\tilde{D}_\phi(\Delta x, \Delta y)$  may be represented by

$$\tilde{D}_\phi(\Delta x, 0) = 6.88 \left( \frac{|\Delta x|}{x_0} \right)^{5/3} \quad \text{and} \quad \tilde{D}_\phi(0, \Delta y) = 6.88 \left( \frac{|\Delta y|}{y_0} \right)^{5/3}, \quad (40)$$

where

$$x_0 = \left( \frac{\alpha_x}{6.88} \right)^{-3/5} \quad \text{and} \quad y_0 = \left( \frac{\alpha_y}{6.88} \right)^{-3/5}, \quad (41)$$

which have units of samples waves $^{-6/5}$ .

The parameters  $x_0$  and  $y_0$  were computed for the six aperture locations in the flow and are shown in Fig. 16, where the result from Eq. (41) has been scaled by sample spacing and  $(2\pi)^{-6/5}$  to obtain units of centimeters. For an appreciation of the downstream anisotropy, the vertical axis of Fig. 16 is on a  $\log_{10}$  scale. Hence, the values for  $x_0$  and  $y_0$  range from approximately 2 cm to less than 0.4 mm. For comparison, an average value for the atmospheric parameter,  $r_0$ , for a good mountain-top observatory [13] is about 10 cm. Lower values of  $r_0$  indicate poorer seeing conditions. While the average structure functions are not circularly symmetric, they are approximately symmetric about the  $\Delta x$  and  $\Delta y$  axes. Therefore, in terms

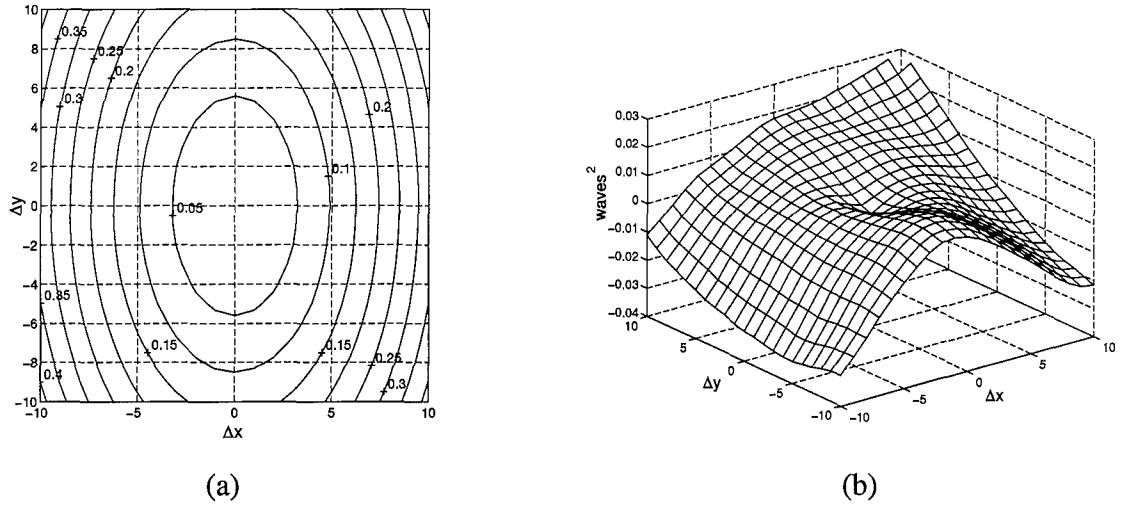


Figure 17. Structure function surface approximation using the coherence dimensions,  $x_0$  and  $y_0$ , for the aperture centered at 5.75 cm. Each unit of  $\Delta x$  and  $\Delta y$  is  $95 \mu\text{m}$  and  $105 \mu\text{m}$ , respectively. (a) Surface contour, in units of  $\text{waves}^2$ ; (b) Difference between actual and approximation.

of the coherence dimensions, the structure functions may be approximated by

$$\tilde{D}_\phi(\Delta x, \Delta y) \approx 6.88 \left\{ \left( \frac{\Delta x}{x_0} \right)^2 + \left( \frac{\Delta y}{y_0} \right)^2 \right\}^{5/6}. \quad (42)$$

A surface contour of Eq. (42) is shown in Fig. 17 for the aperture centered at 5.75 cm, which may be compared with the experimental structure function shown in Fig. 12. Included in Fig. 17 is a surface displaying the difference between the experimental and approximated structure function. The maximum difference between the two surfaces is approximately  $0.03 \text{ waves}^2$  at  $(\Delta x, \Delta y) = (-10, -10)$ , which is suggestive of the limited separation for which the Kolmogorov-like model may be valid in this flow.

### 3.5 Strehl Ratio and Reynolds Number Effects

The PSF and SR were computed for an imaging aperture equal to the beam size using Eq. (18) and Eq. (19). The SR is relative because the diffraction-limited PSF in the

denominator of Eq. (19) was replaced with the PSF of the imaging system in the absence of turbulence, a measurable quantity. This relative metric of image quality is similar to techniques used previously [7, 50], and is consistent with direct measurements reported in Chapter IV. Throughout this chapter, reference to SR implies a relative measure, unless noted otherwise. The structure function,  $D_\phi$ , was taken to be the average structure functions,  $\tilde{D}_\phi(\Delta x, \Delta y)$  for each location in the flow, and determined from the experimental structure function parameters using Eq. (42).

A plot of the SR is shown in Fig. 18, accompanied by two other SR calculations: the SR using Eq. (21), where  $\sigma_\phi^2$  was computed from the center of the measured phase surfaces, which is also a relative measure; and the theoretical SR using Eq. (22), an approximation of Eq. (21) which assumes wide-sense stationarity. The vertical axis of Fig. 18 is on a  $\log_{10}$  scale to highlight the significant differences in the three predictions. First, the SR computed from the structure functions follows a curve similar to the coherence parameters,  $x_0$  and  $y_0$ , predicting a minimum SR of approximately 0.02. Both the structure function and phase variance calculations indicate a minimum in the region of 10.75 cm, where the coefficients  $\alpha_x$  and  $\alpha_y$  peak. However, the SR computed from the on-axis phase variance overestimates the optical degradation by nearly three orders of magnitude compared to the estimate obtained using the structure functions. Note that 28.75 cm downstream, where significant diffusion of the free mixing layers into the ambient air has occurred, these two predictions are nearly equal. The theoretical SR given by Eq. (22) is a poor model for two reasons: first, the random phase fluctuations for this flow are not wide-sense stationary; and second, Eq. (22) predicts continued degradation with growth of the mixing layer width, not accounting for lateral diffusion.

The mixing layers may be characterized as being in a pre-transition, transition, or post-transition state [55]. In the pre-transition state, the flow may be turbulent, but minimal mixing of the two fluids has occurred. Mixing transition is characterized by a large increase in the mixed fluid fraction, and is associated with a rapid decrease in the SR [3]. The transition state has been reported [5] to occur for a local Reynolds number, as defined by Eq. (32), of  $Re_\delta > 10^4$ . Thus, referring to Table 1, the mixing transition for the present experiments occurs

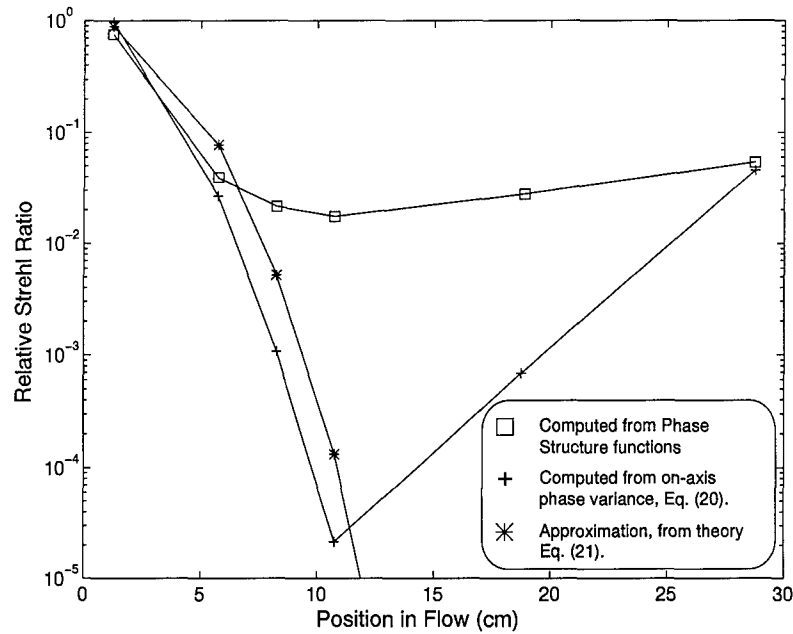


Figure 18. Relative Strehl ratio as a function of downstream location. The vertical axis is  $\log_{10}$  scale.

in the range of 2.4 cm, 5.5 cm, and 28.4 cm for the air/He,  $N_2$ /He, and  $N_2$ /air mixing layers, respectively. The effects of transition for the air/He and  $N_2$ /He mixing layers may be seen in Fig. 18, where the structure-function-based SR drops by approximately 95% between 1.25 and 5.75 cm. The SR continues to decrease downstream to 10.75 cm, then increases, although the mixing transition for the  $N_2$ /air has not yet occurred. We conjecture the improvement in the SR beyond 10.75 cm is a result of the three mixing layers merging. Using Eq. (30), the  $N_2$ /He mixing layer is predicted to reach the width of the turbulence generator exit between 5 and 10 cm downstream for the range of  $C_\delta$  given in Eq. (31). By this point, the three mixing layers have merged, and a leveling of the SR should be observed [3]. The coefficients,  $\alpha_x$  and  $\alpha_y$ , and the SR indicate a maximum turbulence effect in the region of 10.75 cm, suggesting the region where the mixing layers have merged. Consequently, we may conclude that the coefficient,  $C_\delta$ , is near the lower bound of Eq. (31) for these experiments. The increase in SR beyond 10.75 cm is attributed to the continued diffusion of the unbounded mixing layers

into the ambient air. The mixing transition for the  $N_2$ /air mixing layer is predicted to occur in the downstream region of 28 cm. With a density ratio of approximately one and a velocity difference of 1.5 m/sec, this mixing layer has negligible effect on the SR.

### 3.6 *Summary of Free Turbulent Mixing Layers*

The shearing interferometer, a well-established flow visualization tool, was used to generate a statistical ensemble of optical phase fluctuations due to propagation through high-Reynolds-number mixing layers. An unbounded mix of Helium gas at 8.5 m/sec and Nitrogen gas at 1.5 m/sec in ambient air induced optical phase perturbations. An ensemble of wave front phase measurements was obtained for six aperture locations in the flow. The autocorrelation function and the phase structure function were computed for each ensemble. For each location in the turbulent flow, the autocorrelation function indicated the random phase fluctuations were not wide-sense stationary; thus, application of the previously described aero-optical model is not appropriate. The structure function results indicated the random phase fluctuations were stationary in first increments, though not isotropic. Hence, a direct application of a Kolmogorov five-thirds power law was not appropriate. However, an analogous five-thirds power law was developed for the streamwise and cross-stream indices separately. One-dimensional coherence parameters were introduced, analogous to the atmospheric coherence diameter,  $r_0$ , for Kolmogorov turbulence. The parameters provide a measure of the anisotropy in the flow. Strehl ratios, computed from the phase structure functions, were reported and compared with two aero-optical estimations based on on-axis phase variance and mixing layer width. The aero-optical models overestimate the optical degradation by orders of magnitude compared to the structure functions. These results suggest the potential for developing novel prediction models for complex flows such as free turbulent mixing layers.

## *IV. TURBULENT MIXING LAYERS IN CHANNEL FLOW*

### *4.1 Overview*

In this chapter the shearing interferometer wave front sensor is used to obtain slope measurements of perturbed wave fronts after propagating through a turbulent mixing layer within a rectangular channel. The dynamics of turbulence in channels differ significantly from free turbulence. The presence of the solid boundaries results in the generation of boundary layers, characterized by a flow velocity of zero at the channel wall and a large velocity gradient within close proximity. For high Reynolds numbers, the frictional forces due to viscous effects near the wall are significant. As the flow develops, the boundary layer thickness grows, thus affecting the flow properties throughout the channel [30, 45]. Experimental investigations of the optical effects of mixing layers in channel flow is more prevalent in the literature than for free mixing layers. These investigations, however, have been limited to thin beam techniques or averaged Strehl ratios [3, 4, 21, 55]; hence, data on the anisotropic properties of the flows have not been available.

For this portion of the research, the turbulence generator was used to mix Helium and Nitrogen gas at a sharp trailing edge, forming a bounded mixing layer with a density ratio of approximately seven. The slope measurements were used to reconstruct wave front phase surfaces. Again, the intent was to capture the random index-of-refraction fluctuations by means of phase reconstructions over a sufficiently large set of measured data. Autocorrelation functions and phase structure functions were computed to assess the statistical stationarity of the phase fluctuations. The previous chapter described similar measurements for free turbulent mixing. In that chapter, the random phase fluctuations were not wide-sense stationary; hence, application of classical aero-optical models assuming isotropy was not appropriate. However, calculation of phase structure functions indicated stationarity in first increments, resulting in a structure-function-based model of the average optical transfer function and Strehl ratio. In the present chapter, the phase fluctuations are evaluated in a similar manner for a single mixing layer of Helium and Nitrogen in a channel flow. Additionally, for each slope measurement, the



corresponding point spread function was recorded. The point spread function is a measurement capability that was added after the free turbulence experiments. The averaged set of point spread functions provided an independent and direct measurement of a Strehl ratio. Finally, two additional estimates of the Strehl ratio are presented. One is computed from the on-axis variance of the reconstructed phase surfaces, and the other is computed from an empirical formula using an estimate of the growth of the mixing layer width. The latter two estimates assume an isotropic flow. These two models are shown to be accurate only for low Reynolds numbers in the mixing layer, whereas, the Strehl ratios computed from the structure functions are shown to be accurate throughout the flow.

The chapter begins with a description of the experimental setup used to generate and compute an ensemble of phase reconstructions of aberrated light waves. Next, a set of statistical calculations is performed on the phase surfaces and the results are assessed for statistical homogeneity and isotropy. Then, a set of modeling parameters is computed, based on the structure functions, leading to Strehl ratio predictions. Finally, the Strehl ratio is related to the Reynolds number in the flow.

## 4.2 *Experimental Setup*

The optical bench used for the experiments is shown in Fig. 19. A 2 cm diameter, collimated laser beam was transmitted through the turbulent flow at various distances from the exit of the turbulence generator. The edge of the turbulent flow was imaged onto the entrance pupil of the wave front sensor. The lens pair, Lens 1 and Lens 2, provides a magnification of 0.5 so that a 1 cm diameter image of the perturbed beam was presented at the pupil plane of a lateral shearing interferometer. The image filled approximately 50% of the pixels in a  $512 \times 484$  detector array. This resulted in a single pixel subtending a region of approximately  $47 \mu\text{m} \times 54 \mu\text{m}$  in the plane of the turbulence. Additionally, the 1 cm image was split at the non-polarizing beam splitter, providing a path to the point spread function (PSF) camera. The collimated beam was focused by lens 5, having a focal length of 1000 mm, on the PSF camera. This camera was synchronized with the wave front sensor cameras, providing simultaneous

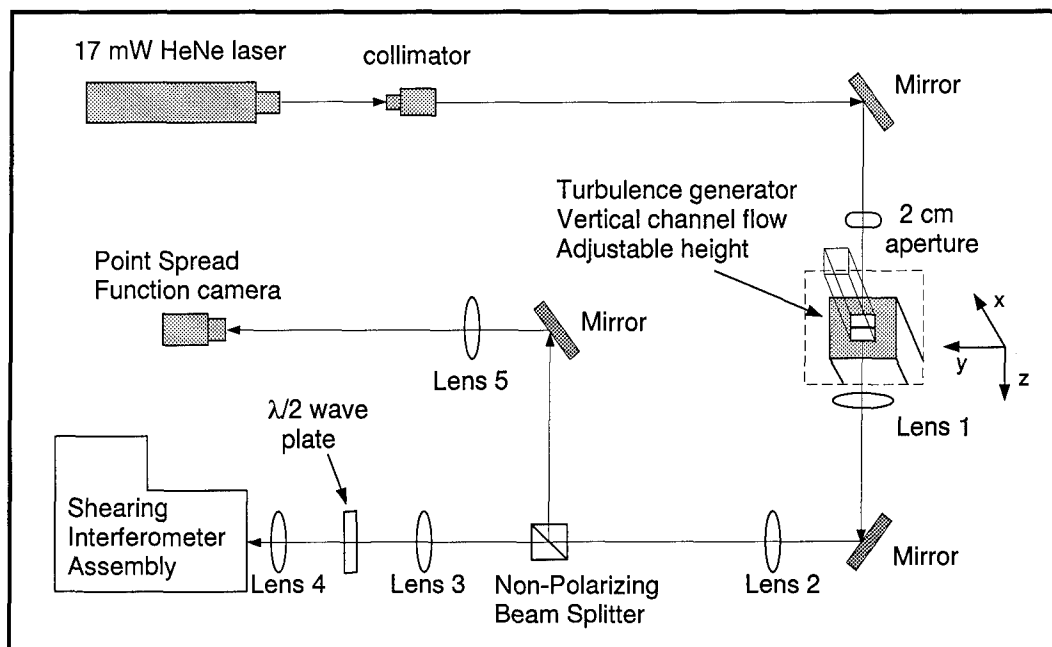


Figure 19. Optical bench used to obtain phase measurements and point spread functions for a laser beam propagating through the turbulent mixing layer.

measurements in the mixing layer. The flow field orientation with respect to the laser beam was the same as for the free mixing layers described in Chapter III. Here, the flow is confined within a rectangular channel. The channel cross-section is matched to the exit nozzle of the turbulence generator to inhibit the creation of an additional boundary layer at the generator-channel interface. The two transmitting sides of the channel are composed of  $2.54 \text{ cm} \times 50 \text{ cm}$  flats of glass, having an optical quality of  $1/3$  wave at  $632.8 \text{ nm}$ . The glass is a water white material and is anti-reflective coated. The continuous-window channel was chosen to permit a vertical translation of the generator-channel assembly, so that any location in the flow could be analyzed. The optical phase perturbations and PSF were measured at eight locations in the flow. The locations were centered on  $1.25 \text{ cm}$ ,  $2.25 \text{ cm}$ ,  $3.75 \text{ cm}$ ,  $5.75 \text{ cm}$ ,  $8.25 \text{ cm}$ ,  $10.75 \text{ cm}$ ,  $13.25 \text{ cm}$ , and  $15.75 \text{ cm}$  downstream of the exit of the turbulence generator. These locations can be equivalently expressed in terms of a dimensionless  $X/D$  parameter, where  $X$  is the location of the beam in the flow, and  $D$  is the length of one side of the exit nozzle. Thus, for

the present experiment, the  $X/D$  locations are approximately 0.5, 0.9, 1.5, 2.3, 3.3, 4.3, 5.3, and 6.3.

The relevant channel flow parameters may be obtained directly from Table 1 in Chapter III for the He/N<sub>2</sub> mixing layer. Hence, the Reynolds number per centimeter,  $Re_x/x$ , for the He/N<sub>2</sub> mixing layer is 4444 cm<sup>-1</sup>. For an average  $C_\delta$  of 0.37, the width per centimeter,  $\delta(x)/x$ , of the He/N<sub>2</sub> mixing layer is approximately 0.4, which results in a  $Re_\delta/x$  of 1822 cm<sup>-1</sup>.

An example of a reconstructed phase surface is shown in Fig. 20, where the deterministic effects have been subtracted. Fig. 20 is one realization for the aperture centered at 8.25 cm in the flow, and is representative of the average dynamic range observed at that location. Note that the  $x$  and  $y$  axis units in Fig. 20 are samples. The sample spacing in the  $x$ -direction (streamwise) is approximately 95  $\mu$ m, and the sample spacing in the  $y$ -direction (cross-stream) is approximately 105  $\mu$ m. An ensemble of these phase surfaces was used as a means to characterize the random fluctuations in the turbulent flow. Section 4.3 describes the statistical calculations performed.

The PSF camera was used to generate an ensemble of PSF measurements to be used to calculate the average SR. The SR is relative because the diffraction-limited PSF in the denominator of Eq. (19) was replaced with the PSF of the imaging system in the absence of turbulence, a measurable quantity. Replacing the formal Strehl definition with a relative measure of image degradation is not unusual in analysis of optical systems [7, 50]. Furthermore, this relative measure allows direct comparison with the phase-variance-based model, which is also relative, as was discussed in Chapter II. The topic of relative SR is discussed in more detail in Section 4.5.

For each aperture location in the flow, a PSF was initially recorded with the turbulence generator off. This measurement was used as a reference for computing the SR given by Eq. (19). An example of a reference PSF, for the aperture centered at 8.25 cm, is shown in Fig. 21(a). The central maximum, recognized as the Airy disk in the diffraction-limited case, has a 256 gray-scale intensity of approximately 100. Dark frame and flat field calibrations have

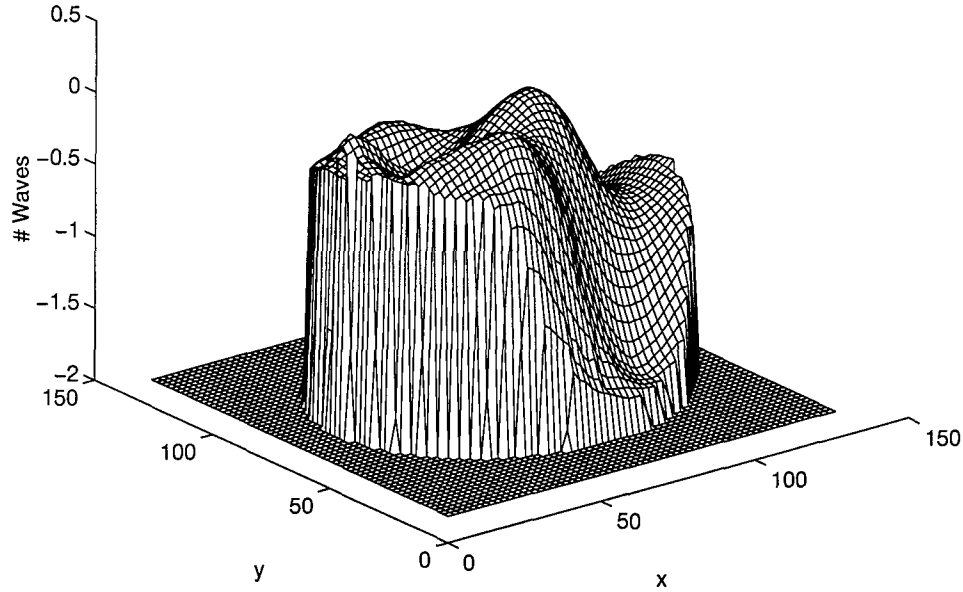
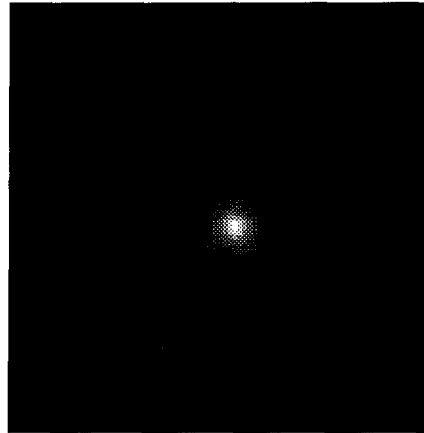
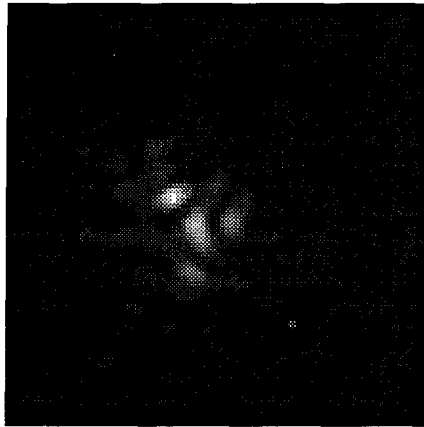


Figure 20. Reconstructed wavefront phase. Deterministic optical system effects have been removed. Flow is in +x direction, propagation is in +z direction. Sample spacing in  $x$  is  $95 \mu\text{m}$ ; sample spacing in  $y$  is  $105 \mu\text{m}$ .

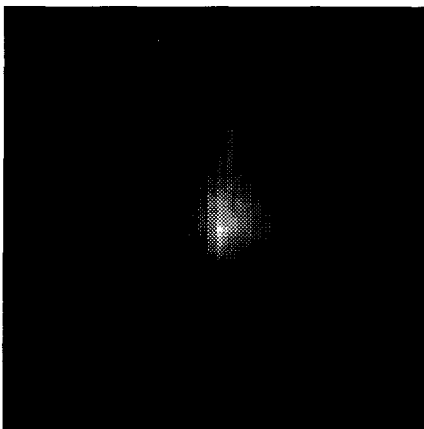
been performed [42]. Fig. 21(b) shows an example of a single realization of the PSF for the He/N<sub>2</sub> mixing layer at the same aperture location. The horizontal and vertical scale represents angular frequency of the perturbed wavefront in the streamwise and cross-stream directions, respectively. This realization corresponds to the reconstructed phase surface depicted in Fig. 20 and clearly exhibits the optical effects induced by the turbulent mixing. An image of the average PSF, taken over 160 realizations, is shown in Fig. 21(c). The average optical effects are characterized by blurring about a central maximum. The central maximum for this example has a 256 gray-scale intensity of approximately 18. Thus, using Eq. (19), the relative SR is about 0.18. PSF reference measurements and averages were obtained similarly for the other seven beam locations, and the corresponding SR was computed. The results are presented later in this chapter.



(a)



(b)



(c)

Figure 21. PSF images for the turbulent mixing layer experiments. Aperture is centered at 8.25 cm: (a) Reference PSF (no turbulence); (b) Single realization; (c) Average PSF taken over 160 independent realizations.

### 4.3 Statistical Calculations

In this section the results of the ACF and the structure function calculations are presented. First, a discussion of the general technique used for the statistical calculations is provided. The procedure is nearly identical to that performed for the free turbulence. Only the variations are presented here.

First, the random fluctuating phase,  $\phi'(x, y)$  is obtained. Again, the reconstructed phase surfaces are  $128 \times 128$  arrays. To reduce computational complexity and allow the assumptions of homogeneity and isotropy to be tested, a set of 81 anchor points was defined on the aperture, similar to the free turbulence calculations. This time, however, the anchor points were located more compactly towards the center region of the aperture since the edge anchor points were not useful for the free turbulence measurements. Fig. 22 shows an example of one phase realization,  $\phi'(x, y)$ , displayed as a surface contour with an overlay of the 81 anchor points, where the  $x$  and  $y$  spacing between each anchor point is five samples. This grid of anchor points was used for the ACF and structure function calculations for all channel turbulence measurements. All statistical calculations were based on an ensemble size of 160 realizations, based on the sample-based SNR given in Eq. (34). For 160 realizations, the SNR is approximately 10 for both the ACF and the structure function, when the respective estimates are substituted as the sample mean in Eq. (34).

*4.3.1 Autocorrelation Function.* The discussion is initially limited to a single location in the turbulent flow, where the aperture is centered at 8.25 cm. An estimate of the statistical ACF given by Eq. (2) was obtained using Eq. (37) for  $\Delta x$  and  $\Delta y$  on an interval of  $-10$  samples to  $+10$  samples and an ensemble of 160 realizations of  $\phi'_i(x, y)$ . Figs. 23 and 24 show the ACF surface contours for a sample set of eight anchor points about the center of the aperture. Each contour exhibits a similar ACF; however, as was observed with the free turbulence, these ACF surfaces do not satisfy the second property of the homogeneous ACF listed in Chapter II. A similar result was obtained for the other seven aperture locations in the turbulent flow. The conclusion is that the phase fluctuations induced by the channel

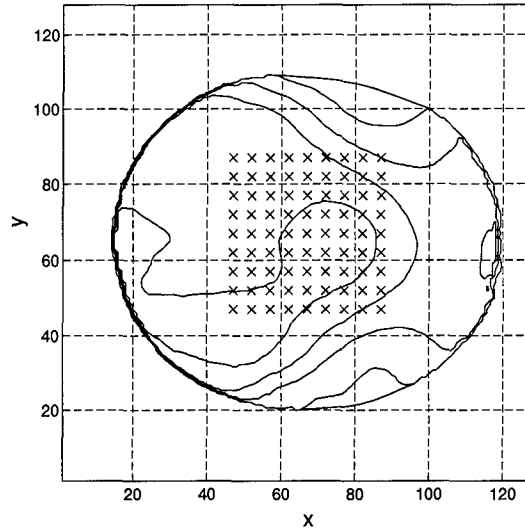


Figure 22. Surface contour of one phase realization,  $\phi'(x, y)$ , with overlay of 81 anchor points. Each 'x' indicates an anchor point. Sample spacing in  $x$  is  $95 \mu\text{m}$ ; sample spacing in  $y$  is  $105 \mu\text{m}$ . Spacing between each anchor point is five samples.

flow mixing layer are not wide-sense stationary, and the traditional aero-optical model is not appropriate. Similar to the free turbulence experiment, the Strehl ratio estimates which are derived from the aero-optical model, as given in Eqs. (21) and (22), were computed and compared to the Strehl ratio obtained from structure function calculations. This time a direct measurement acquired from the average point spread function is also available for comparison. These results appear later in this chapter.

**4.3.2 Structure Function.** Again, the discussion is initially limited to a single location in the turbulent flow, where the aperture is centered at 8.25 cm. An estimate of the statistical phase structure function given by Eq. (14) was obtained using Eq. (38) for  $\Delta x$  and  $\Delta y$  on an interval of  $-10$  samples to  $+10$  samples and an ensemble of 160 realizations of  $\phi'_i(x, y)$ . Figs. 25 and 26 show the structure function for eight representative anchor points located near the center of the aperture. For the random process  $\phi'(x, y)$  to be stationary in first increments, all anchor points must exhibit approximately the same structure function.

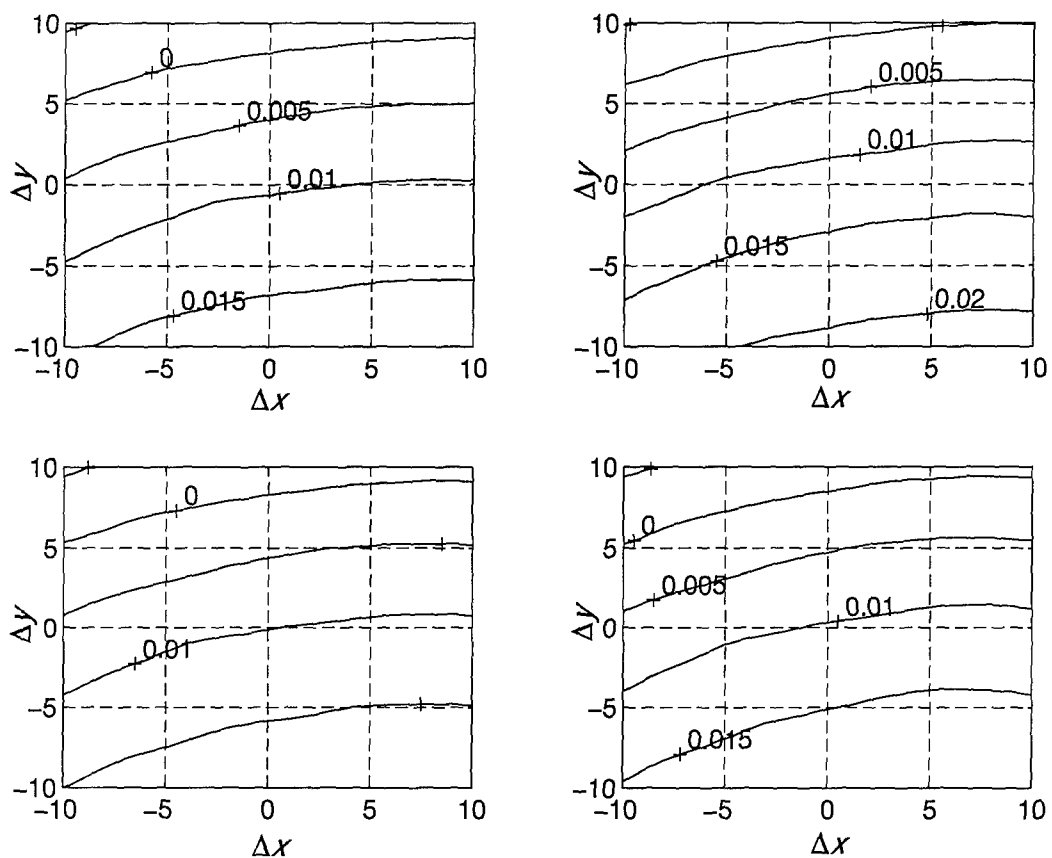


Figure 23. Surface contour of the autocorrelation function for four representative anchor points from the sample grid. Contours are in units of  $\text{waves}^2$ . Each unit of  $\Delta x$  and  $\Delta y$  is  $95 \mu\text{m}$  and  $105 \mu\text{m}$ , respectively.



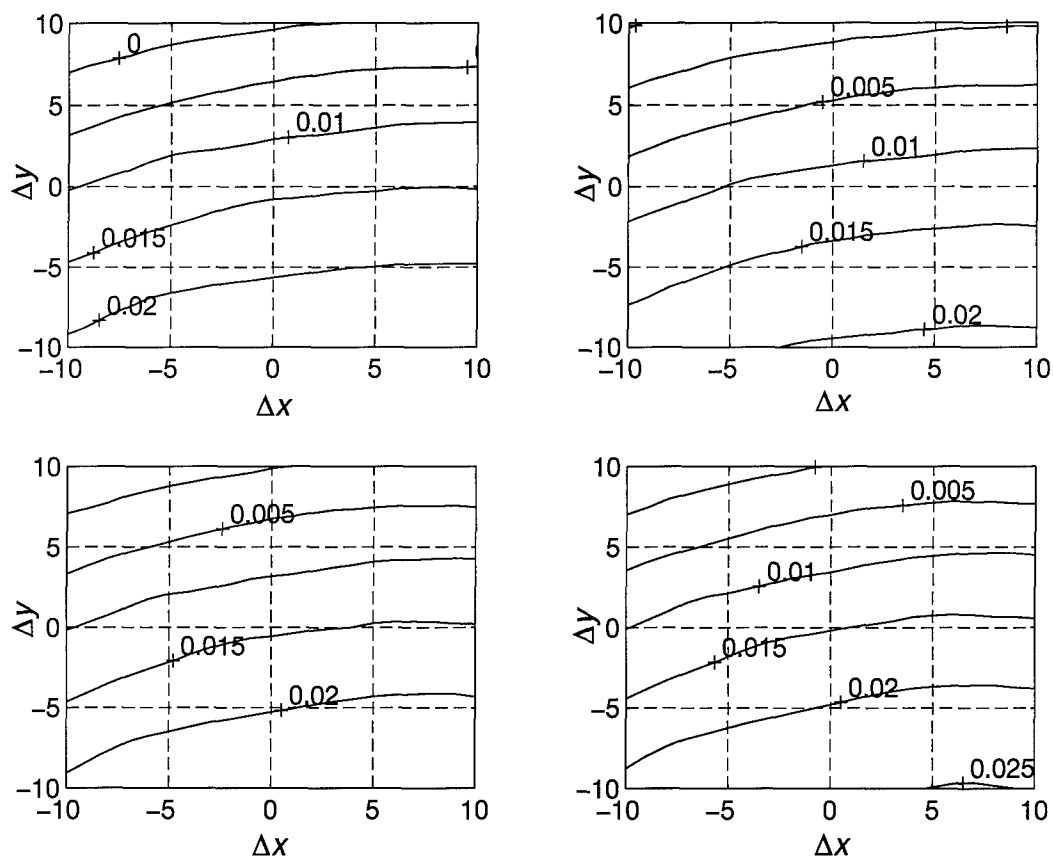


Figure 24. Surface contour of the autocorrelation function for four representative anchor points from the sample grid. Contours are in units of  $\text{waves}^2$ . Each unit of  $\Delta x$  and  $\Delta y$  is  $95 \mu\text{m}$  and  $105 \mu\text{m}$ , respectively.

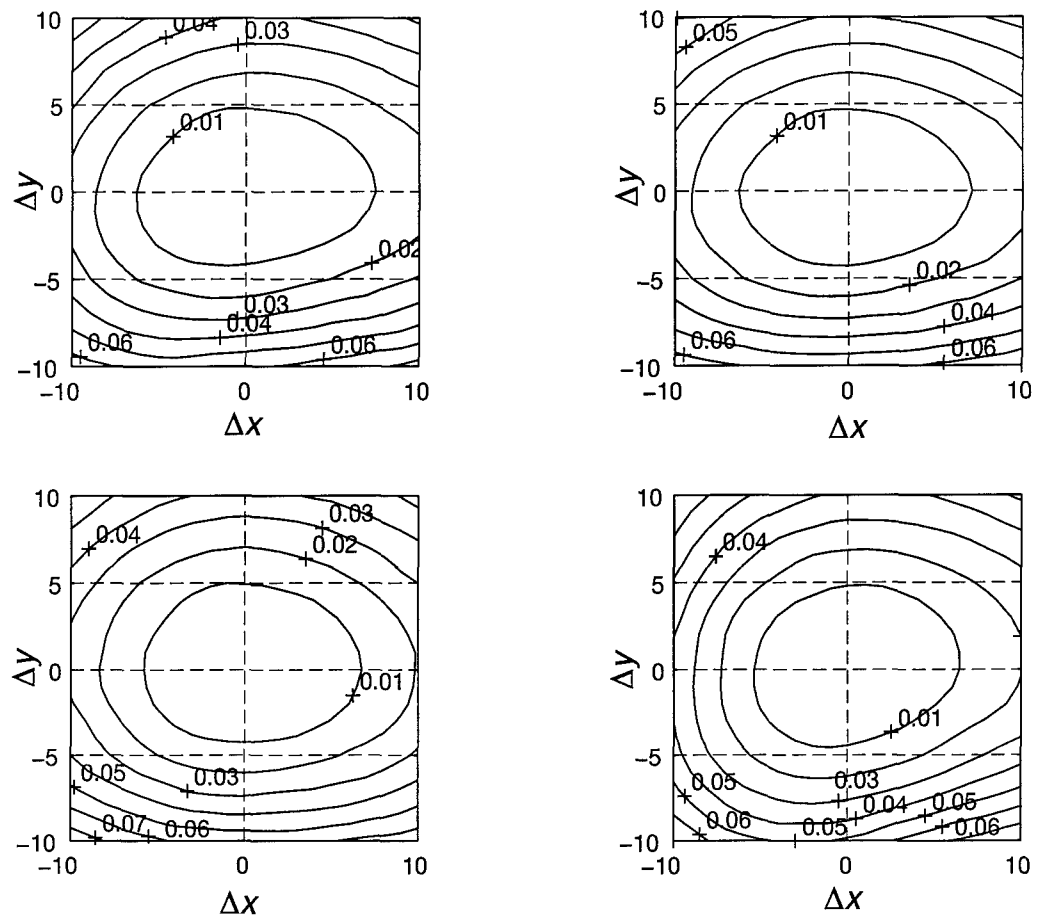


Figure 25. Surface contour of the structure function for four representative anchor points from the sample grid. Contours are in units of  $\text{waves}^2$ . Each unit of  $\Delta x$  and  $\Delta y$  is  $95 \mu\text{m}$  and  $105 \mu\text{m}$ , respectively.

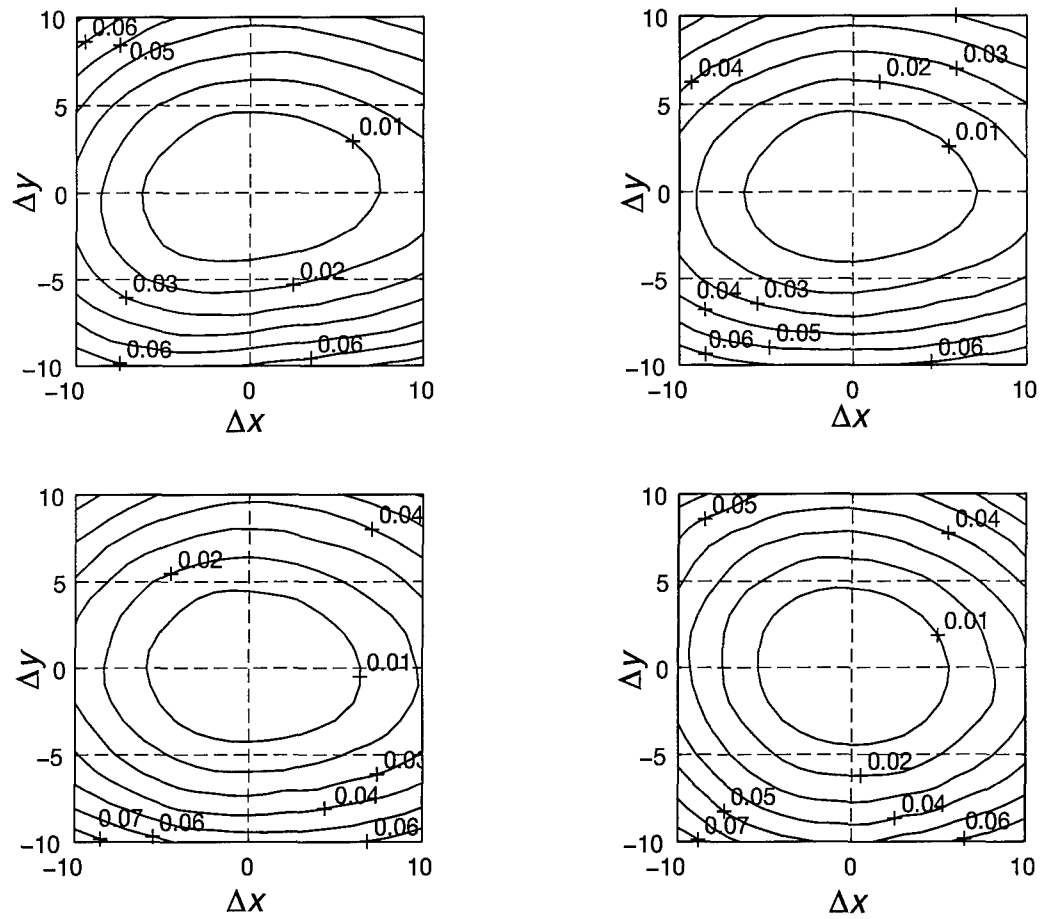


Figure 26. Surface contour of the structure function for four representative anchor points from the sample grid. Contours are in units of  $\text{waves}^2$ . Each unit of  $\Delta x$  and  $\Delta y$  is  $95 \mu\text{m}$  and  $105 \mu\text{m}$ , respectively.

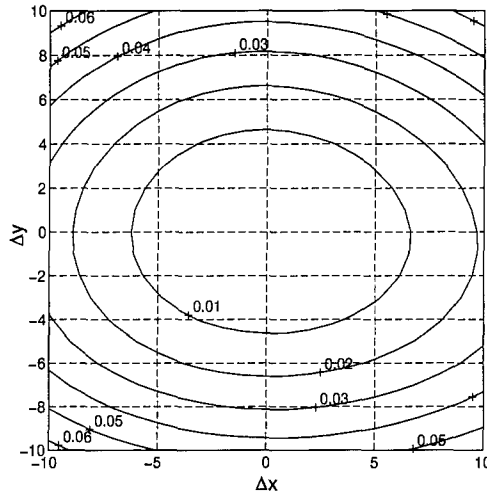
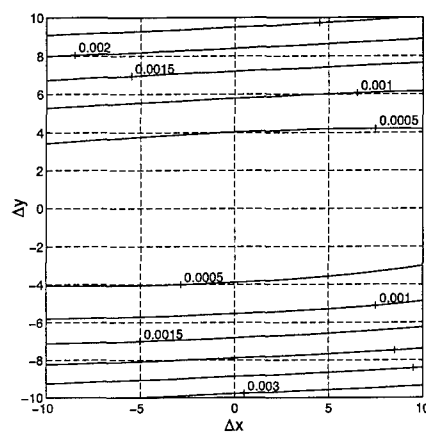
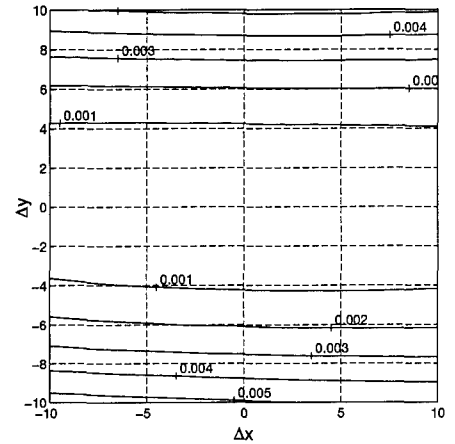


Figure 27. Average structure function surface contour for 81 anchor points. Aperture is centered at 8.25 cm in the flow. Contours are in units of waves<sup>2</sup>. Each unit of  $\Delta x$  and  $\Delta y$  is 95  $\mu\text{m}$  and 105  $\mu\text{m}$ , respectively.

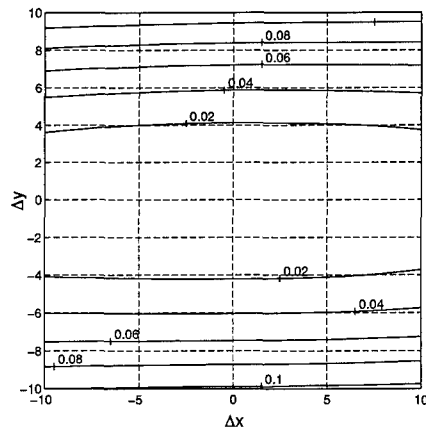
This feature is apparent in the eight-sample set shown in Figs. 25 and 26; i.e., the grid points exhibit similar elliptical contours, symmetric about  $\hat{D}_\phi(0,0)$ . In general, local homogeneity was a good approximation for all 81 anchor points. Hence, an average structure function,  $\tilde{D}_\phi(\Delta x, \Delta y)$ , was computed for the aperture centered at 8.25 cm and is shown as a surface contour in Fig. 27. Similar structure functions were obtained for the other seven aperture locations in the flow. Figures 28 and 29 show average structure functions for the eight flow locations. Note the transition in the elliptical shape of these contours in the region of 8.25 cm to 10.75 cm. In this region the strength of the phase fluctuations in the streamwise direction surpass those in the cross-stream direction. One implication is that there exists a location in this region of the flow which has a circularly symmetric structure function contour, indicative of statistical isotropy. This is a significantly different result from the free turbulence experiments, where the streamwise fluctuations remained at a steady scale factor above the cross-stream fluctuations. The distinction suggests the potential of this technique in characterizing the anisotropy in various types of flow in a non-invasive manner.



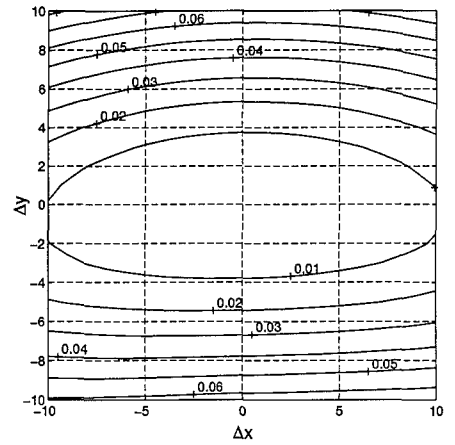
(a)



(b)

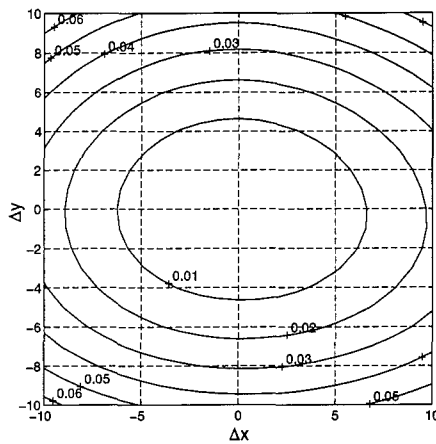


(c)

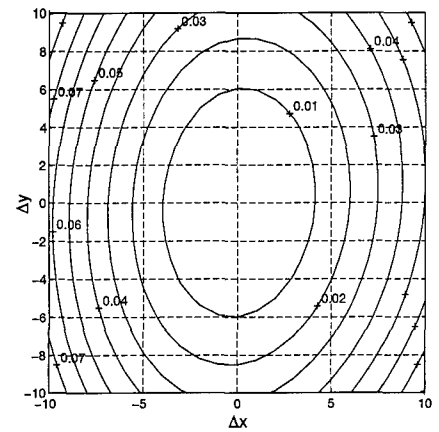


(d)

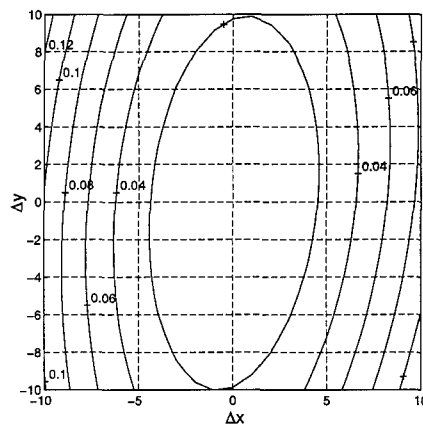
Figure 28. Average structure function surface contours for 81 anchor points at four aperture locations in the turbulent mixing layer. Contours are in units of waves<sup>2</sup>. Each unit of  $\Delta x$  and  $\Delta y$  is 95  $\mu\text{m}$  and 105  $\mu\text{m}$ , respectively. Aperture is centered at: (a) 1.25 cm; (b) 2.25 cm; (c) 3.75 cm; and (d) 5.75 cm from the exit of the turbulence generator.



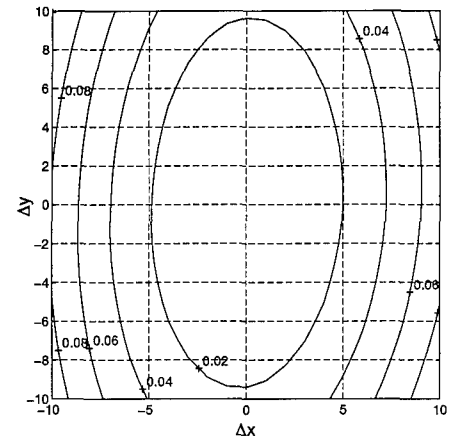
(a)



(b)



(c)



(d)

Figure 29. Average structure function surface contours for 81 anchor points at four aperture locations in the turbulent mixing layer. Contours are in units of waves<sup>2</sup>. Each unit of  $\Delta x$  and  $\Delta y$  is  $95 \mu\text{m}$  and  $105 \mu\text{m}$ , respectively. Aperture is centered at: (a) 8.25 cm; (b) 10.75 cm; (c) 13.25 cm; and (d) 15.75 cm from the exit of the turbulence generator.

#### 4.4 Structure-Function-Based Modeling of Channel Turbulence

As in the free turbulence experiment, the local homogeneity observed at all eight aperture locations is used to develop a model analogous to the Kolmogorov model for atmospheric turbulence, described in Chapter II. For clarity, this development is initially limited to a single location in the turbulent flow, where the effective aperture is centered at 8.25 cm, and the average structure function is represented in Fig. 27. Again, this structure function does not exhibit circular symmetry, a requirement for statistical isotropy. Hence, an attempt to model the structure function using the scalar  $r^{5/3}$  power law given by Eq. (17) is not appropriate. However, as with the free turbulence,  $\alpha_x |\Delta x|^{5/3}$  and  $\alpha_y |\Delta y|^{5/3}$  functions are developed for the orthogonal slices,  $\tilde{D}_\phi(\Delta x, 0)$  and  $\tilde{D}_\phi(0, \Delta y)$ , respectively. Fig. 30 is the result of this power law fit resulting in  $\alpha_x = 4.4 \times 10^{-4}$  and  $\alpha_y = 9 \times 10^{-4}$ . The phase structure functions are in units of waves<sup>2</sup>, while the  $\Delta x$  and  $\Delta y$  units are samples; hence the coefficients,  $\alpha_x$  and  $\alpha_y$ , have units of waves<sup>2</sup> samples<sup>-5/3</sup>. Equivalently, the alpha coefficients may be expressed in units of rad<sup>2</sup>  $\mu\text{m}^{-5/3}$  by the conversion factor,  $(2\pi)^2(\text{sample spacing})^{-5/3}$ , where the sample spacing is 95  $\mu\text{m}$  and 105  $\mu\text{m}$  in  $x$  and  $y$ , respectively. Fig. 31 is a plot of the coefficients  $\alpha_x$  and  $\alpha_y$  as a function of the beam locations. Again, the transition through isotropy is evident in the region between 8.25 cm and 10.75 cm. As with the free turbulence measurements, directional coherence parameters,  $x_0$  and  $y_0$ , are computed. The parameters were computed for the eight aperture locations in the flow and are shown in Fig. 32, where the result from Eq. (41) has been scaled by sample spacing and  $(2\pi)^{-6/5}$  to obtain units of centimeters. For an appreciation of the anisotropy and the crossover of the parameters, the vertical axis of Fig. 32 is on a  $\log_{10}$  scale. Hence, the values for  $x_0$  and  $y_0$  range from approximately 10 cm to less than 0.2 mm, indicating better seeing conditions than that reported for the free turbulence. This improvement is the result of adding the channel, which eliminated the two mixing interfaces with the ambient air.

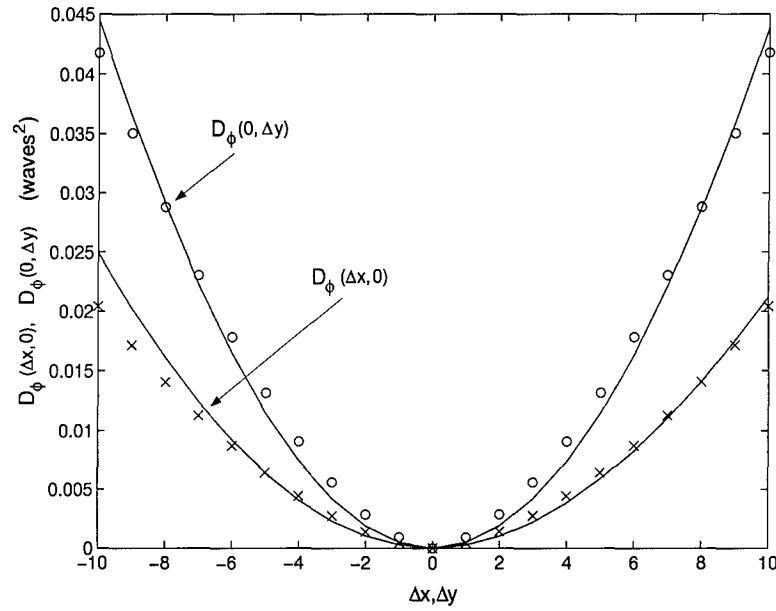


Figure 30. Orthogonal slices of  $\tilde{D}_\phi(\Delta x, \Delta y)$ . Upper curve:  $\tilde{D}_\phi(\Delta x, 0)$ , overlayed ('x') with  $\alpha_x |\Delta x|^{5/3}$  for  $\alpha_x = 4.4 \times 10^{-4} \text{ waves}^2 \text{ samples}^{-5/3}$ . Lower curve:  $\tilde{D}_\phi(0, \Delta y)$ , overlayed ('o') with  $\alpha_y |\Delta y|^{5/3}$  for  $\alpha_y = 9 \times 10^{-4} \text{ waves}^2 \text{ samples}^{-5/3}$ .

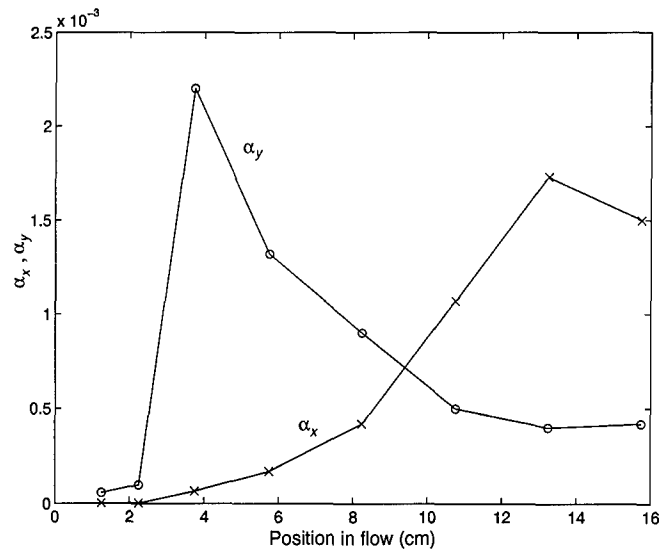


Figure 31. Plot of the coefficients  $\alpha_x$  and  $\alpha_y$  as a function of the eight locations in the flow. Units are  $\text{waves}^2 \text{ samples}^{-5/3}$ .



In terms of the coherence dimensions,  $x_0$  and  $y_0$ , the structure functions may be approximated by

$$\tilde{D}_\phi(\Delta x, \Delta y) \approx 6.88 \left\{ \left( \frac{\Delta x}{x_0} \right)^2 + \left( \frac{\Delta y}{y_0} \right)^2 \right\}^{5/6}, \quad (43)$$

a five-thirds power law representation for Kolmogorov-like, anisotropic flow.

#### 4.5 *Strehl ratio and Reynolds Number Effects*

This section presents and compares four separate SR calculations. Recall from Section 4.2, these are relative SR values; that is, the denominator of Eq. (19) was replaced with the PSF of the imaging system in the absence of turbulence (the reference PSF), a measurable quantity. For completeness, an ‘absolute’ SR was estimated to quantify the optical degradation induced by the imaging system. The estimate was obtained from Eq. (20), where the integrals were replaced with finite, two-dimensional summations. The numerator for Eq. (20) was the normalized system OTF, computed from Eq. (18) for the reference PSF. The denominator for Eq. (20) was a normalized autocorrelation of a zero-phase pupil function [13], where the pupil function geometry may be obtained directly from a camera image (e.g., Fig 20). Using this procedure, the absolute SR was approximately 0.2.

All four SR results are shown in Fig. 33. The first SR is computed from an average of the 160 PSF measurements for each of the eight beam locations in the flow. This result is obtained using Eq. (19) where, for each location, the denominator in Eq. (19) is taken to be the maximum-intensity pixel in the reference PSF. The numerator in Eq. (19) is obtained from the same pixel for the average PSF. This curve is designated by the symbol ‘o’ in Fig. 33. This technique is the most direct for determining SR and the results may be compared, for example, with time-averaged Strehl ratios reported by Chew and Christiansen for a similar experiment [3, 4].

The second SR was computed using Eq. (18) and Eq. (19), where the structure function,  $D_\phi$ , was taken to be the average structure function,  $\tilde{D}_\phi(\Delta x, \Delta y)$  for each location in the flow, and determined from the experimental structure function parameters using Eq. (43). The

relative SR was obtained by including the system reference phase in  $\mathcal{H}_0$  for Eq. (16). This second curve is designated by the symbol 'x' in Fig. 33, and is seen to be in close agreement with the PSF-based SR. This agreement reflects the appropriateness of the approximations leading to the structure-function-based SR; e.g., that the phase,  $\phi(x, y)$  is a zero-mean, Gaussian random process which is stationary in first increments.

The third SR was obtained using Eq. (21), where the on-axis phase variance,  $\sigma_\phi^2$ , was computed from the center point of the 160 measured phase surfaces for each location in the flow. This is a relative SR. The curve is designated by the symbol '+' in Fig. 33. This technique, which assumes the on-axis phase variance is representative of the entire aperture, appears to be a reasonable estimate of the SR over the first few centimeters of the mixing where the Reynolds number is low; however, as depicted in Fig. 33, it significantly underestimates the optical degradation farther downstream.

Finally, the fourth SR, also relative, was computed using Eq. (22), an approximation of Eq. (21) which assumes wide-sense stationarity. The curve is designated by the symbol '\*' in Fig. 33. This technique, which predicts the SR exponentially approaches zero as a function of the growth of the shear layer, again appears to be a reasonable estimate over the first few centimeters when compared to the PSF-based SR. However, it significantly overestimates the optical degradation farther downstream, as shown previously by Chew and Christiansen [4].

A visualization of the flow evolution provides a useful reference for the remainder of this discussion. Figs. 34 and 35 depict an interesting view of the mixing layer in the channel. The images were obtained by propagating the laser beam through the generator-channel assembly which was rotated 90 degrees from the orientation of the ensemble measurements. This orientation provides a visualization of the width of the mixing layer. The flat sides of the images are due to the walls of the channel. The views represent interference images from the first camera in the  $x$ -leg of the shearing interferometer. Hence, the irradiance at the detector plane,  $I_x(x, y)$ , is indicative of the wavefront change in the flow and is given by [37]

$$I_x(x, y) = [1 + \cos(\nabla_x \phi(x, y) \Delta x)], \quad (44)$$

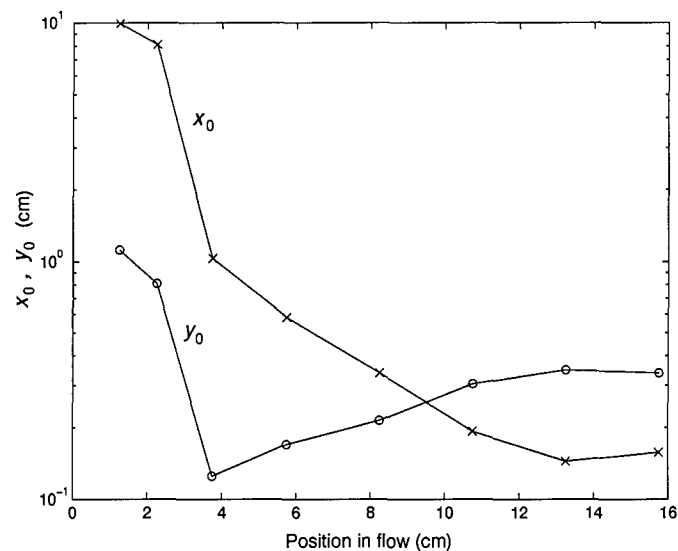


Figure 32. Coherence parameters,  $x_0$  and  $y_0$  as a function of downstream location. The vertical axis is  $\log_{10}$  scale.

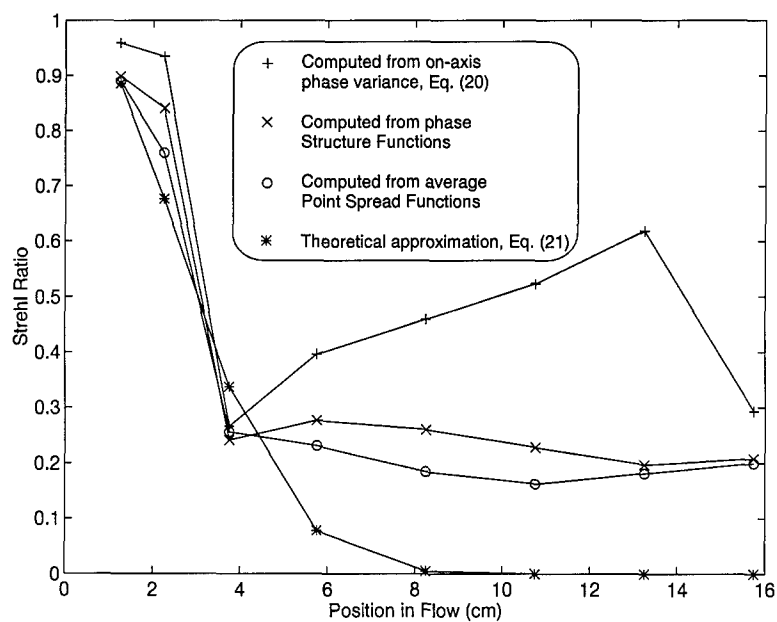


Figure 33. Relative Strehl ratio as a function of downstream location.

where  $\nabla_x$  is the  $x$ -component of the gradient of the density, and  $\Delta x$  is the lateral shear applied to the wave in the  $x$ -leg of the shearing interferometer. For all experiments in this research,  $\Delta x$  was set to approximately one pixel. Note that the images in Figs. 34 and 35 are single realizations. While these realizations are generally representative of the flow evolution, an attempt to physically connect the individual stages in the figures is not appropriate. For this reason, an overlap of the visualization stages was intentionally recorded, providing two independent realizations for some of the locations. In concert, the flow visualizations in Figs. 34 and 35, the Strehl ratios in Fig. 33, the coherence parameters in Fig. 32, and the alpha coefficients in Fig. 31 provide a means to thoroughly assess the flow.

The models which assume wide-sense stationarity appear to yield reasonable predictions for the SR in the pre-transition state of the mixing layer; i.e., the region in the flow where minimal mixing of the two fluids have occurred. For the present experiments this region is within 2 cm of the exit nozzle of the turbulence generator. As seen from Fig. 34, this region appears nearly laminar at the mixing layer interface (center of the aperture). Hence, although the autocorrelation functions are not wide-sense stationary in this region, the limited mixing of the two gases supports the approximations for the aero-optical models.

Mixing transition is characterized by a large increase in the mixed fluid fraction, and is associated with a rapid decrease in the SR [3]. Referring to the Strehl ratios in Fig. 33, transition appears to be in the region of 4 cm, indicated by all four SR calculations. Note from Fig. 34 the mixing of the two fluids may be visualized in this region, evidenced by the presence of a 'braided' core which spreads in width beyond 4 cm. That the  $y_0$  parameter improves beyond 4 cm in Fig. 32 is a consequence of the onset of molecular mixing which would decrease optical degradation in the cross stream direction. The continued degradation in the streamwise direction is a consequence of the continued growth of the mixing layer.

In the post-transition state, the SR has been shown to approach a constant value [3]. In this region, the on-axis variance and mixing layer width models yield poor estimates of the optical degradation. The structure-function-based SR appears to provide accurate predictions in all three states. An interesting region in the flow to further investigate is where the coherence

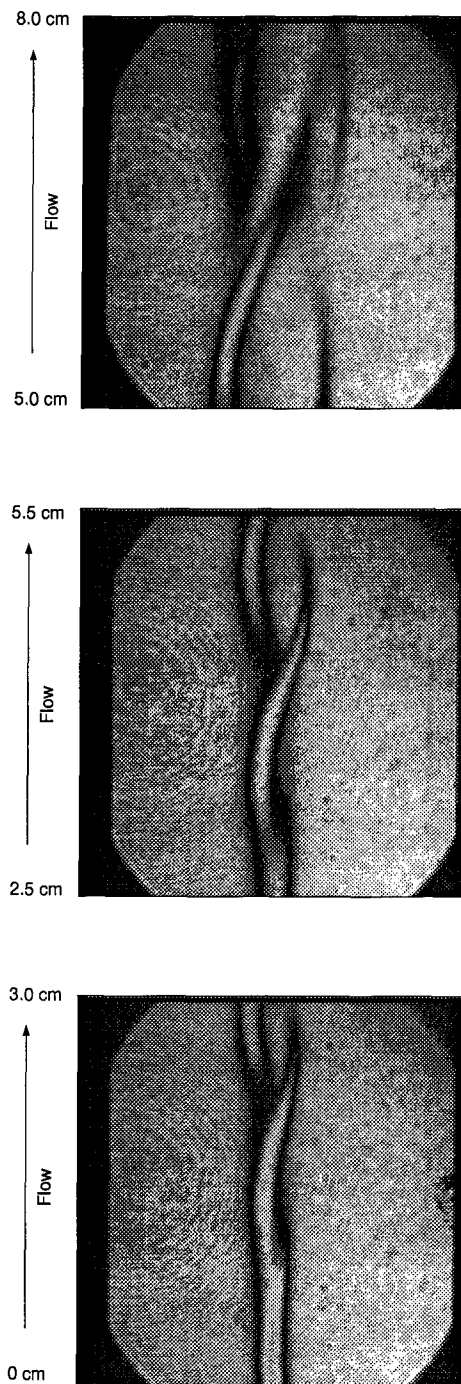


Figure 34. Interference images from one camera in the  $x$ -leg of the shearing interferometer. Gas velocities are 1.5 m/s and 8.5 m/s for the Nitrogen and Helium respectively. Distance along flow axis is with respect to the exit nozzle of the turbulence generator. Channel width is approximately 2.5 cm.

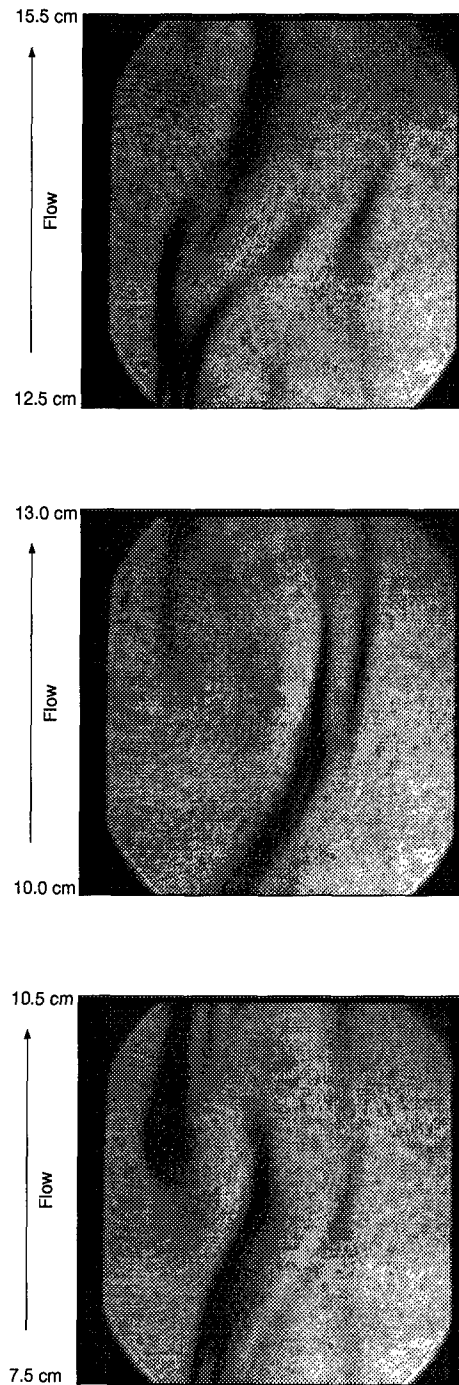


Figure 35. Interference images from one camera in the  $x$ -leg of the shearing interferometer. Gas velocities are 1.5 m/s and 8.5 m/s for the Nitrogen and Helium respectively. Distance along flow axis is with respect to the exit nozzle of the turbulence generator. Channel width is approximately 2.5 cm.

parameters cross over. This crossover occurs between 8.25 cm and 10.75 cm downstream from the exit nozzle, as depicted in Fig. 32. From the flow visualization in Fig. 35, this region is also characterized by a complete mixing in the channel; i.e., the mixing layer width has reached the channel boundaries. Hence, the crossover of the coherence parameters may provide additional insight into the mixing fluid properties. For example, a crossover at 9 cm suggests a  $\delta(x)/x$  of 0.28. This growth rate implies a local Reynolds number,  $Re_\delta/x$  of  $1244\text{ cm}^{-1}$  and a mixing coefficient,  $C_\delta$ , of approximately 0.26. Note that the variance model approaches the PSF and structure function models in the region of 16 cm. This property was also observed in the region of 30 cm for the free turbulence [8], suggesting the variance model may be appropriate well-beyond the transition region; i.e., in a fully-developed flow.

For the flow region beyond 13 cm, the two coherence parameters approach constant values. This property may again be attributed to the full development of the mixing layer within the channel. The similarity of the density fluctuations is evident in the flow visualization images in Fig. 35. Referring to Fig. 31, the streamwise coefficient,  $\alpha_x$ , is approximately three times that of the cross-stream coefficient,  $\alpha_y$  in the region of 15 cm. This factor is consistent with the results reported for the free turbulence in the region beyond 10 cm, and with typical scale sizes reported by Sutton [48]. However, a crossover of the coefficients was not observed in the free turbulence. Hence, the structure functions provide valuable insight into the anisotropic properties of mixing layers in the transition and post-transition states of the flow.

#### 4.6 *Mixing characteristics for other Reynolds numbers*

For both the free-turbulence experiments and the channel-flow turbulence, the velocities for the Helium and Nitrogen gases have remained fixed. This section provides a small set of flow visualizations for mixing layers with different velocities. These are intended to qualitatively complement the earlier experiments. Once again the visualizations are obtained from a single camera in the x-leg of the shearing interferometer, providing an interference image whose contrast variation is proportional to the density variation in the mixing layer.

The turbulent flow is confined within the rectangular channel and is oriented for a 'side view' of the mixing layer. The velocities were chosen such that the Reynolds number per centimeter,  $Re_x/x$ , is doubled over three sets of velocities. Recall the previous experiments had a  $Re_x/x$  of  $4444\text{ cm}^{-1}$ . Thus two other velocity combinations were selected which provided a  $Re_x/x$  of  $2222\text{ cm}^{-1}$  and  $8888\text{ cm}^{-1}$ . The fluid parameters are summarized in Table 2, where the second velocity profile is the one used for the previous experiments in this research, and whose flow visualizations were previously presented in Figs. 34 and 35. The flow visualization images for the other two velocity profiles are shown in Fig. 36 through Fig. 39. For the remainder of this discussion the three entries in Table 2 will be referred to as profiles 1, 2, and 3, relating to a  $Re_x/x$  of 2222, 4444, and 8888  $\text{cm}^{-1}$ , respectively. In Table 2 the growth rate,  $\delta(x)/x$ , was estimated for profiles 1 and 3 using Eq. (30) and a mixing coefficient,  $C_\delta$  of 0.26. Recall this mixing coefficient was estimated based on the crossover of the structure function coherence parameters in Section 4.5. Since the mixing coefficient is highly dependent on initial conditions [5], it's not clear that the estimate derived from profile 2 can be extended to profiles 1 and 3; however, the flow visualizations may provide an indication of the appropriateness of this extension.

The mixing characteristics for profile 1, which has a  $Re_x/x$  of  $2222\text{ cm}^{-1}$  is shown in Figs. 36 and 37. In the region just beyond the exit jet of the turbulence chamber (i.e., 0-3 cm), the contrast across the mixing layer appears less sharp than that observed with the higher velocities of profile 2, as shown in Fig. 34. This is likely attributed to an earlier mixing of the lower speed gases, although the Reynolds number is below that associated with a turbulent transition. Furthermore, the emergence of the braided core structure, associated with a molecular mixing transition, is delayed by approximately 1 cm in comparison to Fig. 34 for profile 2. From Fig. 37, the mixing layer was found to reach the width of the channel in the region of 10 cm. This observation supports the estimate of a growth rate of 0.25, suggesting that the mixing coefficient derived from profile 2 is also valid for profile 1.

The mixing characteristics for profile 3, which has a  $Re_x/x$  of  $8888\text{ cm}^{-1}$  is shown in Figs. 38 and 39. This profile is characterized by a rapid appearance of a braided core.



Table 2. Fluid parameters for three He/N<sub>2</sub> mixing ratios (for  $C_\delta = 0.26$ ).

He Velocity (m/sec)	N <sub>2</sub> Velocity (m/sec)	$Re_x/x(\text{cm}^{-1})$	$\delta(x)/x$	$Re_\delta/x(\text{cm}^{-1})$
4.5	1.0	2222	0.25	564
8.5	1.5	4444	0.28	1244
16.0	2.0	8888	0.34	3010

The mixing layer was found to reach the width of the channel in the region 7 cm. Again, this observation supports the estimate of a growth rate of 0.34, suggesting that the mixing coefficient derived from profile 2 is also valid for profile 3.

#### 4.7 Summary of Turbulent Mixing Layers in Channel Flow

The shearing interferometer was used to generate a statistical ensemble of optical phase fluctuations due to propagation through a high-Reynolds-number mixing layer. A channel-flow mix of Helium gas at 8.5 m/sec and Nitrogen gas at 1.5 m/sec induced optical phase perturbations. An ensemble of wave front phase measurements was obtained for eight aperture locations in the flow. The autocorrelation function and phase structure function were computed for each ensemble. Additionally, simultaneous measurements of the corresponding point spread functions were obtained.

The autocorrelation function results indicate the phase fluctuations are not wide-sense stationary; hence, as with the free turbulence measurements, the channel flow cannot be appropriately modeled using the aero-optical equations. The structure function results indicated the random phase fluctuations were stationary in first increments, though not isotropic. Hence, a direct application of a Kolmogorov five-thirds power law was not appropriate. However, an analogous five-thirds power law was developed for orthogonal flow components. Two directionally-dependent coherence parameters were introduced, analogous to the single atmospheric coherence diameter,  $r_0$ , for Kolmogorov turbulence. The parameters provide a measure of the anisotropy in the flow. A plot of the coherence parameters versus location in

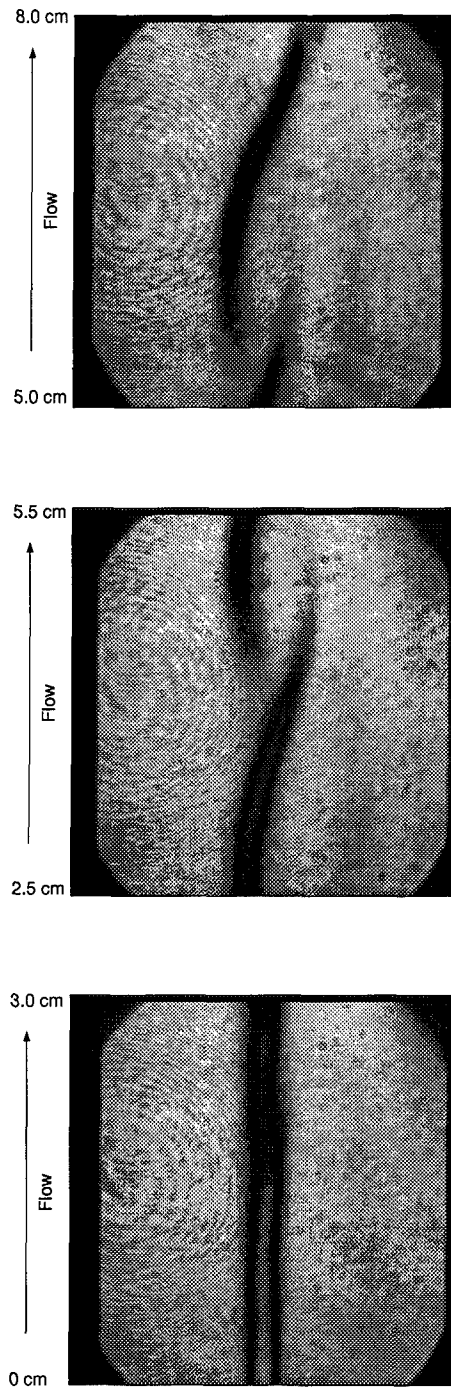


Figure 36. Interference images from one camera in the  $x$ -leg of the shearing interferometer. Gas velocities are 1.0 m/s and 4.5 m/s for the Nitrogen and Helium respectively. Distance along flow axis is with respect to the exit nozzle of the turbulence generator. Channel width is approximately 2.5 cm.

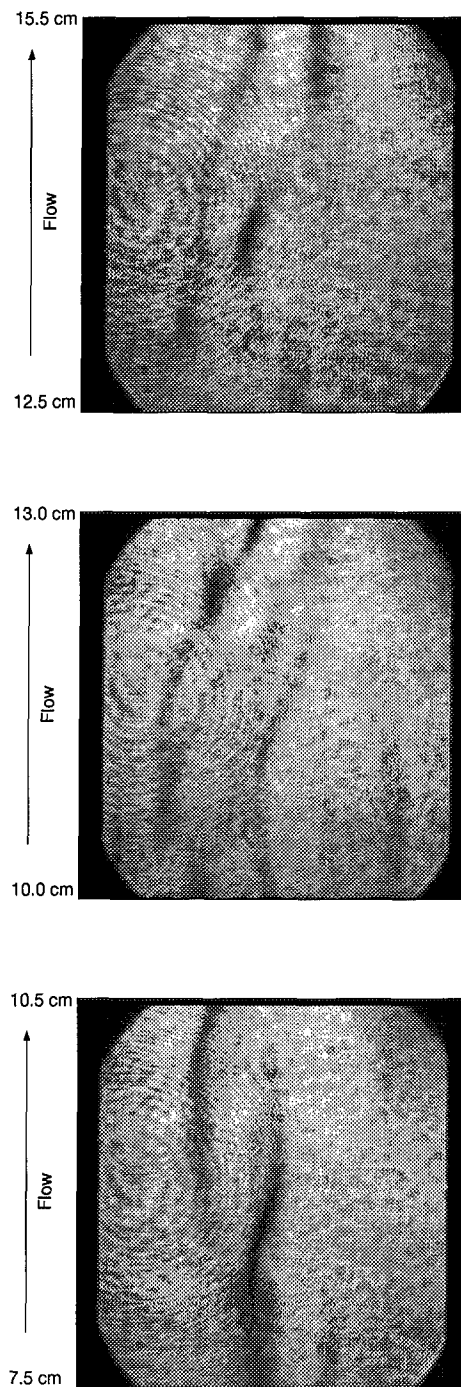


Figure 37. Interference images from one camera in the  $x$ -leg of the shearing interferometer. Gas velocities are 1.0 m/s and 4.5 m/s for the Nitrogen and Helium respectively. Distance along flow axis is with respect to the exit nozzle of the turbulence generator. Channel width is approximately 2.5 cm.

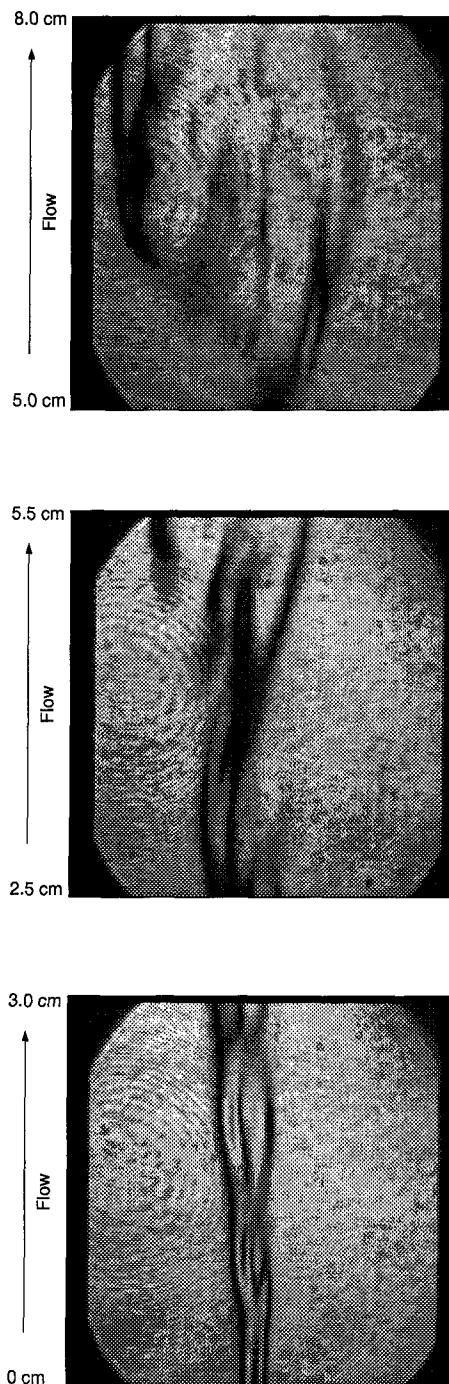


Figure 38. Interference images from one camera in the  $x$ -leg of the shearing interferometer. Gas velocities are 2.0 m/s and 16.0 m/s for the Nitrogen and Helium respectively. Distance along flow axis is with respect to the exit nozzle of the turbulence generator. Channel width is approximately 2.5 cm.

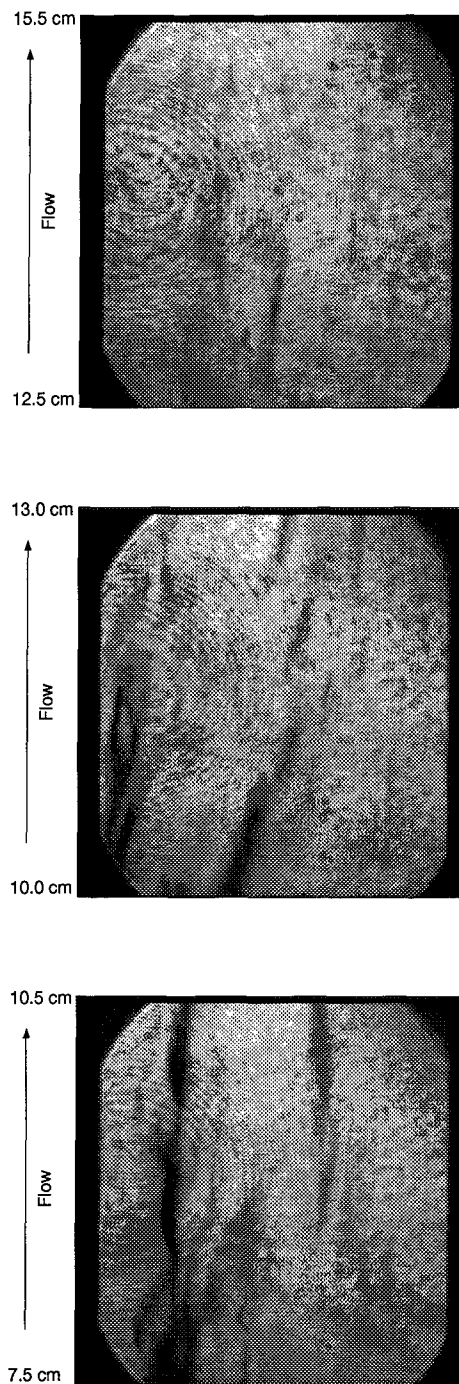


Figure 39. Interference images from one camera in the  $x$ -leg of the shearing interferometer. Gas velocities are 2.0 m/s and 16.0 m/s for the Nitrogen and Helium respectively. Distance along flow axis is with respect to the exit nozzle of the turbulence generator. Channel width is approximately 2.5 cm.

the flow indicated a local region of isotropy in the region between 8.25 cm and 10.75 cm. This region is coincident with a maximization of the mixing layer width in the channel.

Four independent, Strehl ratios were computed using the average point spread functions, average structure functions, on-axis phase variance, and estimation of the mixing layer width. The latter two calculations assume wide-sense stationarity and provide poor estimates of the optical degradation beyond a few centimeters of the mixing, when compared to the point spread function measurements. The structure function calculations provide a reasonable Strehl ratio estimate throughout the flow, as well as a measure of the statistical anisotropy in the flow.

## V. TIME-RESOLVED MEASUREMENTS IN CHANNEL FLOW

### 5.1 Overview

In this chapter a pair of high-speed (1kHz) cameras are used to obtain a large set of measurements to characterize the He/N<sub>2</sub> mixing layer in an orientation which was orthogonal to the orientation described in Chapters III and IV. For the present measurements, the mixing layer was oriented such that the laser propagation direction was parallel to the plane of the mixing layer. These experiments were motivated by the need to assess the validity of the Taylor hypothesis for frozen flow, an assumption which is often assumed for turbulent mixing layers, particularly for small-aperture beam techniques [21]. The present mixing layer orientation provides the best visualization of turbulent structures, as demonstrated by the flow visualization images presented in Chapter IV.

The present experimental setup affords the capability of collecting simultaneous (i.e., frame-registered) images of the turbulent flow from a pair of cameras at rates of 1000 non-interlaced frames per second. The combination of measurements reported are simultaneous shadowgraphs and wavefront slopes which were used to evaluate the temporal characteristics of the flow, and simultaneous point spread functions and wavefront slopes which were used to evaluate the spatial characteristics of the flow, similar to the calculations presented in the previous chapter. The wavefront slopes are obtained using a Hartmann wavefront sensor, composed of a two-dimensional lenslet array coupled with one of the cameras.

The chapter begins with a description of the experimental setup used to obtain the turbulence measurements. This is followed by a presentation of sequential shadowgraph images. The shadowgraph images are assessed for frozen flow characteristics using a novel technique of computing an array of correlation coefficients over a two-dimensional sliding window for various temporal separations. The same computational technique is then applied to a series of phase surfaces which were reconstructed from the slope measurements, collected simultaneously with the shadowgraphs. Next the series of slope measurements which were collected with the point spread functions are reconstructed and the phase surfaces are assessed

for statistical homogeneity through structure function calculations. Finally, Strehl ratios are reported from the average point spread functions.

## 5.2 Experimental Setup

The optical bench used for the experiments is shown in Fig. 40. A 2 cm diameter, collimated laser beam was transmitted through the turbulent flow at various distances from the exit of the turbulence generator. Note that the orientation of the splitter plate in the exit nozzle of the turbulence generator has been rotated 90 degrees relative to the two previous experiments. Hence, for propagation in the  $z$  direction and a vertical flow of the gases in the  $x$  direction, the shear layer of the mixing gases is in the  $(x, z)$  plane. This orientation will be referred to as a 'side view' of the mixing layer. It was determined that this orientation would provide the most interesting view of the density gradients in the mixing layer. Note that this orientation is the same as that used to generate the flow visualization images in the previous chapter in Fig. 34 through Fig. 39. The velocity profile selected for these experiments is profile 1 from Table 2. This profile gives a  $Re_x/x$  of  $2222\text{ cm}^{-1}$ . The rationale for this selection is discussed later in this section.

At the first non-polarizing beam splitter (NPBS), the laser power was evenly divided between the shearing interferometer and the path to the two high-speed cameras. The path for the shearing interferometer was identical to the description given in Chapter IV. For this experiment, the shearing interferometer was used primarily as a flow visualization tool. The interference images provided a real-time capability to monitor the mixing characteristics at the various flow positions during data collection.

At the second NPBS, half of the power was transmitted to the optional high-speed camera. This path was configured for two different experiments. The first configuration recorded shadowgraph images. In this configuration, lens 5 consisted of a 450 mm lens, placed in the path at approximately 550 mm from the camera. This provided a shadowgraph image of the turbulent field which just filled the camera detector. The shadowgraph technique is described in more detail in Section 5.3.1. The second configuration recorded point spread functions



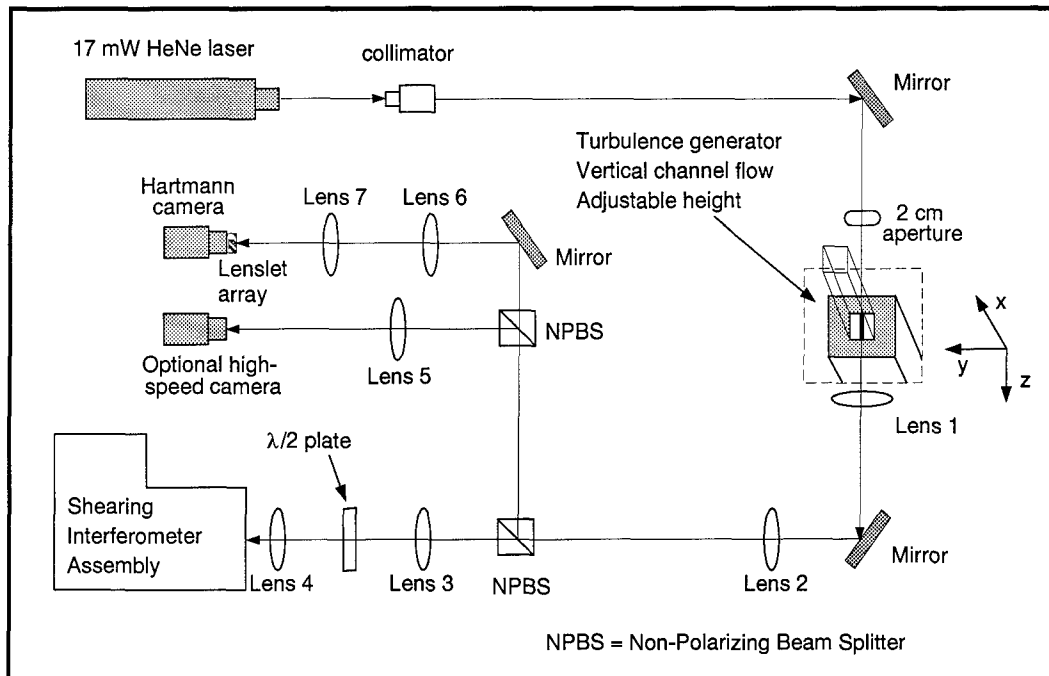


Figure 40. Optical bench used to obtain shadowgraphs, point spread functions, and phase measurements for a laser beam propagating through the turbulent mixing layer.

(PSF) using a 1000 mm focal length lens in the lens 5 position. This measurement was similar to the PSF's which were recorded for the channel flow measurements in Chapter IV. The present PSF configuration differs in several ways from the earlier channel measurements. The present PSF's were collected at much faster rates (1000 Hz versus 60 Hz). Additionally, they were collected at a different velocity profile (profile 1 versus profile 2) and at a different beam propagation orientation to the mixing layer. Results from the two experimental configurations will be presented separately in this chapter.

The remaining power from the second NPBS was transmitted through a collimating lens pair, lens 6 and lens 7, which provided sufficient demagnification for the beam to fill the CCD array of the Hartmann camera. The Hartmann wavefront sensor system consisted of a monolithic lenslet array and the high-speed camera. The lenslet array consisted of a grid of  $20 \times 20$  square subapertures, each measuring 203 microns on a side and having a focal length of 7.8 mm. In concert, the lenslet array and the imaging camera provided a two-dimensional

measure of the wavefront slope of the perturbed beam. The technique will be described in more detail later in this chapter.

Both of the high-speed cameras used for these experiments were MD4256C solid state video cameras manufactured by EG&G Reticon. The CCD array had an active imaging area of  $4.1 \times 4.1$  mm, composed of  $256 \times 256$  pixels. The cameras were capable of operating at a maximum frame rate of 1000 non-interlaced frames per second (fps). For all of the measurements reported in this chapter, the maximum frame rate was used. One disadvantage with these cameras was the absence of a built-in, adjustable shutter. When the camera was running at 1000 fps, the integration time was approximately 1 ms. Recall that the slower 60 Hz cameras on the shearing interferometer had a selectable shutter which enabled an exposure time of 0.5 ms. It was determined that the longer exposure times on the EG&G cameras dictated the need to reduce the gas velocities for these experiments. Note that a better solution is to place in the path an optical shutter which is capable of sub-millisecond cycling. This device was not available at the time of this research; however, it is highly recommended for future experiments using these cameras.

For both experimental configurations, the Hartmann camera and the optional camera were triggered externally from a function generator to obtain simultaneous, frame-registered images of the turbulent flow at rates of 1kHz. A triggering anomaly was observed in the procedure which proved to be a useful quality control test. It was noted that when the function generator was switched off (manually) at the conclusion of a recording session, the last recorded frame was completely washed out. Hence, for a 256-frame measurement, only 255 frames were usable. The camera software was designed to overwrite frames in the 256-frame buffer until recording was terminated; therefore, the washed out frame could occur on any of the frames for a given experiment. A simple test for frame registration was to confirm the washed out frame occurred at the same frame number for both cameras. Over 16 sets of measurements, this test was satisfied every time.

Given the need for a lower velocity profile, the gas velocities selected for these experiments were 4.5 m/s for the Helium gas and 1.0 m/s for the Nitrogen gas. Note this is profile 1

given in Table 2. Hence, the Reynolds number,  $Re_x/x$ , for these experiments was  $2222\text{ cm}^{-1}$ . A flow visualization of this profile for a region covering 0 to 15 cm from the exit nozzle of the turbulence generator may be seen in Figs. 36 and 37 in Chapter IV. Wavefront slopes and either PSF's or shadowgraphs were measured at eight locations in the flow. The locations were centered on 1.25 cm, 2.5 cm, 3.75 cm, 5.0 cm, 7.5 cm, 10.0 cm, 12.5 cm, and 15.0 cm downstream of the exit of the turbulence generator. These locations can be equivalently expressed in terms of a dimensionless  $X/D$  parameter, where  $X$  is the location of the beam in the flow, and  $D$  is the length of one side of the exit nozzle. Thus, for the present experiment, the  $X/D$  locations are approximately 0.5, 1.0, 1.5, 2.0, 3.0, 4.0, 5.0, and 6.0.

### 5.3 Simultaneous Shadowgraphs and Wavefront Measurements

This section presents the results from the simultaneous realizations of shadowgraphs and wavefront slopes for eight beam locations in the turbulent mixing layer. The full data set consisted of 255 frame-registered images for each flow location, for a total of 4096 images, excluding flat field, dark frame, and reference measurements. For all images reported in this section, dark frame and flat field calibrations have been performed [42]. Statistical calculations reported in this section are with regard to the temporal properties of the phase fluctuations. Spatial statistics (e.g.; phase structure functions) are addressed in the next section which reports the simultaneous point spread functions and wavefront slopes.

*5.3.1 Time-resolved Shadowgraphs.* In this section, a series of shadowgraph images is reported for the eight locations in the flow. The shadowgraphs provide an additional flow visualization of the mixing layer. Additionally, the shadowgraphs provide a means to 'track' the propagation of coherent structures as a visual assessment of the frozen flow hypothesis.

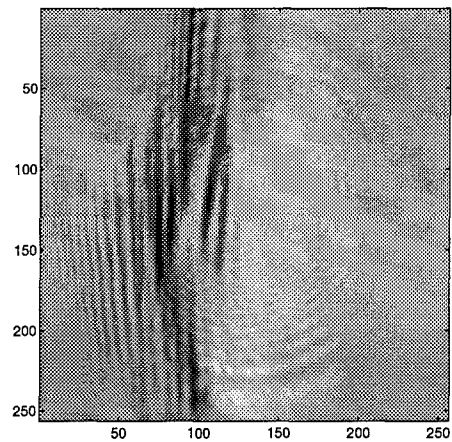
The shadowgraph is a relatively simple means for visualizing turbulent flows when fine details of the density variations are not required [17]. The contrast,  $h$ , observed in a shadowgraph is related to the density by [1]

$$h = L \int_0^D \left( \frac{\partial^2 \rho}{\partial x^2} + \frac{\partial^2 \rho}{\partial y^2} \right) dz, \quad (45)$$

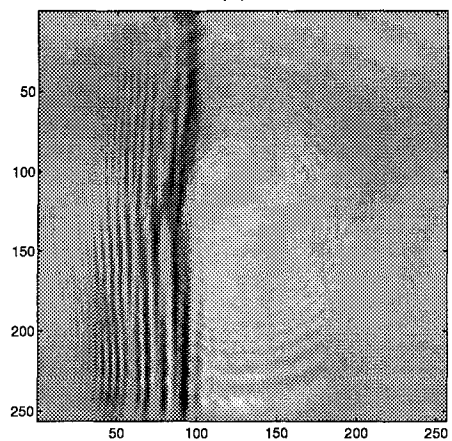
where  $L$  is the distance from the centerline of the channel to the shadowgraph plane. It may be seen from the optical bench schematic in Fig. 40 that the placement of imaging lens 1 in close proximity to the channel ensures a good spatial correspondence between the shadowgraph and the true density field [17]. The relationship between the shadowgraph and density fluctuations is based on geometrical optics approximations, which was shown in Chapter II to be limited to regions of slowly varying density. However, extraction of density fluctuations have been performed digitally using the model in Eq. (45) on shadowgraphs obtained from air flows with a free stream Reynolds number of  $7 \times 10^5 \text{ cm}^{-1}$  [1]. The results were in excellent agreement with independent measurements from cross-wire anemometry.

Figures 41 through 43 provide single realizations of shadowgraphs for the eight beam locations in the mixing layer. As with the interference images presented in Chapter IV, these are independent realizations, and an attempt to physically connect the figures is not appropriate. The contrast variations across the aperture are indicative of the second derivative of the density in the flow. Hence, the dark vertical bands seen in the center of the aperture in Fig. 41 are due to the strong density gradient which occurs at the He/N<sub>2</sub> interface. As noted in the figures, the Helium gas is on the left side of the aperture. It's not clear what mixing phenomena are responsible for the striated bands on the Helium side of the aperture; however, it's noted that these bands vanish in the flow region of 10 cm where the mixing layer is maximized in the channel.

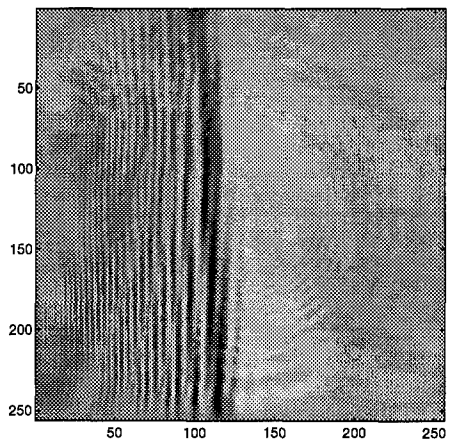
A preliminary, and somewhat qualitative assessment of the frozen flow hypothesis may be performed on the time-resolved shadowgraphs. An interesting test point to evaluate is at 15 cm in the flow where, as seen from Fig. 43, the turbulent mixing is characterized by relatively small and scattered structures. It should be noted that even for the low velocity profile and high frame rates for this experiment, there still exists some substantial averaging of the turbulence. The laser beam diameter is 2 cm in the turbulent flow. If the mean velocity of the flow is assumed to be approximately equivalent to 4.5 m/s (i.e., the velocity of the



(a)

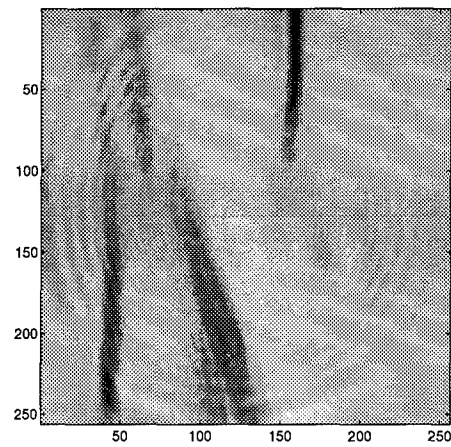


(b)

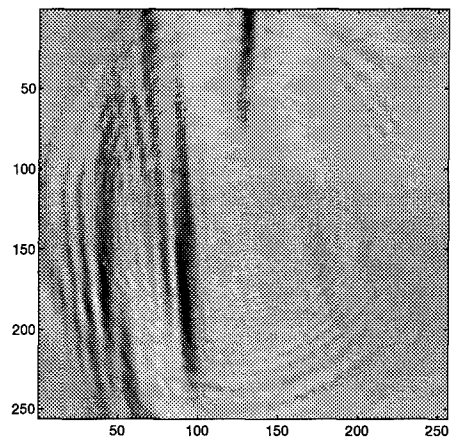


(c)

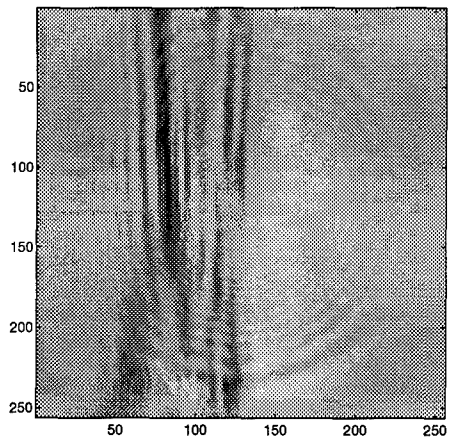
Figure 41. Shadowgraph images for a 2 cm diameter beam in the mixing layer. Helium is on the left; Nitrogen is on the right. Flow is upward. Aperture is centered at (a) 1.25 cm, (b) 2.5 cm, and (c) 3.75 cm in the flow.



(a)

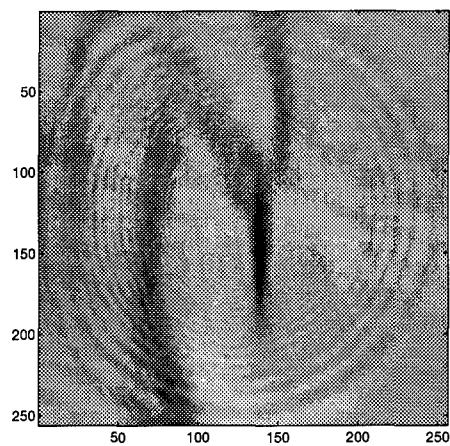


(b)

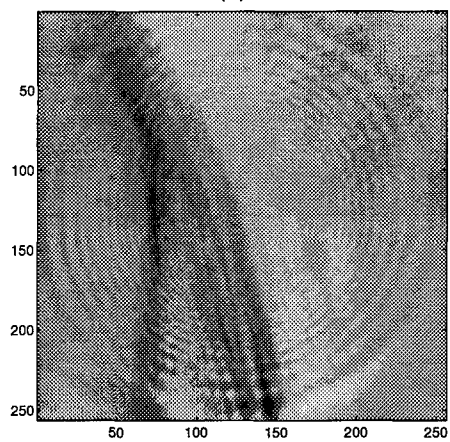


(c)

Figure 42. Shadowgraph images for a 2 cm diameter beam in the mixing layer. Helium is on the left; Nitrogen is on the right. Flow is upward. Aperture is centered at (a) 5.0 cm, (b) 7.5 cm, and (c) 10.0 cm in the flow.



(a)



(b)

Figure 43. Shadowgraph images for a 2 cm diameter beam in the mixing layer. Helium is on the left; Nitrogen is on the right. Flow is upward. Aperture is centered at (a) 12.5 cm, and (b) 15.0 cm in the flow.

higher-speed gas), then a particle moving at the mean velocity will traverse the aperture in 4.4 ms. The EG&G camera, operating at 1000 fps, has an integration time of approximately 1 ms; hence, the movement of the particle will be temporally averaged over approximately one-fifth of the aperture. The consequence of this averaging will be indicated by a smearing of the coherent structures in the shadowgraphs. The Taylor hypothesis states that over a small time interval,  $t_2 - t_1 = \tau$ , the turbulent fluctuations have a constant velocity, in space and time, equal to the mean velocity in the flow. In the shadowgraphs, frozen flow will be indicated by the persistence of coherent structures over several consecutive flow realizations.

Figures 44 through 47 display a series of 16 sequential shadowgraph realizations at 15 cm in the flow, recorded at 1000 fps. The image sequence is (a) through (d) for each figure. An example of an isolated structure which appears to persist with little visible change has been designated with a series of arrows in Fig. 44 (b) through (d) and continuing in Fig. 45 (a) and (b). Note that the presence of the structure over five shadowgraph realizations suggests a velocity of the structure in the range of 4 to 4.5 m/s. Similar examples of structure preservation may be 'tracked' in the 16-frame sequence. In general, small isolated structures appeared to be preserved over 3 to 5 frames for realizations beyond 10 cm. This would suggest some validity to the frozen flow hypothesis for these experimental conditions for isolated examples. For regions closer to the exit nozzle, the shadowgraphs lacked the morphology to make any conclusions. It should be noted, however, that the smaller structures were generally observed in a vertical band near the center of the aperture. At the outer regions of the aperture, the structures were generally longer with less morphology. This may be, in part, due to the boundary layer effects induced by the channel wall. Therefore, frozen flow indications are generally more difficult to determine on the outer region of the aperture. As a final observation, referring to the structure designated by the arrows in Figs. 44 and 45, the structure is seen to move slightly in the cross stream direction (left to right) as it propagates streamwise. In general, all structures observed in the shadowgraphs exhibited some lateral displacement in the visualization sequences. The displacement was observed to be nonuniform in both magnitude and direction. The next section presents a more quantitative assessment of the shadowgraphs



for frozen flow characteristics using a technique which evaluates the average flow properties over a 255-frame ensemble.

**5.3.2 Temporal Analysis of Shadowgraphs.** This section introduces a spatial-temporal analysis technique to determine the validity of the frozen flow hypothesis for the measured shadowgraphs. The technique was one which digitally computed correlation coefficients using a windowed region of a shadowgraph realization, which was slid across the aperture of a frame separated in time by  $\tau$ . The full ensemble of 255 frames was used such that the coefficients were time-averaged. Recall the shadowgraph time sequences indicated a lateral displacement of the turbulent structures as they propagated in the streamwise direction. It was determined that this characteristic dictated the need for a two-dimensional sliding window algorithm in computing the frame to frame correlations. For the two-dimensional signals,  $A(m, n)$  and  $B(m, n)$ , the correlation coefficient,  $r$ , is given by [22]

$$r = \frac{\sum_m \sum_n A(m, n) B(m, n)}{\sqrt{\sum_m \sum_n A^2(m, n) \sum_m \sum_n B^2(m, n)}}. \quad (46)$$

Note that when  $A$  and  $B$  are equal, the correlation coefficient is unity. For the shadowgraph images, a three-dimensional coefficient array was computed which accounted for the temporal separation,  $\tau$ , of the images as well as the spatial shift parameters,  $(k, l)$ , of the sliding window. Thus, Eq. (46) may be expanded to obtain

$$\bar{r}(k, l, \tau) = \frac{1}{N - \tau} \sum_{i=1}^{N-\tau} \frac{\sum_m \sum_n A_i(m, n) B_{i+\tau}(m + k, n + l)}{\sqrt{\sum_m \sum_n A_i^2(m, n) \sum_m \sum_n B_{i+\tau}^2(m + k, n + l)}}, \quad (47)$$

where  $\bar{r}$  denotes an ensemble average. A pictorial representation of this operation is shown in Fig. 48. A  $41 \times 21$  template window, 'A', was uniquely defined on a  $128 \times 63$  vertical strip which encompassed the  $128 \times 128$  image array. The spatial features within the fixed window,  $A$ , were then correlated over the entire region of the vertical strip, for a given frame separation, using  $(k, l)$  shifts of one pixel in  $x$  or  $y$ . The vertical strip was defined to

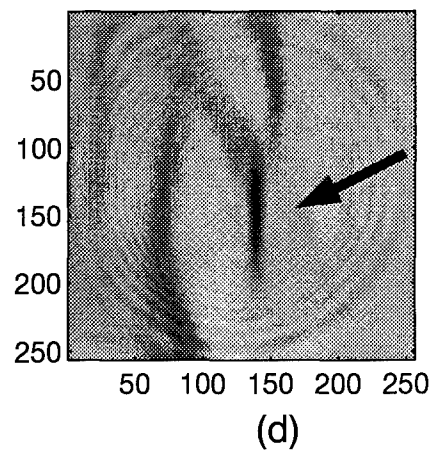
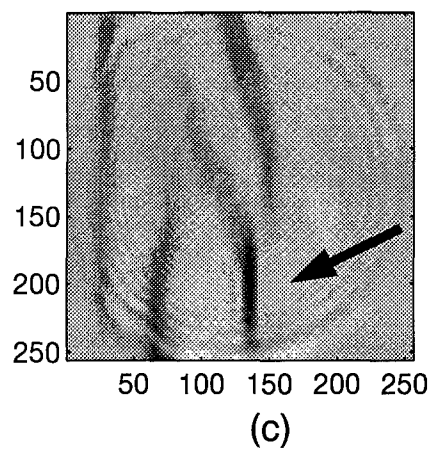
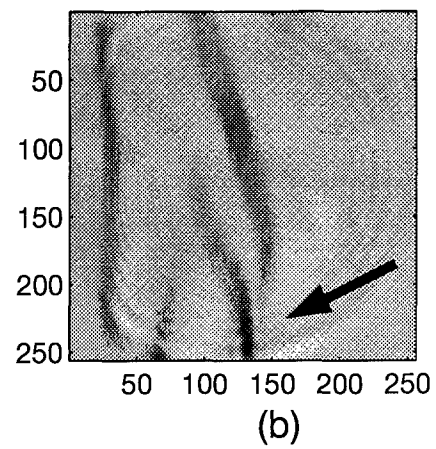
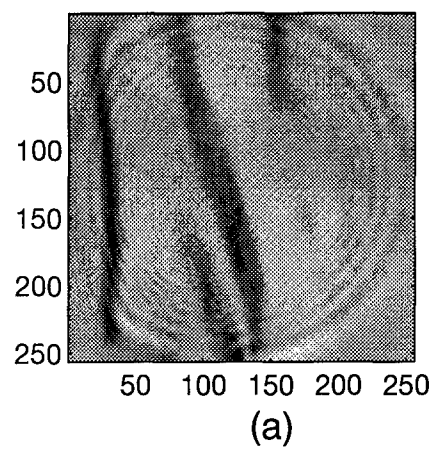


Figure 44. Shadowgraph sequence for four realizations at 1000 fps and 15 cm in the flow. Flow is upward. Sequence is (a) through (d).

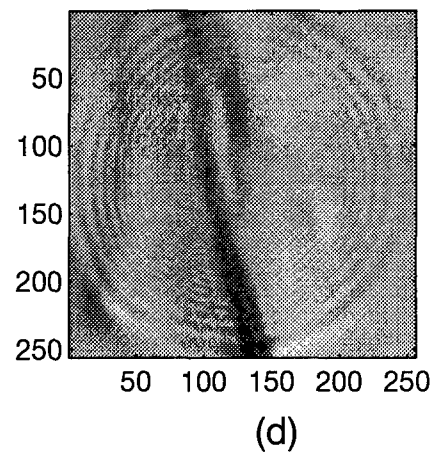
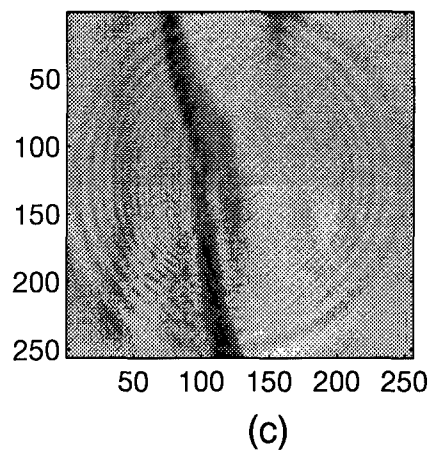
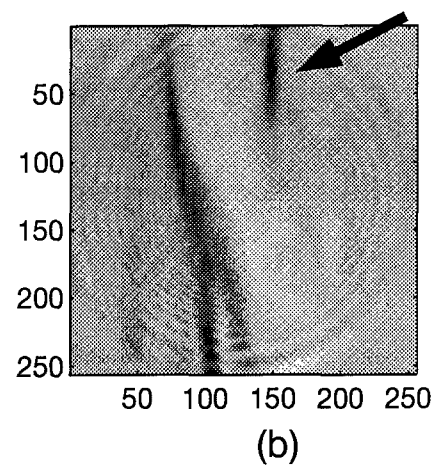
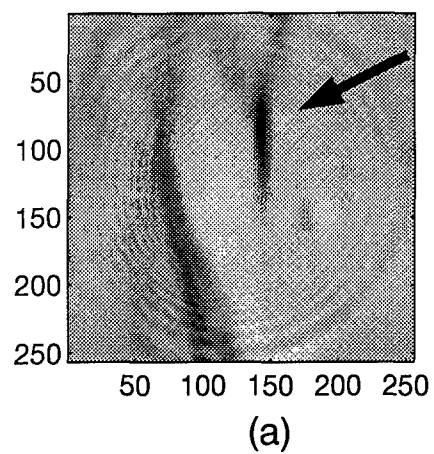
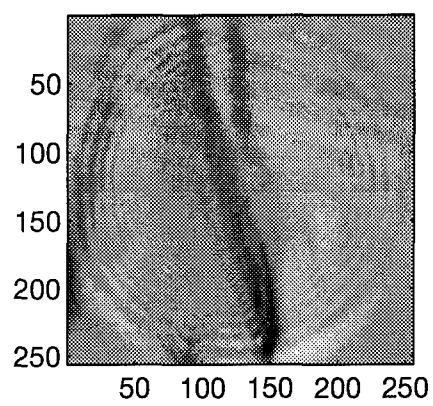
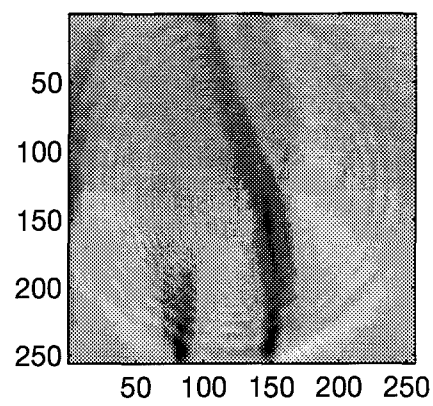


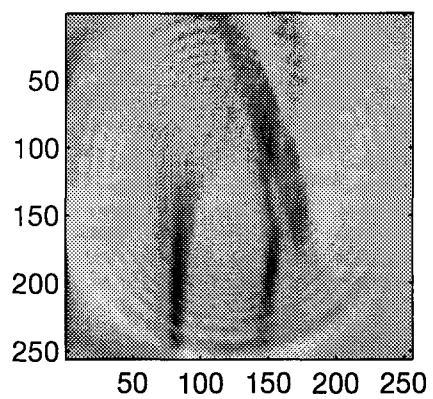
Figure 45. Continuation of the shadowgraph sequence for four realizations at 1000 fps and 15 cm in the flow. Flow is upward. Sequence is (a) through (d).



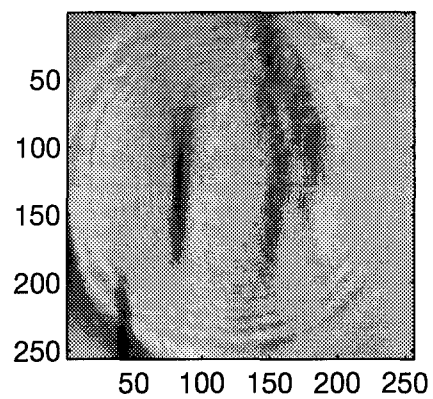
(a)



(b)



(c)



(d)

Figure 46. Continuation of the shadowgraph sequence for four realizations at 1000 fps and 15 cm in the flow. Flow is upward. Sequence is (a) through (d).

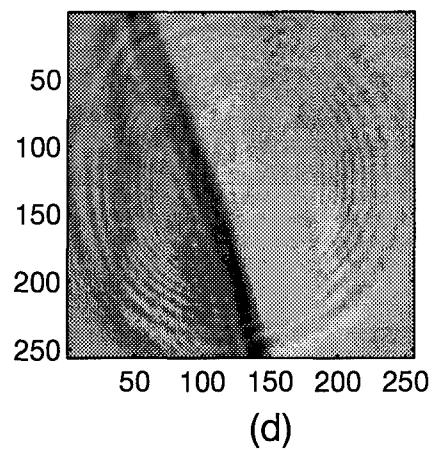
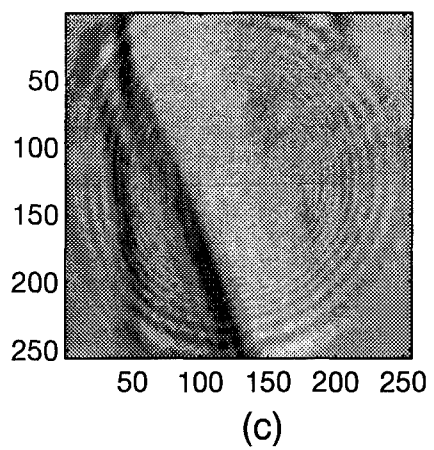
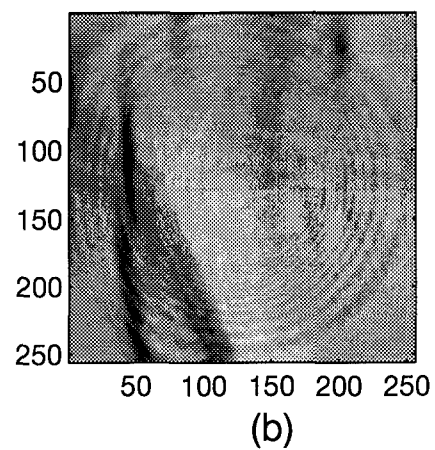
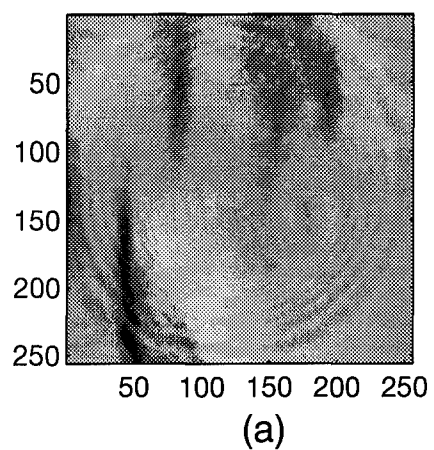


Figure 47. Continuation of the shadowgraph sequence for four realizations at 1000 fps and 15 cm in the flow. Flow is upward. Sequence is (a) through (d).

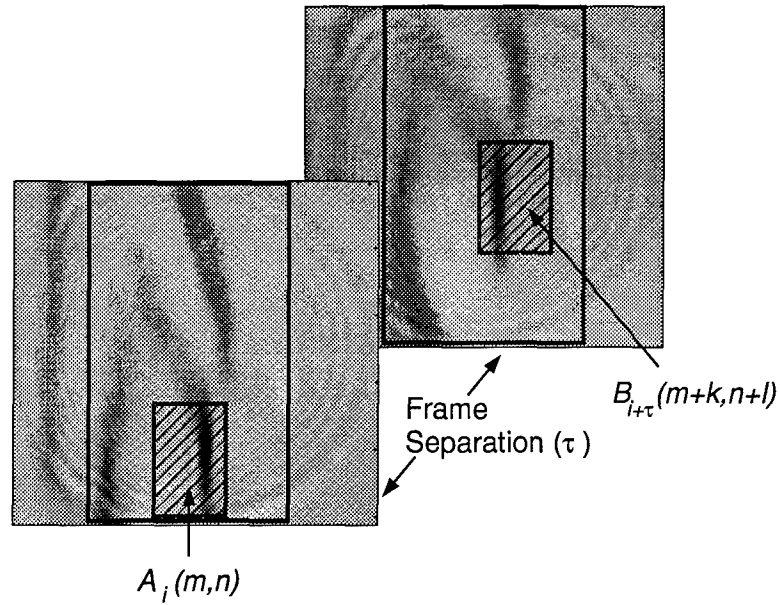


Figure 48. Pictorial representation of the operation performed to obtain the correlation coefficient arrays.

encompass a maximum region of the aperture in the streamwise direction, while minimizing multiplication of the window with regions outside the circular aperture. The window size was empirically selected. The window had to be large enough to enclose morphologically significant structures, yet small enough to provide a relevant array size for the correlation coefficients. The scale size of the structures are largest in the streamwise direction, thus permitting a rectangular window. Note the placement of the template window  $A$  is at the bottom of the aperture and in the center of the vertical strip. This placement allowed for complete tracking of a structure across the aperture in the streamwise direction, and laterally for one full window width on either side in the cross stream direction. For a fixed  $k$ ,  $l$ , and  $\tau$ , the parameter  $\bar{r}$  was computed using Eq. (47). The window was then shifted until complete coverage of the vertical strip was complete. The result for a given  $\tau$  is a  $87 \times 43$  array of correlation coefficients.

Figs. 49 through 52 are images of the coefficient arrays for frame separations between 0 and 5, where each frame is separated in time ( $\tau$ ) by 1 ms. The figures are for the eight flow locations. For example, Fig. 49 (a) shows a 6-frame sequence of array images at 1.25 cm

in the flow. The whiter regions represent higher correlations, and the peak coefficient in the array for each frame separation is designated by the symbol 'o'. Note for  $\tau = 0$ , the peak coefficient is located where the window 'A' was defined, indicating an autocorrelation of the window. For the frozen flow hypothesis to be valid, the correlation peak should move upward with increasing values of  $\tau$ . This feature was found to be present for beam locations greater than 1.25 cm, over 2 to 4 frame separations. At 1.25 cm in the flow, the laminar streams at the mixing layer result in a structure which is highly-correlated in the streamwise direction over the entire aperture. An interesting phenomenon seen in Fig. 49 (a) is the non-vertical aspect of the correlated region in each array. This may be the effects of entrainment of the lower-speed Nitrogen gas into the region of the higher-speed Helium gas, consistent with reports for this type of mixing layer [5].

A relevant metric of the correlation coefficient arrays is the value of the correlation peak. Figs. 53 and 54 show plots of the correlation peaks as a function of frame separation for flow locations greater than 1.25 cm. For flow locations greater than 7.5 cm, the peak is approximately 0.9 for 2 frames of separation, suggesting minimal evolution of the fluctuations over 2 ms. However, even the most highly-correlated regions in the flow degrade by over 30 percent in 4 ms, suggesting the limited extent of validity for frozen flow assumptions. Note that for the present velocity profile, a frozen flow limited to 4 frames of separation relates to a temporal range of 4 ms or a spatial range of approximately 1.8 cm. Hence, techniques which must assume frozen flow over many centimeters may have questionable validity for complex mixing layers.

*5.3.3 Time-resolved Wavefront Slope Measurements.* For each shadowgraph measurement, a simultaneous measurement of the wavefront slope was recorded using the Hartmann wavefront sensor (WFS). This section presents the statistical calculations which were performed on the reconstructed phase surfaces obtained from the slope measurements. The section begins with a description of the Hartmann WFS principle and the phase reconstruction technique. The Hartmann WFS utilized for the present experiments and the shearing interferometer WFS utilized for the experiments described in Chapters III and IV are func-

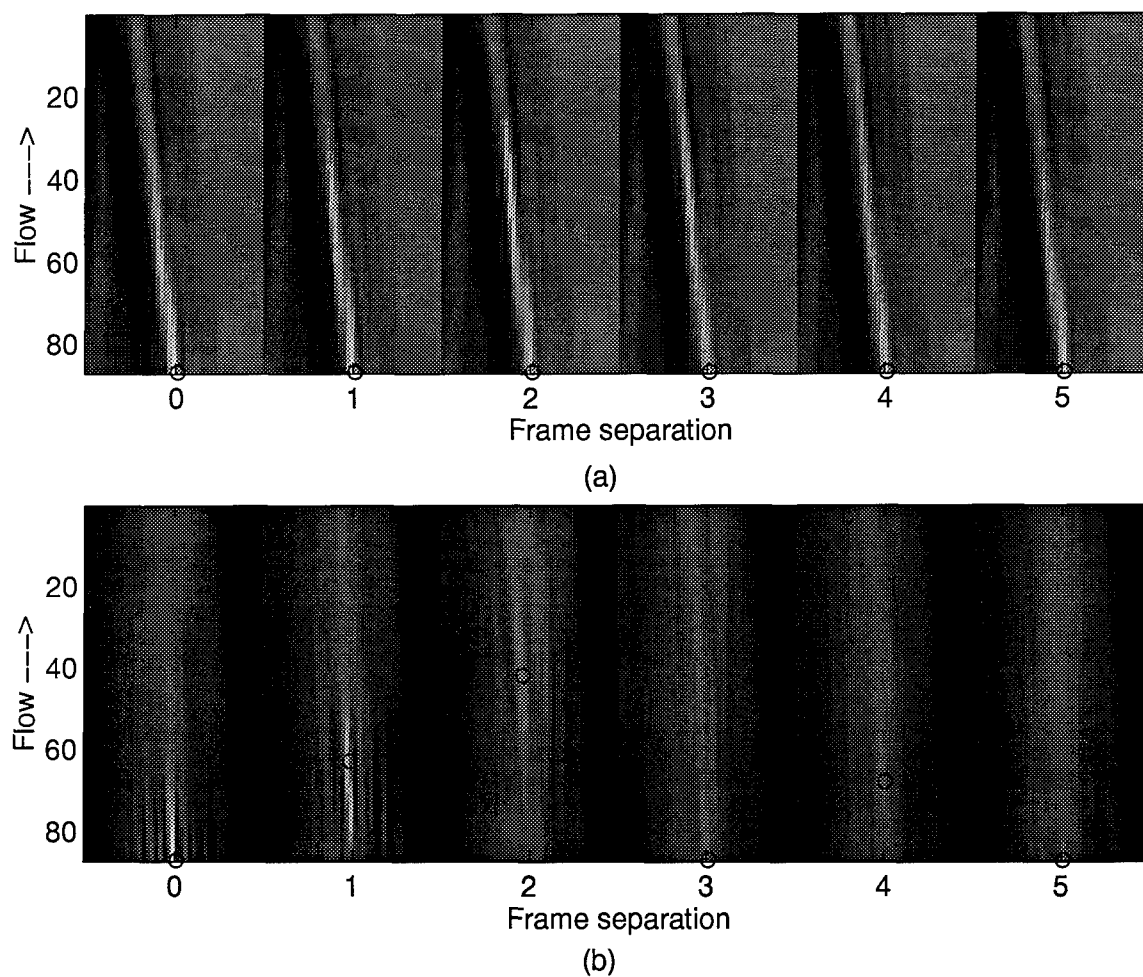


Figure 49. Correlation coefficient arrays computed on the shadowgraph images. Flow is upward. Aperture is centered at (a) 1.25 cm, and (b) 2.5 cm in the flow.



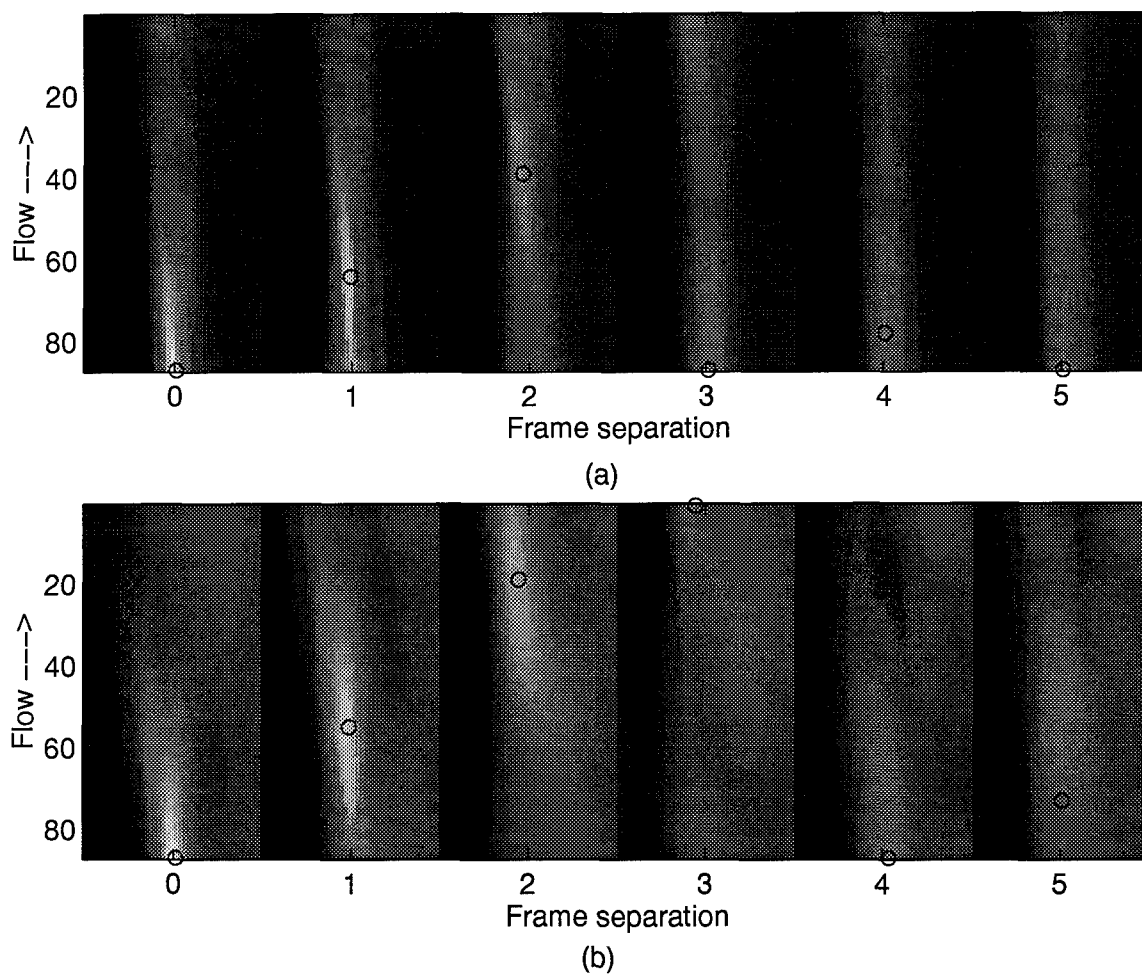


Figure 50. Correlation coefficient arrays computed on the shadowgraph images. Flow is upward. Aperture is centered at (a) 3.75 cm, and (b) 5.0 cm in the flow.

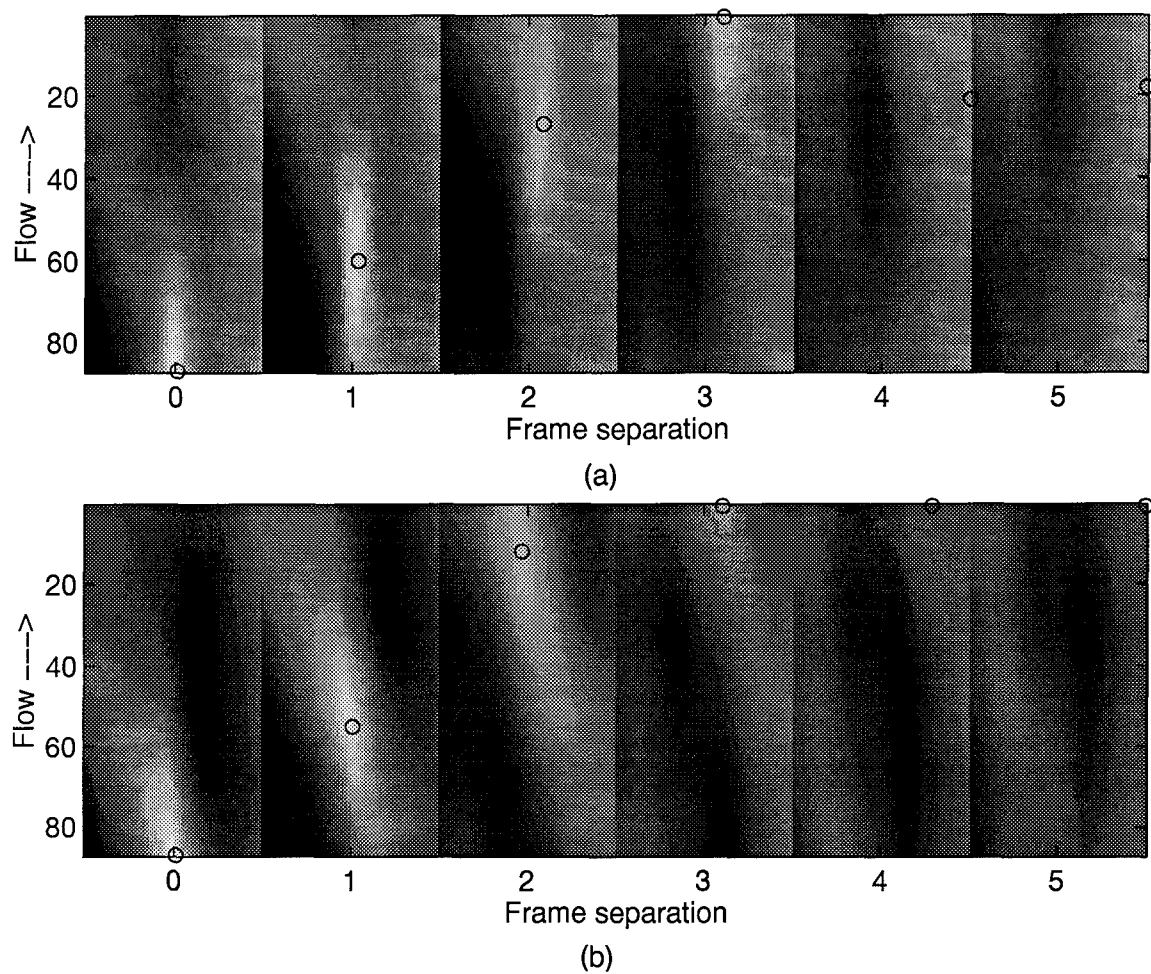


Figure 51. Correlation coefficient arrays computed on the shadowgraph images. Flow is upward. Aperture is centered at (a) 7.5 cm, and (b) 10.0 cm in the flow.

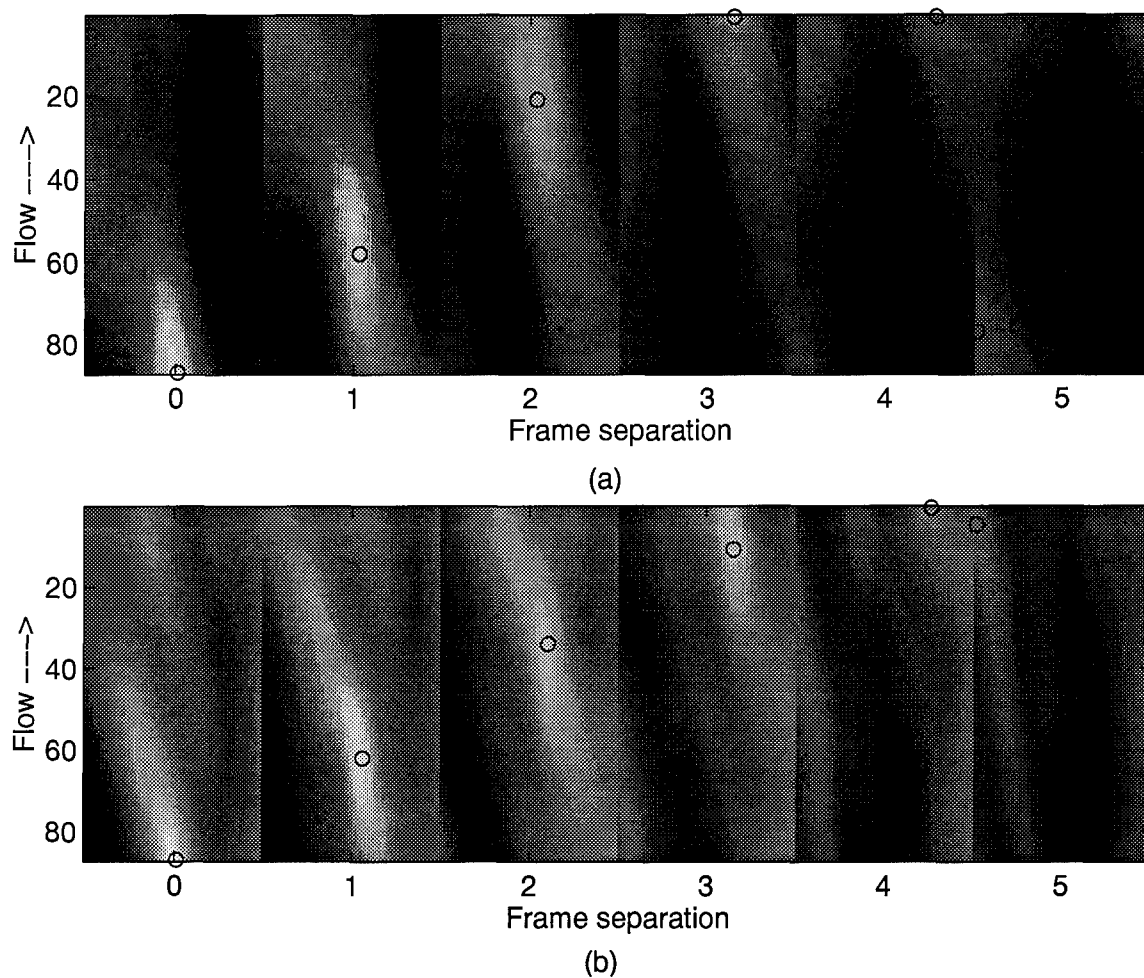


Figure 52. Correlation coefficient arrays computed on the shadowgraph images. Flow is upward. Aperture is centered at (a) 12.5 cm, and (b) 15.0 cm in the flow.

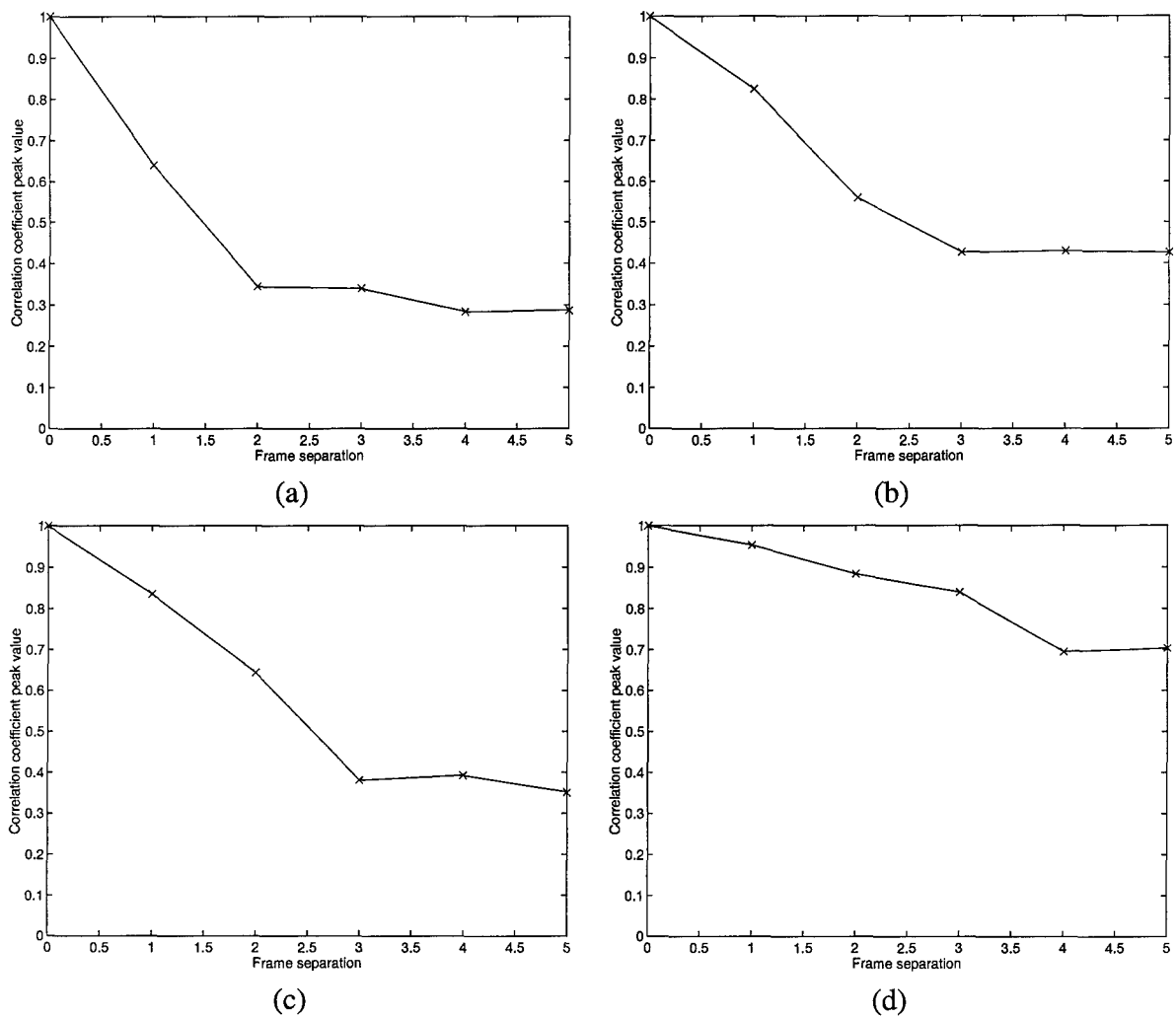
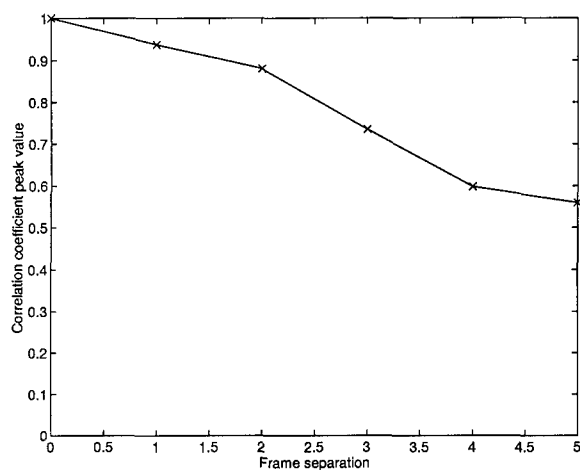
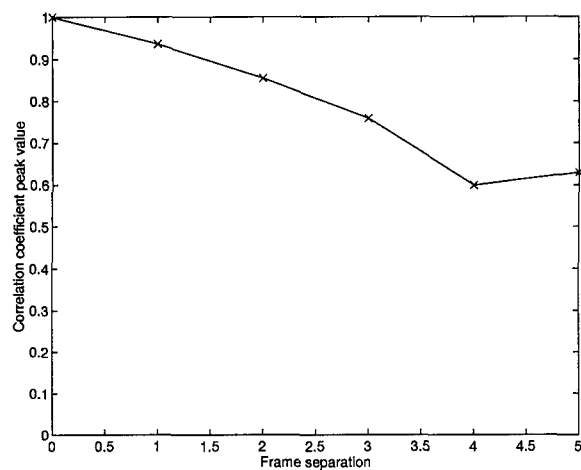


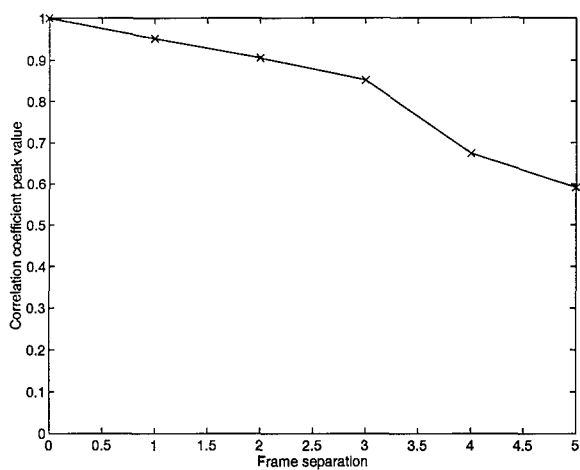
Figure 53. Peak values of the shadowgraph correlation coefficient arrays as a function of frame separation. Aperture is centered at (a) 2.5 cm, (b) 3.75 cm, (c) 5.0 cm, and (d) 7.5 cm in the flow.



(a)



(b)



(c)

Figure 54. Peak values of the shadowgraph correlation coefficient arrays as a function of frame separation. Aperture is centered at (a) 10.0 cm, (b) 12.5 cm, and (c) 15.0 cm in the flow.

tionally equivalent. Both sensors provide measurements of phase slopes across the wavefront. In weak turbulence the two have been shown to perform nearly identically [35], with the Hartmann WFS being slightly less susceptible to shot noise errors in strong turbulence. A detailed description of a performance comparison between the two sensors may be found in Pennington [34].

The physical arrangement of a section of a Hartmann WFS is shown in Fig. 55. A collimated laser beam is propagated through the turbulent region, illuminating a two-dimensional Hartmann sensor. The sensor consists of a two-dimensional array of lenslets coupled with a CCD-array of detectors. Incident light is focused onto the detectors by the lenslets. The slope of the local phase aberration incident on each lenslet causes the image formed to be displaced from the center of the focal plane. The centroid of each image is then computed to estimate the local slope,  $S_n$ , of the wavefront phase. The output of a single Hartmann sensor is related to the incident phase by [53]

$$S_n^\zeta = - \int_{-\infty}^{\infty} \int_{-\infty}^{\infty} W_n^\zeta(x, y) \phi(x, y) dx dy, \quad (48)$$

where  $S_n^\zeta$  is the slope output by the  $n^{th}$  subaperture in the  $\zeta$  direction, and  $\zeta$  indicates either the  $x$  or the  $y$  component of the slope. The function,  $W_n(x, y)$  is the normalized phase weighting function of the  $n^{th}$  lenslet, which is a constant function inside the subaperture and zero outside. The notation  $W_n^\zeta(x, y)$  indicates the  $\zeta$ -direction component of the gradient of  $W_n(x, y)$ . Note that the measurement of  $S_n^\zeta$  implies temporal integration; hence, the frozen flow hypothesis must be assumed in Eq.( 48). The temporal averaging for the slope measurements is identical to the averaging described for the shadowgraphs in Section 5.3.1; i.e., the flow is averaged over approximately one-fifth of the aperture. While this extent of temporal integration may be considered long, the shadowgraphs indicate that the frozen flow hypothesis may be reasonably valid over this extent.

The reconstructed phase,  $\phi_{meas}(x, y)$ , may be computed from the wavefront slope measurements by [39]

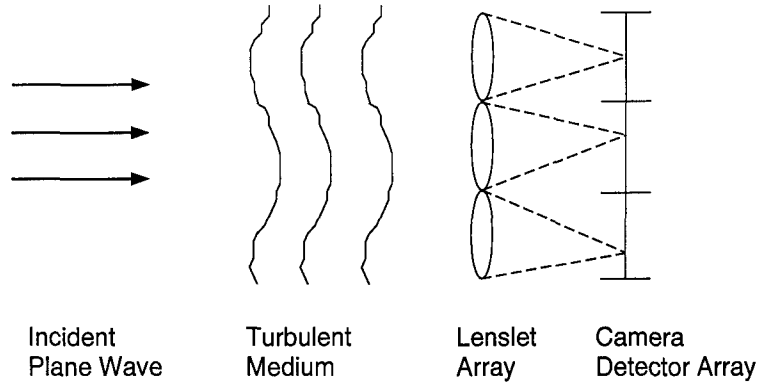


Figure 55. Hartmann WFS turbulence sensing system.

$$\phi_{meas}(x, y) = \sum_j c_j e_j(x, y), \quad (49)$$

where  $e_j(x, y)$  is the  $j^{th}$  elementary function used to estimate  $\phi_{meas}(x, y)$ , and  $c_j$  is the weight associated with that elementary function. The elementary functions were two-dimensional triangle functions [9], with base width equal to two times the subaperture side length, centered at the interior corners of the subapertures. For the present experiment, an array of  $11 \times 11$  elementary functions was used. The weights,  $c_j$ , are computed from the slope measurements using [39]

$$c_j = \sum_n M_{jn} S_n^\zeta, \quad (50)$$

where  $M_{jn}$  is the reconstruction matrix. The reconstruction matrix used for the present experiments is a least-squares reconstructor. A more detailed explanation of this procedure may be found in a paper by Roggemann *et al.* [39].

The reconstructed phase surfaces for the present experiments are bilinearly-interpolated,  $41 \times 41$  arrays, expressed in units of waves to be consistent with the phase surfaces presented from the shearing interferometer in the previous chapters. Additionally, the random phase was isolated as before by removing the deterministic imaging system effects as well as the average phase associated with the 255-sample ensemble. An example of a reconstructed

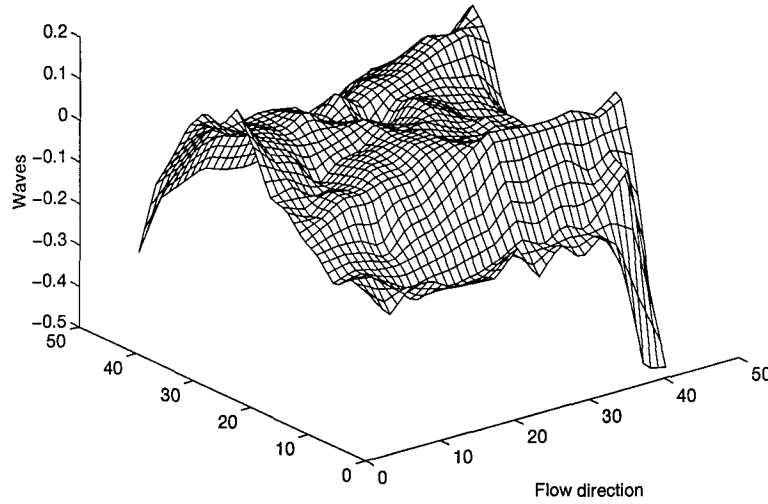


Figure 56. Reconstructed wavefront phase from the Hartmann WFS. Optical system effect and average phase have been removed. Flow is in the  $x$  direction. Propagation is in the  $z$  direction. Sample spacing in  $x$  and  $y$  is  $345 \mu\text{m}$ .

phase surface, where the system effects and average phase effects have been removed is shown in Fig. 56. This realization was obtained at 15 cm in the flow, simultaneously with the shadowgraph realization depicted in Fig. 44(a). Note the  $x$  and  $y$  units in Fig. 56 are samples. The sample spacing in both directions is approximately  $345 \mu\text{m}$ . In the next section these phase surfaces are evaluated for indications of frozen flow characteristics in a manner analogous to the shadowgraph assessment.

**5.3.4 Temporal Analysis of the Wavefront Phase.** This section presents the results of the correlation coefficient arrays given by Eq. (47), computed for the ensemble of wavefront phase measurements which were recorded simultaneously with the shadowgraphs. While the temporal resolution of these measurements is the same as the shadowgraphs, the spatial resolution is substantially less. The procedure is identical to the operation described in Section 5.3.2. A quantitative assessment of frozen flow is more relevant for phase measurements than shadowgraphs, given the role of frozen flow assumptions on adaptive optics. Here, a  $15 \times 15$  window was chosen for the  $41 \times 41$  phase surfaces. The window size was selected



empirically. Smaller windows resulted in poor correlations. The present window afforded the best indications of frozen flow.

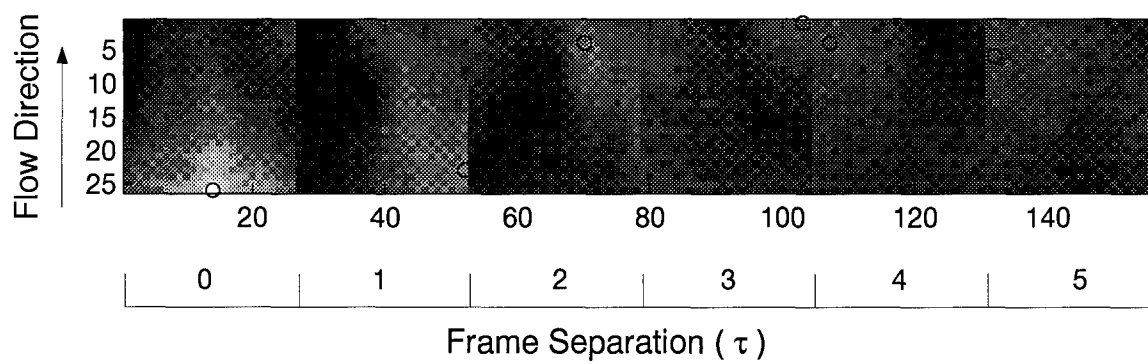
Figs. 57 through 60 are images of the coefficient arrays for frame separations between 0 and 5, and for the eight flow locations. As before, the peak coefficient in the array for each frame separation is designated by the symbol 'o'. As with the shadowgraphs, indications of frozen flow was found to be present for flow locations greater than 1.25 cm, over 2 to 4 frame separations.

The peak values of the correlation coefficient arrays were computed and are shown in Figs. 61 and 62 as a function of frame separation for flow locations greater than 1.25 cm. Here, even for the most highly-correlated regions in the flow (greater than 10 cm), the coefficients degrade by over 30 percent for a 1-frame separation, compared with 5 percent for the shadowgraphs. Thus, although the frames appear to be correlated when Figs. 61 and 62 are visually assessed, the large degradation in the peak values suggests significant evolution of the density fluctuations over sub-millisecond time scales.

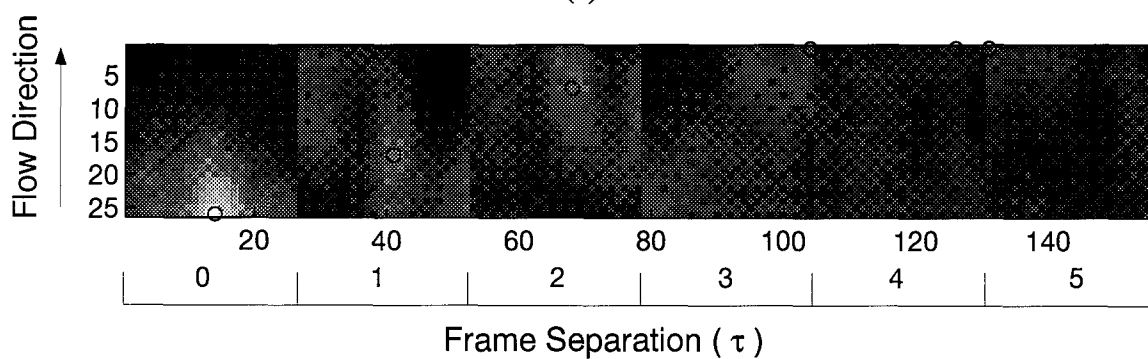
An additional parameter of interest which is readily available from the correlation arrays is an estimate of the velocity of the correlation peaks. The velocities may be estimated, based on the frame rate, aperture size, and pixel separation of the peaks. This estimate may be used to approximate the convection velocity of the turbulent structures. The average velocity of the phase correlation peaks over three frames was computed and is shown in Fig. 63 as a function of flow location. A velocity estimate at 1.25 cm was omitted due to the inconclusive correlations at that location.

#### *5.4 Simultaneous Wavefront Slope and PSF Measurements*

This section presents the results from the simultaneous realizations of wavefront slopes and PSF's for eight beam locations in the turbulent mixing layer. The full data set consisted of 255 frame-registered images for each flow location, for a total of 4096 images, excluding flat field, dark frame, and reference measurements. For all images reported in this

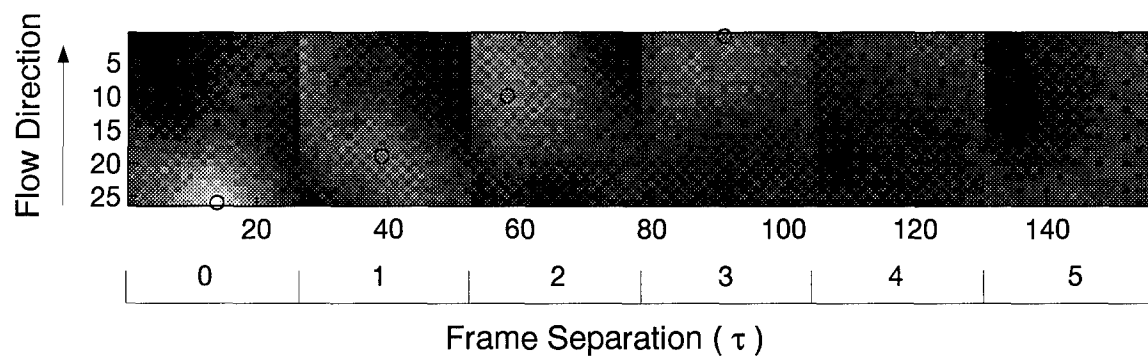


(a)

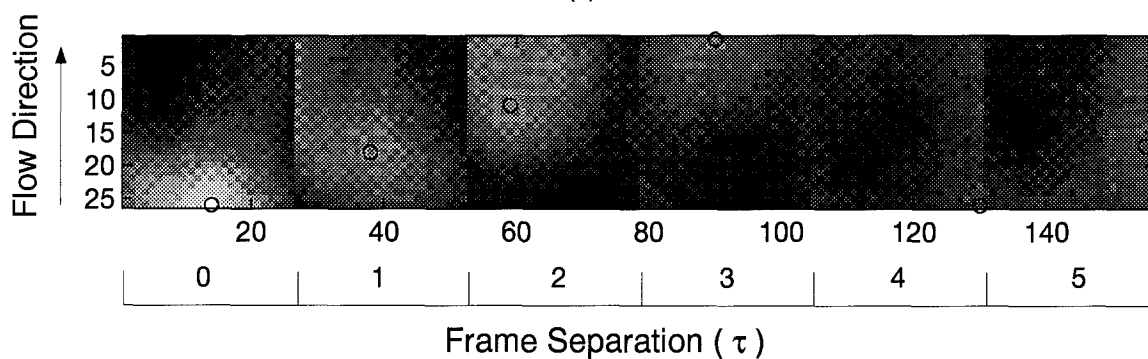


(b)

Figure 57. Correlation coefficient arrays computed on the phase surfaces. Flow is upward. Aperture is centered at (a) 1.25 cm, and (b) 2.5 cm in the flow.

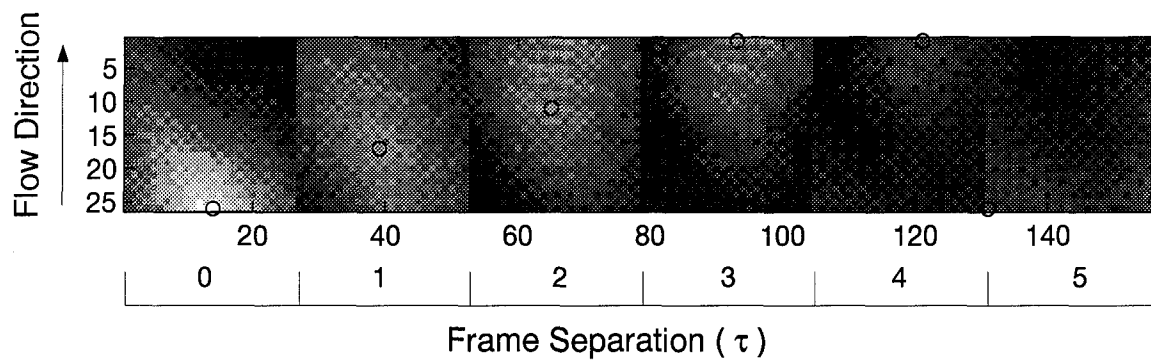


(a)

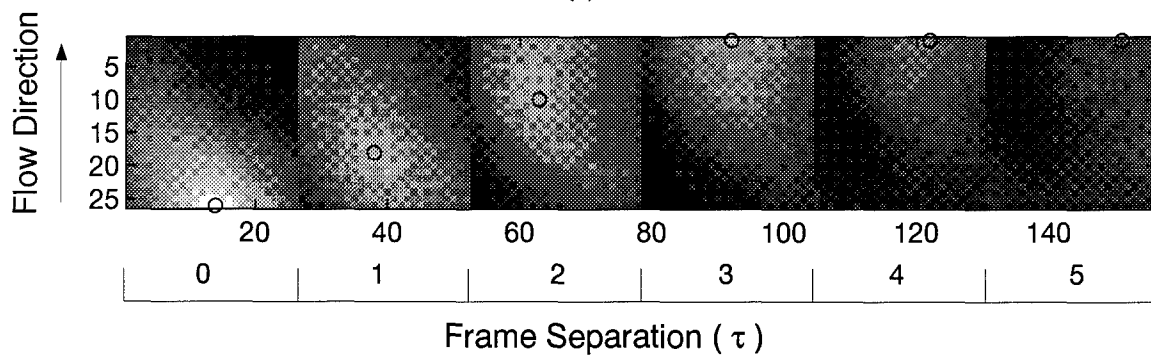


(b)

Figure 58. Correlation coefficient arrays computed on the phase surfaces. Flow is upward. Aperture is centered at (a) 3.75 cm, and (b) 5.0 cm in the flow.

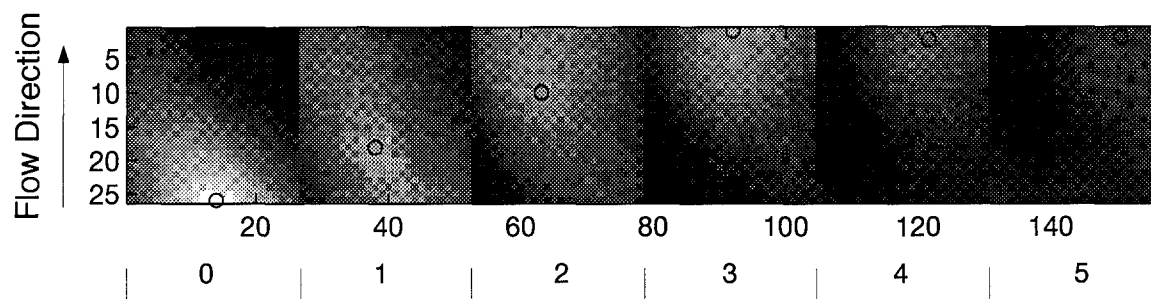


(a)



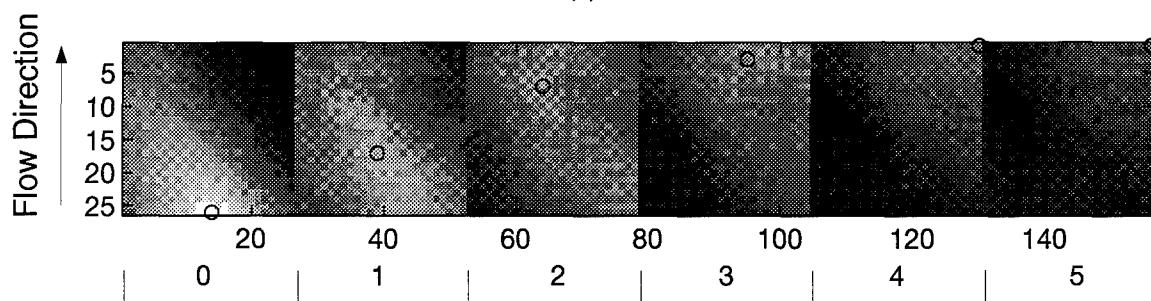
(b)

Figure 59. Correlation coefficient arrays computed on the phase surfaces. Flow is upward. Aperture is centered at (a) 7.5 cm, and (b) 10.0 cm in the flow.



Frame Separation ( $\tau$ )

(a)



Frame Separation ( $\tau$ )

(b)

Figure 60. Correlation coefficient arrays computed on the phase surfaces. Flow is upward. Aperture is centered at (a) 12.5 cm, and (b) 15.0 cm in the flow.

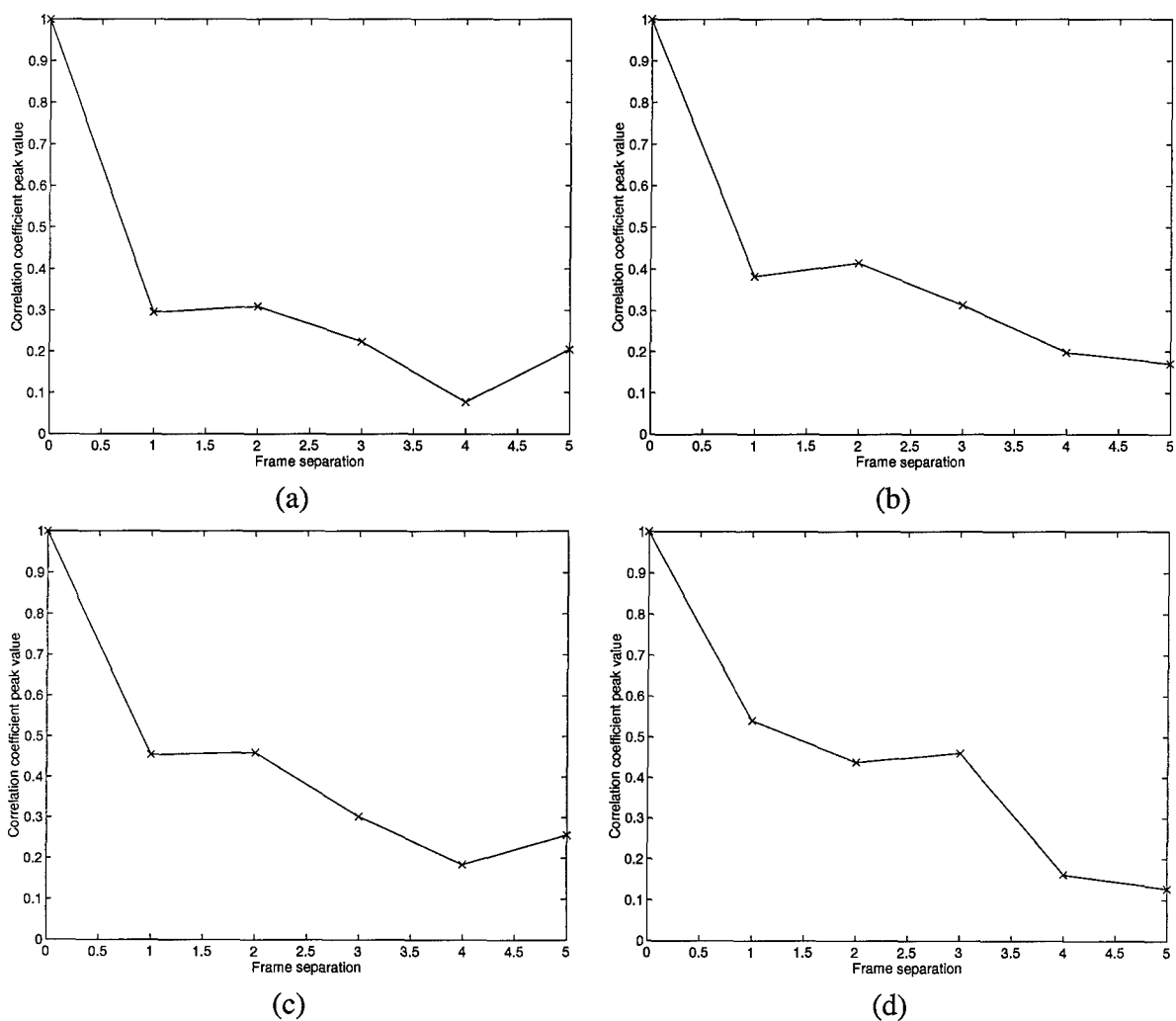
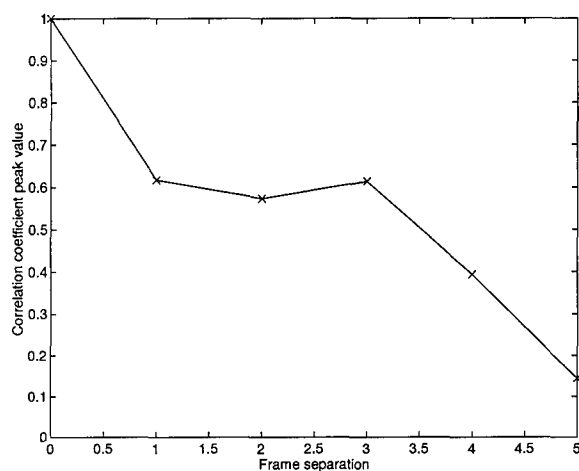
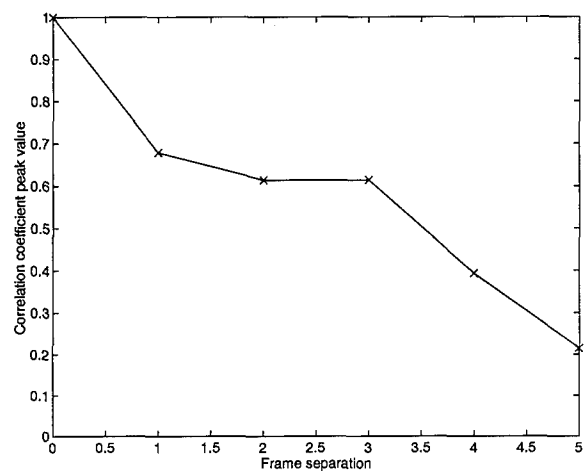


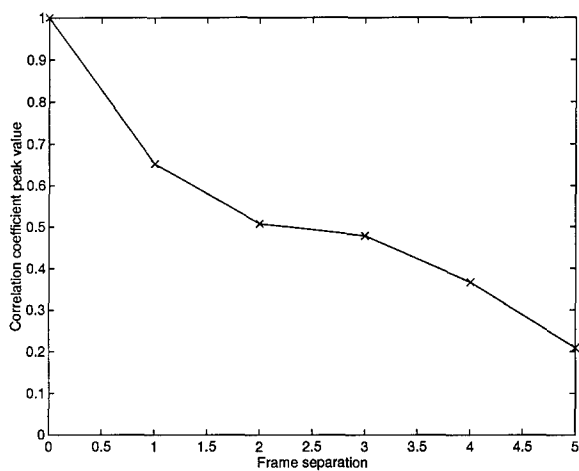
Figure 61. Peak values of the phase correlation coefficient arrays as a function of frame separation. Aperture is centered at (a) 2.5 cm, (b) 3.75 cm, (c) 5.0 cm, and (d) 7.5 cm in the flow.



(a)



(b)



(c)

Figure 62. Peak values of the phase correlation coefficient arrays as a function of frame separation. Aperture is centered at (a) 10.0 cm, (b) 12.5 cm, and (c) 15.0 cm in the flow.

section, dark frame and flat field calibrations have been performed [42]. Statistical calculations reported in this section are with regard to the spatial properties of the phase fluctuations.

*5.4.1 Phase Structure Function Calculations.* In this section phase structure functions are reported for the eight aperture locations in the mixing layer. The structure function was computed using a procedure analogous to the that described in Chapter III for the free turbulence and Chapter IV for the channel flow turbulence. Recall these mixing layers were shown to be nonhomogeneous for the statistical ACF with an orthogonal orientation of the turbulence generator. It's anticipated that the present orientation, consisting of much stronger density gradients in the mixing region, are similarly nonhomogeneous; hence, the ACF calculation was not repeated. The present experiment had two important distinctions from the two previous experiments with regard to statistical calculations. First, the present orientation of the mixing layer introduced strong density gradients in the local mixing region and negligible density gradients elsewhere. This was particularly significant for flow locations greater than 10 cm; i.e., where the mixing width was still growing. The second distinction was in the frame rate of the realizations. As shown in the two previous sections, the samples are correlated for 2 to 3 frames; hence, the realizations are not independent, although the larger data set (255 frames) provides increased confidence.

To compute the phase structure function using Eq. (14) for 255 realizations, a grid of 16 anchor points was defined on the  $41 \times 41$  phase surfaces. Fig. 64 shows an example of one phase realization, displayed as a surface contour with an overlay of the 16 anchor points, where the  $x$  and  $y$  spacing between each anchor point is three samples.

An estimate of the phase structure function was obtained using Eq. (38) for  $\Delta x$  and  $\Delta y$  on an interval of  $-5$  samples to  $+5$  samples. Figs. 65 and 66 show the structure function for eight representative anchor points for the aperture centered at 15 cm.

For the random process  $\phi'(x, y)$  to be stationary in first increments, all anchor points must exhibit approximately the same structure function. From the eight-sample set shown in Figs. 65 and 66, it may be seen that the anchor points exhibit similar, though not equivalent,



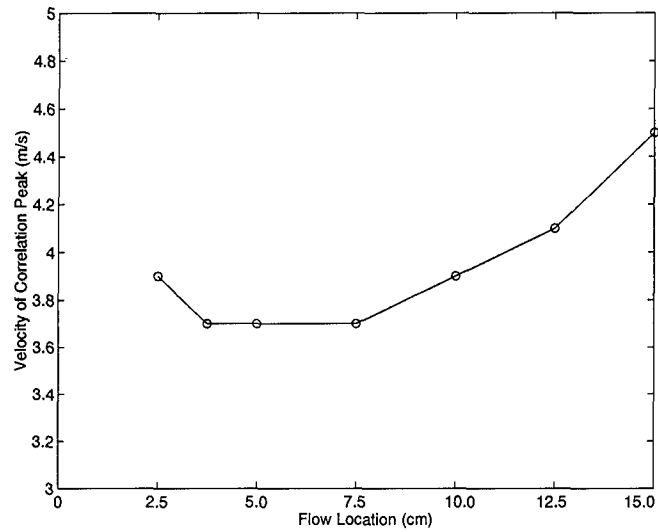


Figure 63. Velocity estimate of the phase correlation peaks as a function of flow location. Velocity estimate at 1.25 cm was omitted due to the inconclusive correlations at that location.

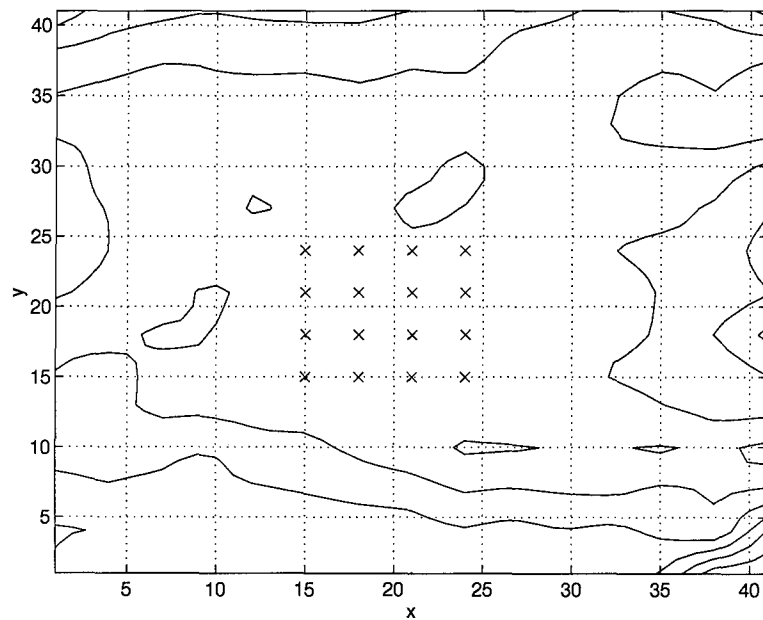


Figure 64. Surface contour of one phase realization,  $\phi'(x, y)$ , with overlay of 16 anchor points. Each 'x' indicates an anchor point. Sample spacing in  $x$  and  $y$  is  $345 \mu\text{m}$ . Spacing between each anchor point is three samples.

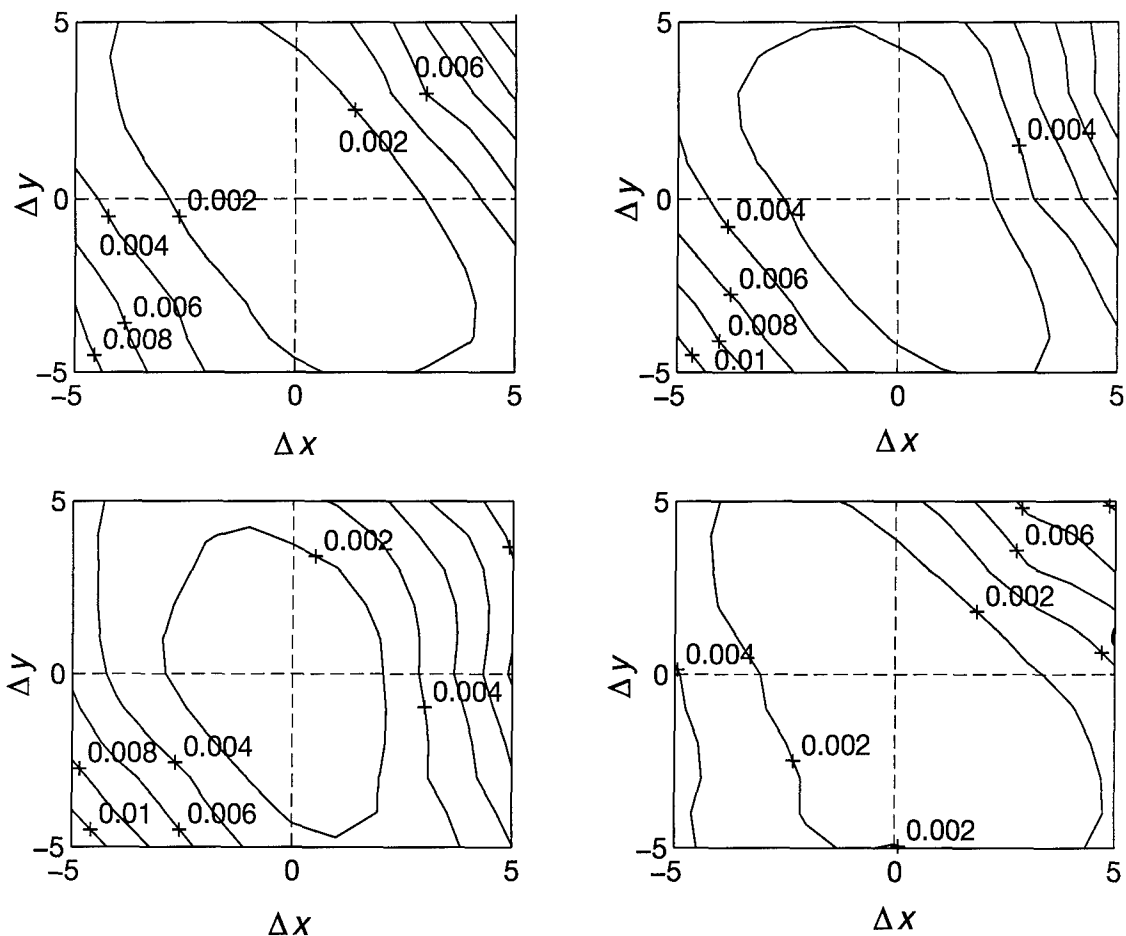


Figure 65. Surface contour of the structure function for four representative anchor points from the sample grid. Aperture is centered at 15 cm. Contour units are waves<sup>2</sup>. Each unit of  $\Delta x$  and  $\Delta y$  is 345  $\mu\text{m}$ .

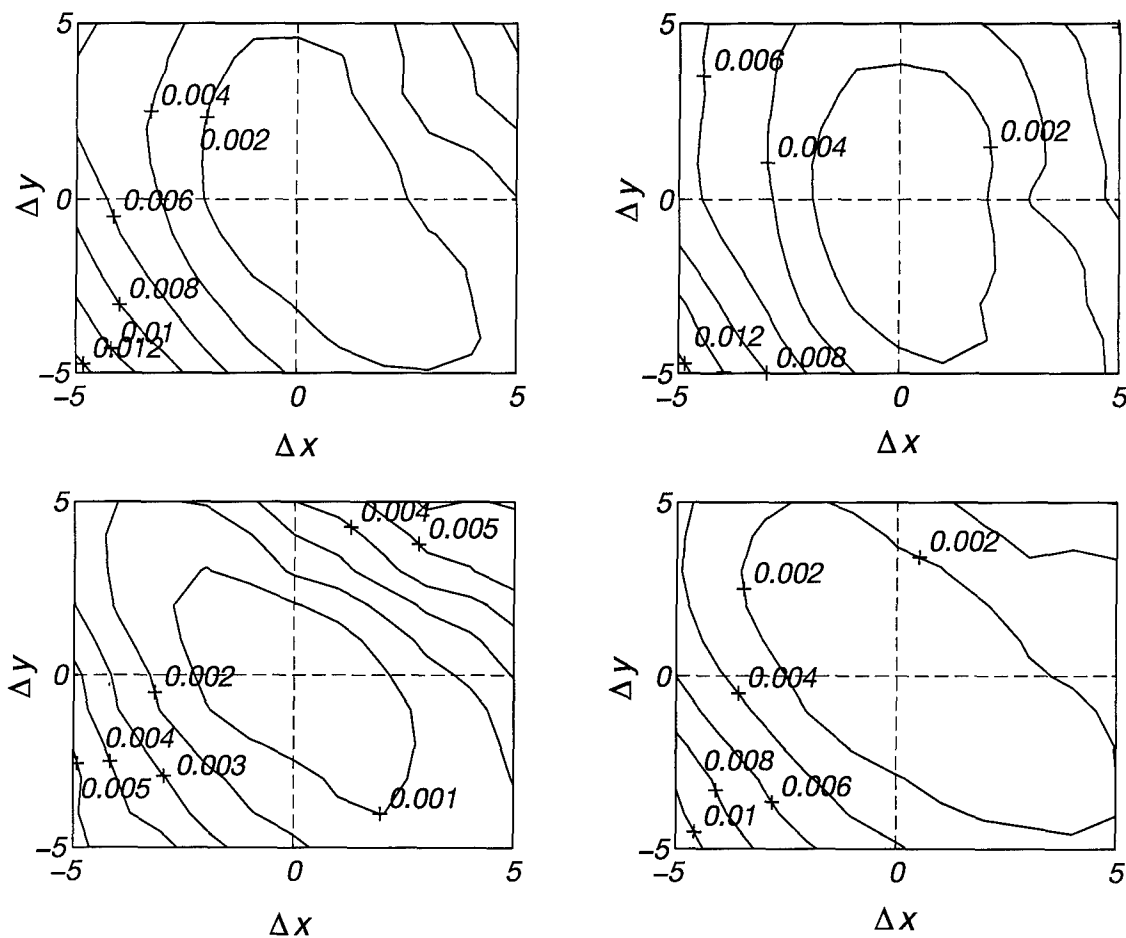


Figure 66. Surface contour of the structure function for four representative anchor points from the sample grid. Aperture is centered at 15 cm. Contour units are waves<sup>2</sup>. Each unit of  $\Delta x$  and  $\Delta y$  is 345  $\mu\text{m}$ .

contours; thus, an average of these points would not appropriately represent the region. In general, the shapes of the contours shown in Figs. 65 and 66 are representative of the contour shapes observed for flow locations greater than 10 cm. For regions closer to the exit nozzle of the turbulence generator, the contours varied significantly for each anchor point. For example, Fig. 67 shows the structure function for four representative anchor points where the aperture is centered at 10 cm. Note that in the region of 10 cm, the mixing layer reaches the width of the channel; hence, it is not surprising that the statistics are nonhomogeneous for locations closer to the exit nozzle. The 'trend towards homogeneity' observed beyond 10 cm for full-channel flow implies that statistical models such as those developed in Chapter IV may be appropriate farther downstream.

In summary, the lack of homogeneity prohibited modeling the channel flow in the present orientation as a Kolmogorov turbulence. Nevertheless, it was of interest to determine the effects of 'forcing' the model on the average structure function data to see the effects of invoking homogeneity assumptions inappropriately. Therefore, coherence dimensions,  $x_0$  and  $y_0$ , were estimated from the average structure functions for each flow location. For the  $x$ -component, the  $r^{5/3}$  functional fit was poor beyond 2 to 3 sample spacings for flow locations between 1.25 cm and 7.5 cm. For flow locations greater than 10 cm, the functional fit was somewhat better. For the  $y$ -component, the  $r^{5/3}$  power law followed the data reasonably well for all locations. The coherence dimensions were then used to approximate the structure function model, using

$$\tilde{D}_\phi(\Delta x, \Delta y) \approx 6.88 \left\{ \left( \frac{\Delta x}{x_0} \right)^2 + \left( \frac{\Delta y}{y_0} \right)^2 \right\}^{5/6}, \quad (51)$$

the familiar five-thirds power law representation for Kolmogorov-like, anisotropic flow. In the next section, a Strehl ratio computed from this model will be compared to measurements.

**5.4.2 Measurements of Strehl Ratio.** In this section a Strehl Ratio (SR) is reported for the eight aperture locations in the mixing layer. The SR is relative because the diffraction-limited PSF in the denominator of Eq. (19) was replaced with the PSF of the imaging system

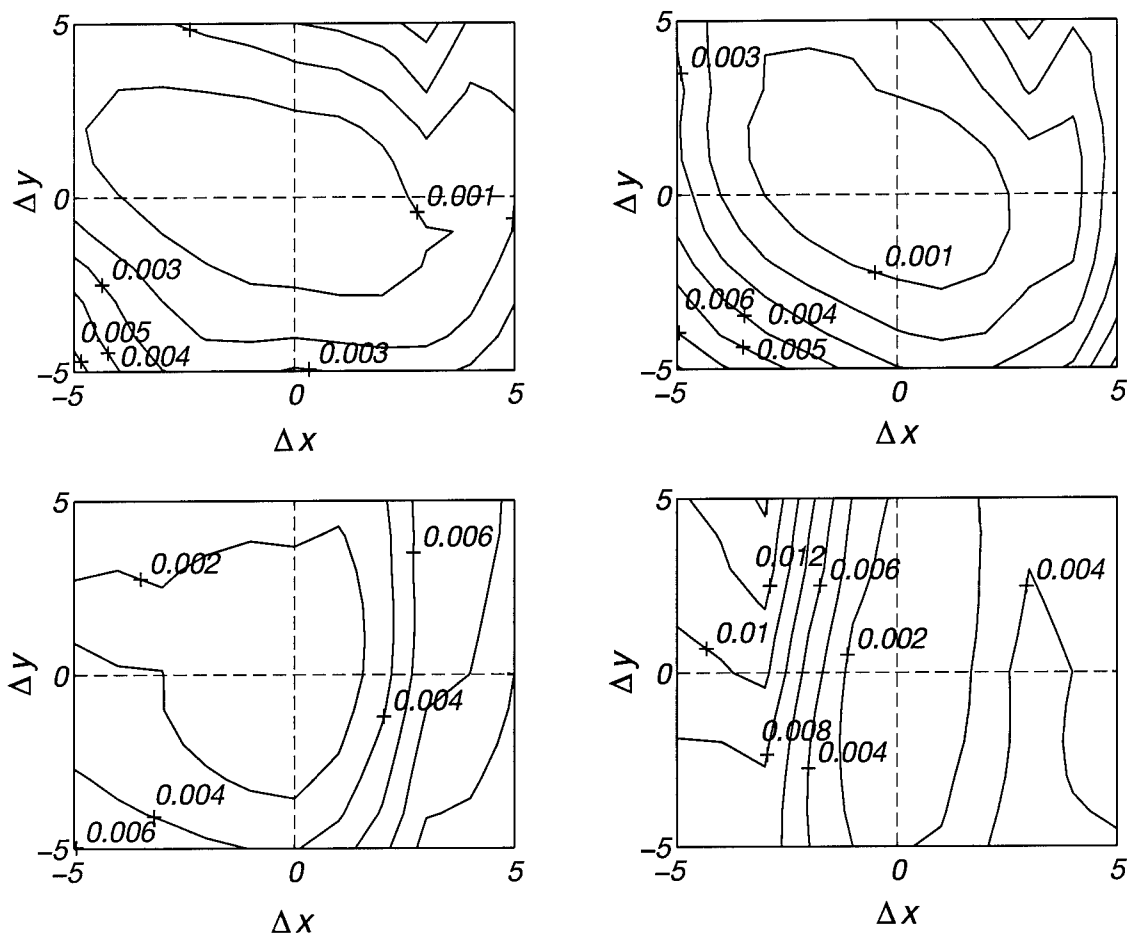


Figure 67. Surface contour of the structure function for four representative anchor points from the sample grid. Aperture is centered at 10 cm in the flow. Contour units are waves<sup>2</sup>. Each unit of  $\Delta x$  and  $\Delta y$  is 345  $\mu\text{m}$ .

in the absence of turbulence (the reference PSF), a measurable quantity. Replacing the formal Strehl definition with a relative measure of image degradation is not unusual in analysis of optical systems [7, 50]. Furthermore, this relative measure allows direct comparison with the phase-variance-based model, which is also relative. For completeness, an 'absolute' SR was estimated to quantify the optical degradation induced by the imaging system. The estimate was obtained from Eq. (20), where the integrals were replaced with finite, two-dimensional summations. The numerator for Eq. (20) was the normalized system OTF, computed from Eq. (18) for the reference PSF. The denominator for Eq. (20) was a normalized autocorrelation of a zero-phase pupil function [13], where the pupil function geometry may be obtained directly from a camera image. Using this procedure, the absolute SR was approximately 0.2.

The SR was computed from the average of an ensemble of PSF measurements, analogous to the procedure described in Chapter IV. For each flow location, a reference PSF was recorded along with 255 realizations of the perturbed PSF in the presence of the turbulence. The perturbed PSF measurements were averaged, and the SR was computed using Eq. (19). The resulting SR for the eight locations is shown in Fig. 68.

Accompanying the SR derived from PSF measurements, is the relative SR computed from the structure function model given in Eq. (51). The relative measure was obtained by including the system reference phase in  $\mathcal{H}_0$  for Eq. (16). The structure function model tends to underpredict the optical degradation with respect to experiment; however, it consistently follows the measured curve for all locations in the flow. The fact that the structure function model does not agree with experiment is a consequence of forcing the homogeneity assumption for the mixing layer in the present orientation. Hence, the model fails in a manner similar to the aero-optical model. Finally, the theoretical model given in Eq. (22) is displayed. This is a poor predictor of optical degradation, due to its functional form which predicts the same degradation independent of the flow orientation.

Some interesting observations may be made from Fig. 68, with the assistance of the flow visualization images in Figs. 36 and 37. Note that the maximum value for the SR is approximately 0.4, occurring at the exit nozzle of the turbulence generator. For the orthog-

onal orientation of the mixing layer, presented in Chapter IV, this region was shown to be approximately laminar, with a Strehl ratio of 0.9. The degradation in the present experiment is attributed to the large density gradients at the He/N<sub>2</sub> interface. The SR displays a rapid degradation through 3.75 cm. This region is associated with the transition of the mixing layer from a laminar to turbulent flow. The SR then continues to degrade at a slower rate over the region between 3.75 cm and 10 cm, a region characterized by a spreading of the mixing layer within the channel, as can be seen in the flow visualization images. Note from Fig. 68 that the SR reaches a minimum in the region of 10 cm, which corresponds to the location where the width of the mixing layer was predicted to reach the channel width. Recall from Chapter IV, the prediction for  $\delta(x)$  for velocity profile 1 was based on an estimate of the mixing coefficient,  $C_\delta$ , obtained from the crossover of the structure function coherence parameters, and further validated by the flow visualization series. The flow visualization images supported the theory that the value for  $C_\delta$  obtained from profile 2 could be applied to profiles 1 and 3. The SR minimum in Fig. 68 further supports that theory. Beyond 10 cm the SR increases, indicative of improved seeing conditions and consistent with the concept of the dissipation of the small-scale structures in a fully-developed flow.

### 5.5 *Summary of Time-resolved Measurements in Channel Flow*

Two high-speed cameras were used to generate a large set of measurements of laser light propagating through a high-Reynolds-number mixing layer. A channel-flow mix of Helium gas at 4.5 m/sec and Nitrogen gas at 1.0 m/sec induced optical perturbations which were sensed using shadowgraph, wavefront slope, and point spread function measurements. The wavefront slopes were used to reconstruct phase surfaces. The mixing layer was oriented such that the laser propagation direction was parallel to the plane of the mixing layer. An ensemble of 255 measurements were obtained for each sensing technique at eight aperture locations in the flow, spaced between 0 cm and 15 cm from the exit nozzle of the turbulence generator. Shadowgraphs and wavefront slopes were recorded simultaneously, providing

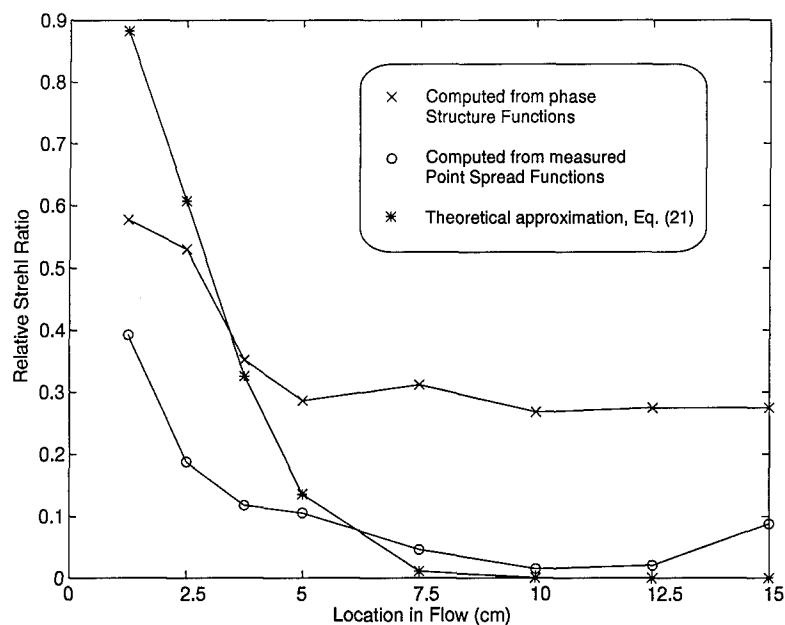


Figure 68. Relative Strehl ratio calculation as a function of downstream location.

frame-registered views of the flow. Additionally, point spread functions and wavefront slopes were recorded simultaneously in a second experiment.

A technique was introduced which computes an array of correlation coefficients over a two-dimensional sliding window for various temporal separations. For the shadowgraphs, reasonable correlations were obtained for a maximum separation of 4 frames, equivalent to 4 ms. For the velocity profiles used in these experiments, this result implies the frozen flow assumption is valid only within a spatial extent of approximately 2 cm. The correlation coefficient arrays which were computed from the wavefront slopes exhibited similar correlation properties; however, the peaks of the arrays degraded by 30 to 60 percent for 1-frame separation.

Structure functions were computed on sets of phase surfaces for the eight locations in the flow. The structure functions indicated the phase fluctuations were not homogeneous for any of the locations, the worst case being in the flow region less than 10 cm, where the mixing layer width had not reached the width of the channel.



Strehl ratios were computed using the average point spread functions for the eight locations in the flow. The maximum SR obtained was 0.4, occurring at the exit nozzle of the turbulence generator. For the orthogonal orientation of the mixing layer, this region was shown to be approximately laminar, with a SR of 0.9. The SR was minimum at 10 cm, consistent with the prediction for the maximization of the mixing layer width. Two additional Strehl ratios were computed. The first was from a structure function model which was forced on the nonhomogeneous data. This prediction model underestimated the optical degradation consistently across the flow. The second Strehl ratio was a theoretical model which provided a poor prediction of the optical effects for this flow orientation.

## VI. CONCLUSIONS AND RECOMMENDATIONS

### 6.1 Overview

This research investigated the effects of light propagation in an aero-optical environment via experimental measurements of turbulent mixing layers in an optical laboratory. A shear layer mix of Helium and Nitrogen gas provided the complex flow field to evaluate the spatial and temporal density fluctuations in a high-Reynolds-number flow. The mixing layer was generated in two experimental configurations. The first configuration explored the dynamics of a free turbulent mixing layer; i.e., one that was discharged into the ambient air. For the free turbulence experiment, the Reynolds number was  $4.4 \times 10^3 \text{ cm}^{-1}$ . The second configuration explored the dynamics of the mixing layer discharged into a rectangular channel. For this configuration the Reynolds number was  $4.4 \times 10^3 \text{ cm}^{-1}$  for one set of experiments and  $2.2 \times 10^3 \text{ cm}^{-1}$  for another.

The turbulent mixing layer was sensed optically; thus, all measurements were non-intrusive. The density fluctuations were treated as a random process, where no a priori assumptions were made on statistical stationarity in the flow. Instead, the fluctuations were tested over various locations in the flow for evidence of homogeneity or isotropy. This was accomplished by computing spatial autocorrelation functions and structure functions on large ensembles of two-dimensional optical phase measurements of laser light after propagating through the mixing layer. Additionally, temporal correlation functions were computed on time-resolved images to assess the validity of Taylor's frozen flow hypothesis on the experimental data.

### 6.2 Conclusions

For the free turbulence experiments, phase measurements were obtained using a 60 Hz lateral shearing interferometer. The phase autocorrelation function indicated the random phase fluctuations were not wide-sense stationary, when the turbulence was sensed in an orientation where the laser propagated orthogonal to the plane of the mixing layer. Thus, application

of classical aero-optical models, which assume statistical homogeneity were determined to be inappropriate. The phase structure function indicated the random phase fluctuations were stationary in first increments, though not isotropic. Hence, a direct application of a Kolmogorov five-thirds power law was not appropriate. However, an analogous five-thirds power law was developed for the streamwise and cross-stream indices separately. One-dimensional coherence parameters were introduced, analogous to the Fried atmospheric parameter,  $r_0$ , for Kolmogorov turbulence. The parameters provided a measure of the anisotropy in the flow. Relative Strehl ratios, computed from the phase structure functions, were reported and compared with two aero-optical estimations based on on-axis phase variance and mixing layer width. The aero-optical models, which assume homogeneity, overestimated the optical degradation by orders of magnitude compared to the structure functions. These results suggest the potential for developing novel prediction models for complex flows such as free turbulent mixing layers.

For the channel flow measurements, where the Reynolds number was  $4.4 \times 10^3$   $\text{cm}^{-1}$ , phase measurements were obtained using a lateral shearing interferometer, and frame-registered point spread functions were recorded. The turbulence was sensed in the same orientation as the free turbulence. The phase autocorrelation function again indicated the phase fluctuations were not wide-sense stationary. Therefore, as with the free turbulence measurements, the channel flow could not be appropriately modeled using the aero-optical equations. The structure function indicated the random phase fluctuations were stationary in first increments, and coherence parameters were developed for this flow configuration, analogous to the free turbulence. A plot of the coherence parameters versus location in the flow revealed a local region of isotropy in the flow region coincident with a maximization of the mixing layer width in the channel. The region was characterized by a cross-over of the streamwise and cross stream coherence parameters, leading to a derivation of a mixing coefficient for predicting the growth of the mixing layer width. The prediction was shown to be in excellent agreement with flow visualization images.

Four independent, relative Strehl ratios were computed using the average point spread functions, average structure functions, on-axis phase variance, and estimation of the mixing layer width. The latter two calculations assumed wide-sense stationarity and provided poor estimates of the optical degradation beyond a few centimeters of the mixing, when compared to the point spread function measurements. The structure function model provided an accurate Strehl ratio estimate throughout the flow.

A second set of channel flow measurements was reported, where the Reynolds number was  $2.2 \times 10^3 \text{ cm}^{-1}$ , and the turbulence was sensed in an orientation where the laser propagated parallel to the plane of the mixing layer. Phase measurements were obtained using a 1 kHz Hartmann wavefront sensor, while a second camera recorded either frame-registered shadowgraphs or frame-registered point spread functions. A technique was introduced which computed an array of correlation coefficients over a two-dimensional sliding window for various temporal separations. For the velocity profiles used in these experiments, a frozen flow assumption was found to be valid only within a spatial extent of one to two centimeters.

Phase structure functions indicated the phase fluctuations were not homogeneous when viewed from the mixing layer orientation for these experiments. The lack of homogeneity precluded the development of a structure function based model. Relative Strehl ratios were reported using the average point spread functions. The maximum SR obtained was 0.4, occurring at the exit nozzle of the turbulence generator. For the orthogonal orientation of the mixing layer, this region was shown to be approximately laminar, with a relative SR of 0.9. The SR was minimum at 10 cm. This minimum was in excellent agreement with a prediction based on the structure function model developed from the first set of channel flow measurements.

### *6.3 Recommendations*

This research was a natural progression in the evolution of a series of research efforts at the Air Force Institute of Technology to better understand and model the effects of turbulence on optical transmission. Although this research generated and analyzed over

20,000 images, this is considered a small sample of the turbulence profiles which could be further explored.

For the measurements recorded in Chapter V, the gas velocities were reduced to accommodate the longer integration times of the EG&G cameras. A worthwhile experiment would be a similar set of measurements with substantially higher gas velocities. This experiment would necessitate an optical shutter in the laser path in order to minimize the averaging effects of the detectors. Current optical shutters can operate at 10 kHz with shutter times of 0.1 ms or less. This device would permit a 10-fold increase in mean stream velocity with the same averaging effects as that noted in Chapter V.

This research conducted in-depth analyses of mixing layers with two velocity profiles resulting in Reynolds numbers of  $4444 \text{ cm}^{-1}$  and  $2222 \text{ cm}^{-1}$ , and an additional set of flow visualization images for a Reynolds number of  $8888 \text{ cm}^{-1}$ . An interesting model could be developed by computing structure function coherence parameters for mixing layers as a function of the Reynolds number. For example, with equivalent mixing layer growth functions, it would be interesting to see if the crossover of the  $x_0$  and  $y_0$  parameters, identified in Chapter IV, occurred predictably for each velocity profile. One dividend from such a large experimental campaign could be an analytical relationship between, for example, the optical transfer function of the turbulent flow for a given Reynolds number. At this time, however, it's not clear that the structure function is homogeneous for substantially higher Reynolds numbers.

Another useful set of experiments would be obtaining three-dimensional tomography of the mixing layer. The present optical bench can easily accommodate a radial series of optical paths through a free-flowing mixing layer for measurements on a set of Hartmann wavefront sensors. A more interesting measurement would likely be in a confined flow, but this would require fabrication of a transmissive pipe of sufficient optical quality. The present research has already solved the challenge of achieving frame synchronization of the high-speed cameras.

Finally, the thrust of this research has been loosely coupled to developing a more reliable model for aero-optical turbulence. This research has introduced a prediction model for optical

degradation in laboratory-generated mixing layers, which makes no a priori assumptions of isotropy or homogeneity. The analogy between mixing layers of dissimilar gases and the aero-optical environment appears to be understood [2]; however, development of structure function models on data from a true aerodynamic flow could be of considerable interest.

## *Appendix A. Data files for shearing interferometer*

This Appendix provides a complete set of tables corresponding to the data collected during this research on the shearing interferometer and point spread function camera, where applicable. The free turbulence and channel turbulence measurements described in Chapters III and IV follow the same numbering convention. Data groups are UNIX directories which contain a set of images, and are numbered XXXP. When the frame grabber for the shearing interferometer (SI) is activated, an image is acquired simultaneously from seven cameras: three from the x-leg of the SI, three from the y-leg of the SI, and one from the PSF camera. For both experiments described in Chapters III and IV the frame grabber was programmed to capture four images for each group, the maximum capable for the buffer. The frame capture sequence is numbered 0, 2, 4, 6. The specific cameras are numbered 00, 01, 02 for the x-leg; 10, 11, 12 for the y-leg; and 13 for the PSF camera. For example, a file called 2.01 refers to the second frame in the group for the second camera in the x-leg.

The ensemble size for one beam location in the flow was 160 realizations. This requires 20 data groups. A reference is also recorded. The reference was obtained by averaging eight realizations within a dedicated data group. Thus, for the experiments described in Chapter III, six beam locations were analyzed, requiring a total of  $6 \times 21$  or 126 data groups and  $7056 \times 512 \times 484$  images.

The reconstructed phase surfaces, with deterministic system effects subtracted are labeled dphi-1 to dphi-160 within each corresponding beam location. The PSF is labeled similarly. The two tables which follow identify an 8 mm tape number and the experimental data which it contains, given by data group numbers.

Table 3. Free Turbulence Experiments - Data Files

Tape Number	Flow Location (cm)	File Name	Comments
1	1.25	358P-377P	ref 317P; no PSF
2	5.75	213P-232P	ref 212P; no PSF
3	8.25	178P-202P	ref 175P; no PSF
4	10.75	234P-253P	ref 212P; no PSF
4	18.75	254P-273P	ref 212P; no PSF
4	28.75	274P-293P	ref 212P; no PSF
5	1.25	dphi358-377.mat	Matlab file
5	5.75	dphi213-232.mat	Matlab file
5	8.25	dphi178-202.mat	Matlab file
5	10.75	dphi234-253.mat	Matlab file
5	18.75	dphi254-273.mat	Matlab file
5	28.75	dphi274-293.mat	Matlab file



Table 4. Channel Turbulence Experiments - Data Files

Tape Number	Flow Location (cm)	File Name	Comments
6	1.25	582P-601P	ref 581P; PSF frame 0.03
6	2.25	731P-750P	ref 730P; PSF frame 0.03
6	3.75	603P-623P	ref 602P; PSF frame 0.03
6	5.75	624P-643P	ref 623P; PSF frame 0.03
6	8.25	645P-664P	ref 644P; PSF frame 0.03
6	10.75	666P-685P	ref 665P; PSF frame 0.03
6	13.25	687P-706P	ref 686P; PSF frame 0.03
6	15.75	708P-727P	ref 707P; PSF frame 0.03
7	1.25	dphi581-601.mat	Matlab file
7	2.25	dphi730-750.mat	Matlab file
7	3.75	dphi602-623.mat	Matlab file
7	5.75	dphi623-643.mat	Matlab file
7	8.25	dphi644-664.mat	Matlab file
7	10.75	dphi665-685.mat	Matlab file
7	13.25	dphi686-706.mat	Matlab file
7	15.75	dphi707-727.mat	Matlab file
8	1.25	psf581-601.mat	Matlab file
8	2.25	psf730-750.mat	Matlab file
8	3.75	psf602-623.mat	Matlab file
8	5.75	psf623-643.mat	Matlab file
8	8.25	psf644-664.mat	Matlab file
8	10.75	psf665-685.mat	Matlab file
8	13.25	psf686-706.mat	Matlab file
8	15.75	psf707-727.mat	Matlab file

### *Appendix B. Data files for high-speed cameras*

This Appendix provides a complete set of tables corresponding to the data collected during this research on the time-resolved, channel turbulence measurements described in Chapter V. Measurements for each flow location are in separate directories. Each directory holds the ensemble of slope or PSF/shadowgraph files as individual image files. For example, 615/615-0001.img refers to the first realization for the measurement group 615. Images are  $256 \times 256$  arrays.

The ensemble size for one beam location in the flow was 255 realizations. All data files are presently located on /elroy2/bernard/matlab/d on the Sparc20 work station in Bldg. 194, Rm. 30.

Table 5. Channel Turbulence Experiments - Slopes and Simultaneous Shadowgraphs

File Location	Flow Location (cm)	File Name	Comments	Flat/Dark/Reference
elroy2	1.25	343	Slopes	340/341/342
elroy2	2.0	346	Slopes	340/344/345
elroy2	3.75	349	Slopes	340/347/348
elroy2	5.0	352	Slopes	340/350/351
elroy2	7.5	355	Slopes	340/353/354
elroy2	10.0	358	Slopes	340/356/357
elroy2	12.5	361	Slopes	340/359/360
elroy2	15.0	364	Slopes	340/362/363
elroy2	1.25	643	Shadowgraphs	640/641/642
elroy2	2.0	646	Shadowgraphs	640/644/645
elroy2	3.75	649	Shadowgraphs	640/647/648
elroy2	5.0	652	Shadowgraphs	640/650/651
elroy2	7.5	655	Shadowgraphs	640/653/654
elroy2	10.0	658	Shadowgraphs	640/656/657
elroy2	12.5	661	Shadowgraphs	640/659/660
elroy2	15.0	664	Shadowgraphs	640/662/663

Table 6. Channel Turbulence Experiments - Slopes and Simultaneous PSF's

File Location	Flow Location (cm)	File Name	Comments	Flat/Dark/Reference
elroy2	1.25	372	Slopes	340/370/371
elroy2	2.0	375	Slopes	340/373/374
elroy2	3.75	378	Slopes	340/376/377
elroy2	5.0	381	Slopes	340/379/380
elroy2	7.5	384	Slopes	340/382/383
elroy2	10.0	387	Slopes	340/385/386
elroy2	12.5	390	Slopes	340/388/389
elroy2	15.0	393	Slopes	340/381/382
elroy2	1.25	672	PSF	640/670/671
elroy2	2.0	675	PSF	640/673/674
elroy2	3.75	678	PSF	640/676/677
elroy2	5.0	681	PSF	640/679/680
elroy2	7.5	684	PSF	640/682/683
elroy2	10.0	687	PSF	640/685/686
elroy2	12.5	690	PSF	640/688/689
elroy2	15.0	693	PSF	640/691/692

## Bibliography

1. R. D. Bowersox, J. A. Schetz, and R. W. Conners. Digital analysis of shadowgraph images for statistical index of refraction (density) turbulent fluctuation properties in high-speed flow. *Measurement*, 15:201–209, 1995.
2. G. L. Brown and A. Roshko. On density effects and large structure in turbulent mixing layers. *J. Fluid Mech.*, 64:775–816, 1974.
3. L. Chew and W. Christiansen. Coherent structure effects on the optical performance of plane shear layers. *AIAA Journal*, 29:76–80, 1990.
4. L. Chew and W. H. Christiansen. Experimental investigation of free shear layer optics. *AIAA paper*, AIAA 91-1722, 1991.
5. P. E. Dimotakis. Turbulent free shear mixing layer and combustion. In S. N. Murthy and E. T. Curran, editors, *High-Speed Flight Propulsion Systems*, volume 137 of *Progress in Astronautics and Aeronautics*, chapter 5, pages 265–340. Am Inst of Aeronautics and Astronautics, 1991.
6. D. L. Fried. Statistics of a geometric representation of wavefront distortion. *J. Opt. Soc. Am.*, 55:1427–1435, 1965.
7. D. L. Fried. Optical resolution through a randomly inhomogeneous medium for very long and ver short exposures. *J. Opt. Soc. Am.*, 56(10):1372–1379, 1966.
8. P. J. Gardner, M. C. Roggemann, B. M. Welsh, R. D. Bowersox, and T. E. Luke. Statistical anisotropy in free turbulence for mixing layers at high reynolds numbers. *Accepted for publication in Applied Optics*, Jan 1996.
9. J. D. Gaskill. *Linear systems, Fourier Transforms, and Optics*. John Wiley and Sons, New York, 1978.
10. K. G. Gilbert. Overview of aero-optics. In *Aero-optical phenomena*, volume 80, pages 1–9. Am Inst of Aeronautics and Astronautics, 1982.
11. K. G. Gilbert, L. J. Otten, and W. C. Rose. Atmospheric propagation of radiation. In F. G. Smith, editor, *Infrared and electro-optical systems handbook*, volume 2, chapter 3, pages 233–285. SPIE optical engineering press, 1993.
12. J W. Goodman. *Introduction to Fourier Optics*. McGraw-Hill, San Francisco CA, 1968.
13. J. W. Goodman. *Statistical Optics*. John Wiley and Sons, New York, 1985.
14. G. M. Grechko, A. S. Gurvich, V. Kan, S. V. Sokolovskii, and S. A. Savchenko. Scintillations and random refraction during occultations by terrestrial atmosphere. *J. Opt. Soc. of Am. A2*, pages 2120–2126, 1985.
15. G. Havener. Optical wave front variance: a study on analytical models in use today. *AIAA paper*, AIAA-92-0654, 1992.
16. E. Hecht. *Optics*. Addison Wesley, Reading, MA, 1987.

17. L. Hesselink. Optical tomography. In W. J. Yang, editor, *Handbook of Flow Visualization*, pages 307–328. Hemisphere Publishing, New York, 1989.
18. C. M. Ho and P. Huerre. Perturbed free shear layers. In *Annual Review of Fluid Mech*, volume 16, pages 365–424. Annual Reviews Inc, Palo Alto, CA, 1984.
19. R. H. Hudgin. Wave front reconstruction for compensated imaging. *J. Opt. Soc. Am.*, 67:375–377, 1977.
20. D.W. Jewell. Flow visualization of a turbulent shear flow using an optical wavefront sensor. Masters thesis, afit/geo/eng/94d-04, Air Force Inst of Tech, 1994.
21. E. J. Jumper and R. J. Hugo. Optical phase distortion due to turbulent-fluid density fields: quantification using the small-aperture beam technique. *AIAA Paper*, AIAA 92-3020, 1992.
22. S. M. Kay. *Modern Spectral Estimation*. Prentice Hall, New Jersey, 1988.
23. D. Kelsall. Optical measurements of degradation in aircraft boundary layers. In *Aero-Optical Phenomena*, volume 80, pages 261–293. Am Inst of Aeronautics and Astronautics, 1982.
24. J. Lee. Topology of trajectories of the 2d navier-stokes equations. *Chaos (Am Inst of Physics)*, 2(4):537–563, 1992.
25. R. W. Lee and J. C. Harp. Weak scattering in random media, with applications to remote probing. In *Proc. IEEE*, volume 57, pages 375–406, 1969.
26. E. P. Magee. Characterization of laboratory generated turbulence by optical phase measurements. 1993, Masters Thesis, Air Force Inst of Tech, WPAFB OH.
27. E. P. Magee and B. M. Welsh. Characterization of laboratory-generated turbulence by optical phase measurements. *Opt. Eng.*, 33(11):3810–3817, 1994.
28. V. N. Mahajan. Strehl ratio for primary aberrations in terms of their aberration variance. *J. Opt. Soc. Am.*, 73(6):860–861, June 1983.
29. L. McMackin, B. Masson, N. Clark, K. Bishop, R. Pierson, and E. Chen. Hartmann wave front sensor studies of dynamic organized structure in flowfields. *AIAA Journal*, 33(11):2158–2164, November 1995.
30. A. S. Monin and A. M. Yaglom. *Statistical Fluid Mechanics: Mechanics of Turbulence*, volume 2. MIT Press, Cambridge MA, 1975. Translated version of 1965 Russian text.
31. F. C. Moon. *Chaotic and fractal dynamics: an introduction for applied scientists and engineers*. John Wiley and Sons, Inc., 1992.
32. L. J. Otten and K. G. Gilbert. Inviscid flow fields: Experimental results. In *Aero-Optical Phenomena*, pages 233–241. Am Inst of Aeronautics and Astronautics, New York, 1982.
33. A. Papoulis. *Probability, Random Variables, and Stochastic Processes*. McGraw Hill, New York, 1991.

34. T. L. Pennington. Performance comparison of the shearing interferometer and hartmann wavefront sensors. Masters thesis, afit/ge/eng/93d-31, Air Force Inst of Tech, 1993.
35. T. L. Pennington, B. M. Welsh, and M. C. Roggemann. Performance comparison of the shearing interferometer and the hartmann wavefront sensors. *SPIE Proc. on Adaptive Optics in Astronomy*, 2201:508–518, 1994.
36. L. F. Richardson. *Weather Prediction by Numerical Process*. Cambridge Universal Press, 1922.
37. M. C. Roggemann, P. J. Gardner, B. M. Welsh, R. D. Bowersox, and D. W. Jewell. Gas flow visualization by means of sheared beam interferometry: sensitivity, maximum measurable gradient of the density fluctuation, and integrated density estimation. *Accepted for publication in Measurements*, Oct 1995.
38. M. C. Roggemann and C. L. Matson. Power spectrum and fourier phase spectrum estimation by using fully and partially compensating adaptive optics and bispectrum postprocessing. *J. Opt. Soc. Am. A*, 9(9):1525–1535, September 1992.
39. M. C. Roggemann, B. M. Welsh, P. J. Gardner, R. L. Johnson, and B. L. Pedersen. Sensing three-dimensional index-of-refraction variations by means of optical wavefront sensor measurements and tomographic reconstruction. *Optical Eng*, 34(5):1374–1384, May 1995.
40. W. C. Rose and D. A. Johnson. Unsteady density and velocity measurements in the 6x6 ft wind tunnel. In K. Gilbert and L. Otten, editors, *Aero-Optical Phenomena*, volume 80, pages 218–232. Am Inst of Aeronautics and Astronautics, 1982.
41. D. G. Sandler, L. Cuellar, M. Lefebvre, T. Barrett, R. Arnold, P. Johnson, A. Rego, G. Smith, G. Taylor, and B. Spivey. Shearing interferometry for laser-guide-star atmospheric correction at large  $d/r_o$ . *J. Opt. Soc. Am. -A*, 11:858–873, 1994.
42. D. L. Snyder. Image recovery from data acquired with a charge-coupled-device camera. *J. Opt. Soc. Am.*, 10(5):1014–1023, May 1993.
43. W. H. Southwell. Wave-front estimation from wave-front slope measurements. *J. Opt. Soc. Am.*, 70(8):998–1006, August 1980.
44. W. J. Steinmetz. Second moments of optical degradation due to a thin turbulent layer. In K. Gilbert and L. Otten, editors, *Aero-Optical Phenomena*, volume 80, pages 78–100. Am Inst of Aeronautics and Astronautics, 1982.
45. V. L. Streeter. *Handbook of Fluid Dynamics*. McGraw-Hill, Inc., NY, 1st edition, 1961.
46. G. W. Sutton. Optical imaging through aircraft turbulent boundary layers. In *Aero-Optical Phenomena*, pages 15–39. Am Inst of Aeronautics and Astronautics, 1982.
47. G. W. Sutton. Optical imaging through aircraft turbulent boundary layers. In K. Gilbert and L. Otten, editors, *Aero-Optical Phenomena*, volume 80, pages 15–39. Am Inst of Aeronautics and Astronautics, 1982.

48. G. W. Sutton. Aero-optical foundations and applications. *AIAA Journal*, 23:1525–1537, 1985.
49. C. R. Truman. The influence of turbulent structure on optical phase distortion through turbulent shear flows. AIAA paper, AIAA 92-2817, 1992.
50. R. K. Tyson. *Principles of adaptive optics*. Academic Press, Inc., San Diego CA, 1991. pp. 5-15.
51. A. Verhoff. Prediction of optical propagation losses through turbulent boundary/shear layers. In *Aero-optical Phenomena*, volume 80, pages 40–77. American Inst of Aeronautics and Astronautics, 1982.
52. B. T. Vu and G. W. Sutton. Laser beam degradation through optically turbulent mixing layers. *AIAA paper*, AIAA-80-1414, 1980.
53. E. P. Wallner. Optimal wavefront correction using slope measurements. *J. Opt. Soc. Am.*, 73:1771–1776, 1983.
54. F. M. White. *Viscous Fluid Flow*. McGraw-Hill, Inc., NY, 2nd edition, 1991.
55. J. B. Wissler. Transmission of thin light beams through turbulent mixing layers. 1992, Ph.D. Thesis, Calif Inst of Tech.

*Vita*

Captain Patrick J. Gardner ~~was born on 22 August 1947 at [redacted]~~. He graduated from Pasco High School, Dade City Florida in 1971. Following a period of enlisted service in the U. S. Air Force as a medical laboratory technician, he attended the University of Florida and was awarded the Bachelor of Science degree in Electrical Engineering in August 1984. In November 1984 he was commissioned in the U. S. Air Force and was assigned to the F-15 program office at Wright-Patterson AFB OH as a flight controls engineer. In December 1988 he was awarded the Master of Science degree in Electrical Engineering from the Air Force Institute of Technology with a specialty in electro optics. He was then assigned to the Air Force Armament Laboratory, Eglin AFB FL, where he managed the development of a joint Air Force-Navy laser radar system for autonomous air-to-surface weapon guidance. In July 1993 he returned to the Air Force Institute of Technology to pursue the Ph.D, where his research centered on developing statistical models of turbulent mixing layers using optical measurements. He is a member of SPIE, Tau Beta Pi, and Eta Kappa Nu. Pat is married to Katerina ~~([redacted])~~ Gardner. They have five children.



REPORT DOCUMENTATION PAGE			Form Approved OMB No. 0704-0188	
Public reporting burden for this collection of information is estimated to average 1 hour per response, including the time for reviewing instructions, searching existing data sources, gathering and maintaining the data needed, and completing and reviewing the collection of information. Send comments regarding this burden estimate or any other aspect of this collection of information, including suggestions for reducing this burden, to Washington Headquarters Services, Directorate for Information Operations and Reports, 1215 Jefferson Davis Highway, Suite 1204, Arlington, VA 22202-4302, and to the Office of Management and Budget, Paperwork Reduction Project (0704-0188), Washington, DC 20503.				
1. AGENCY USE ONLY (Leave blank)		2. REPORT DATE 17 May 1996		3. REPORT TYPE AND DATES COVERED Ph.D. Dissertation
4. TITLE AND SUBTITLE Characterization of Spatial and Temporal Anisotropy in Turbulent Mixing Layers Using Optical Techniques			5. FUNDING NUMBERS	
6. AUTHOR(S) Patrick J. Gardner, Captain, USAF				
7. PERFORMING ORGANIZATION NAME(S) AND ADDRESS(ES) Air Force Institute of Technology School of Engineering 2950 P St. WPAFB, OH 45433-7765			8. PERFORMING ORGANIZATION REPORT NUMBER AFIT/DS/ENP/96-04	
9. SPONSORING / MONITORING AGENCY NAME(S) AND ADDRESS(ES) AFOSR/NE (Major Bill Arrasmith) Bolling AFB, WA DC			10. SPONSORING / MONITORING AGENCY REPORT NUMBER	
11. SUPPLEMENTARY NOTES				
12a. DISTRIBUTION / AVAILABILITY STATEMENT Approved for Public Release; Distribution Unlimited.			12b. DISTRIBUTION CODE	
13. ABSTRACT (Maximum 200 words) The optical aberrations induced by mixing layers of dissimilar gases are recorded and analyzed. Laser light was propagated through a mixing layer of Helium and Nitrogen gas, having velocities of 8.5 m/sec and 1.5 m/sec, respectively. The light was propagated in a direction perpendicular to the plane of the mixing layer. The mixing layer was evaluated in two experimental regimes: free turbulent mixing, where the mixing layer spreads into the surrounding air; and channel flow, where the mixing layer is confined to a rectangular channel. The optical perturbations induced by the mixing layer were recorded using a lateral shearing interferometer and a point spread function camera. Autocorrelation functions and structure functions were computed from the spatially resolved phase surfaces obtained using the shearing interferometer. For both the free and channel flows, the phase fluctuations were not wide-sense stationary. Consequently, the Strehl ratio predicted by traditional aero-optical models did not agree with experimental measurements except in regions of the flow where the Reynolds number was low. However, the phase fluctuations were locally homogeneous. A two-dimensional power law model was developed, analogous to the one-dimensional Kolmogorov model for isotropic turbulence. This model predicted a relative Strehl ratio which closely matched experiment throughout the flow. In a second series of experiments, the gas velocities were reduced to 4.5 m/s and 1.0 m/s for the Helium and Nitrogen gas, respectively. The flow orientation was rotated such that the laser light propagated in a direction parallel to the plane of the mixing layer. Simultaneous high-speed measurements of shadowgraphs and wavefront slopes were used to assess the applicability of Taylor's frozen flow hypothesis to the mixing layer. Results indicated that frozen flow is at best limited to time scales on the order of 1 ms. For this flow orientation the phase fluctuations were nonhomogeneous.				
14. SUBJECT TERMS aero-optics, free shear layers, Hartmann Wavefront Sensor, Kolmogorov model, turbulence, mixing layer, shearing interferometer, Strehl ratio, structure function, wave front sensor			15. NUMBER OF PAGES 148	
			16. PRICE CODE	
17. SECURITY CLASSIFICATION OF REPORT Unclassified	18. SECURITY CLASSIFICATION OF THIS PAGE Unclassified	19. SECURITY CLASSIFICATION OF ABSTRACT Unclassified	20. LIMITATION OF ABSTRACT Unlimited	